



**Aggregation, Attachment, and Transport of Nanoscale Titanium Dioxide
(nTiO₂) in Subsurface Environments:
Effects of Complex Water Chemistry and Medium**

By © Zahra Sadat Rastghalam

A Thesis submitted to the School of Graduate Studies in partial fulfillment of the requirements
for the degree of

Doctor of philosophy

Memorial University of Newfoundland

Department of Earth Sciences

Oct 2019

St. John's, Newfoundland and Labrador

Abstract

The transport of contaminants in subsurface environments is influenced by water chemistry and properties of the transport media. Due to the development and application of nanotechnology, engineered nanoparticles, such as nanoscale titanium dioxide ($n\text{TiO}_2$), are being released into the aquatic environment, which may pose serious hazards to the ecosystem. Extensive research has been performed to understand engineered nanoparticle's fate and transport in groundwater. Many of the studies focus on the influence of simple water chemistry (e.g., pH, ionic strength, dissolved ions) and well-defined porous media (e.g., quartz sand or glass beads). The results obtained from some other studies emphasize the need to consider the effect of heterogeneous media, along with complex water chemistry, when evaluating engineered nanoparticle contamination risks. The objective of this thesis is to elucidate the effect of complex water chemistry and geochemically heterogeneous media on $n\text{TiO}_2$ transport and deposition, and the related mechanisms (e.g., ripening, precipitation, deposition, aggregation, blocking, straining) were explained. Batch experiments illustrated that $n\text{TiO}_2$ aggregation and attachment were strongly influenced by pH and Ca^{2+} , both of which modified $n\text{TiO}_2$ surface charges. The effect of phosphate on $n\text{TiO}_2$ and illite attachment to sand was influenced by pH and cation valency. Moreover, illite attachment to sand was much lower than that of $n\text{TiO}_2$ under all the conditions tested in this study. Results from column experiments showed that under complex physicochemical conditions, $n\text{TiO}_2$ transport is not only controlled by the interactions between $n\text{TiO}_2$ and common groundwater/aquifer components (e.g., suspended illite clay, phosphate, Fe oxyhydroxide coating) but also the interactions between these components. Finally, column experiments illustrated the importance of soil and sediment mineralogical and organic components, including Fe oxyhydroxides, clay (e.g., illite), and solid organic matter (e.g., peat moss) on $n\text{TiO}_2$ transport. Results from this thesis

research contributed to the knowledge of the individual and synergistic effects of complex water chemistry and geochemically heterogeneous media on the fate and transport of engineered nanoparticles in natural environments.

Acknowledgements

Firstly, I would like to thank my supervisor Dr. Tao Cheng for the opportunity to join his research group and for all his support and guidance throughout my studies. I have learned so much from you.

Also, I'd like to thank the committee members Dr. Helen Zhang and Dr. Bing Chen for taking the time to read my thesis and their heart warming supports.

I would like to give sincere thanks to:

Dr. Valerie Booth for allowing the use of Zeta sizer, Inês Nobre Silva and John Allen for ICP-MS, Jamie Warren for DOC, Alison Pye for organic carbon, and Wanda Alyward for XRD analysis.

All the staff of the Earth Sciences Department, including Robbie Hicks, Michelle Miskell, Keir Hiscock, Diane Guzzwell, Danyelle Drodge, and Jane O'Neill.

My fellow lab colleagues Bradley Freake for his assistance running the experiments in Chapter 1, Robert Bazeley for collecting the sediment used in Chapter 3, as well as Yang Wu, Leanne Fisher-Power, Zhong Tang, Yuhong Zhou, A.K.M. Fayazul Kabir, for the assistance and company in the lab.

My gratitude to Memorial University of Newfoundland for providing personal financial support through the School of Graduate Studies Fellowship. I gratefully acknowledge funding from the Natural Sciences and Engineering Research Council for Canada's Discovery Grant (No. 402815-2012) and Canada Foundation for Innovation's Leaders Opportunity Fund (No. 31836).

Last but not least, I extend my most sincere thanks to my lovely family and best friends for being there for me when I needed it most; their care and love will be forever appreciated.

Table of Contents

Abstract.....	ii
Acknowledgements.....	iv
Table of Contents.....	v
List of Tables.....	ix
Supplementary Tables.....	ix
List of Figures.....	x
Supplementary Figures.....	xi
List of Abbreviations and Symbols.....	xiii
Chapter 1. Introduction and overview.....	1
1.1. Environmental context.....	1
1.2. Factors and mechanisms affecting nTiO ₂ transport.....	2
1.2.1. Effect of water chemistry.....	2
1.2.2. Effect of porous media.....	5
1.2.3. Contributing mechanisms.....	7
1.2.3.1. Stability and aggregation.....	7
1.2.3.2. Attachment.....	7
1.2.3.3. Blocking.....	8
1.2.3.4. Straining.....	9
1.3. Theoretical considerations.....	9
1.3.1. Zeta potential and hydrodynamic diameter (HDD).....	9
1.3.2. DLVO calculations.....	10
1.3.3. Modeling nTiO ₂ transport.....	11

1.3.4. Adsorption isotherms.....	11
1.4. Thesis objectives	12
1.5. Co-authorship statement.....	14
Chapter 2. Fine particle attachment to quartz sand in the presence of multiple interacting dissolved components	15
Abstract	15
2.1. Introduction	16
2.2. Materials and methods	19
2.2.1. Preparation of nTiO ₂ and illite colloid suspensions, stock solutions, and quartz sand	19
2.2.2. Batch experiments	21
2.2.2.1. nTiO ₂ and illite colloid attachment to quartz sand.....	21
2.2.2.2. Phosphate adsorption to nTiO ₂ , illite colloid, and quartz sand.....	22
2.2.3. Zeta potential and hydrodynamic diameter (HDD) measurement.....	23
2.2.4. DLVO interaction energy calculation.....	24
2.3. Results and discussion.....	26
2.3.1. nTiO ₂ and illite colloid aggregation	26
2.3.2. Effect of cation valency on nTiO ₂ and illite colloid attachment to quartz sand.....	30
2.3.3. Phosphate adsorption to nTiO ₂ , illite colloid, and quartz sand	34
2.3.4. Effect of phosphate on nTiO ₂ and illite colloid attachment to quartz sand.....	39
2.4. Conclusions	42
Acknowledgments.....	44
Appendix 1. Supplementary data.....	44

Chapter 3. Nanoscale titanium dioxide (nTiO ₂) aggregation and transport in the co-presence of dissolved phosphate, illite colloid, and Fe-oxyhydroxide coating.....	45
Abstract	45
3.1. Introduction.....	46
3.2. Materials and methods	50
3.2.1. Stock solutions and suspensions	50
3.2.2. Transport media.....	51
3.2.3. Zeta potential and HDD measurement	52
3.2.4. Column experiments	54
3.2.5. Theoretical considerations.....	55
3.2.5.1. DLVO calculations	55
3.2.5.2. Modeling nTiO ₂ transport.....	55
3.3. Results and discussions.....	56
3.3.1. Zeta potential and HDD of the influent suspensions.....	56
3.3.2. nTiO ₂ transport.....	61
3.3.2.1. nTiO ₂ suspension at pH 5 (blue diamonds (◇) in Fig. 7-a & 7-b)	61
3.3.2.2. nTiO ₂ -illite suspension at pH 5 (blue diamonds (◇) in Fig. 7-c & 7-d).....	65
3.3.2.3. nTiO ₂ -phosphate suspension at pH 5 (green squares (□) in Fig. 7-a & 7-b).....	67
3.3.2.4. nTiO ₂ -phosphate-illite suspension at pH 5 (green squares (□) in Fig. 7-c & 7-d) ..	68
3.3.2.5. nTiO ₂ suspension at pH 9 (red times (×) in Fig. 7-a & 7-b).....	68
3.3.2.6. nTiO ₂ -illite suspension at pH 9 (red times (×) in Fig. 7-c & 7-d)	70
3.3.2.7. nTiO ₂ -phosphate suspension at pH 9 (brown triangle (Δ) in Fig. 7-a & 7-b)	71
3.3.2.8. nTiO ₂ -phosphate-illite suspension at pH 9 (brown triangle (Δ) in Fig. 7-c & 7-d)	72

3.3.3. Modeling nTiO ₂ transport	72
3.3.3.1. nTiO ₂ and nTiO ₂ -illite suspension at pH 5 (blue diamonds (◇) in Fig. 7).....	73
3.3.3.2. nTiO ₂ and nTiO ₂ -illite suspension at pH 9 (red times (×) in Fig. 7).....	74
3.3.3.3. nTiO ₂ -phosphate and nTiO ₂ -illite-phosphate suspensions at pH 9 (brown triangles (Δ) in Fig. 7)	75
3.4. Conclusions.....	75
Acknowledgments.....	76
Appendix 2. Supplementary data	77
Chapter 4. The role of Fe oxyhydroxide coating, illite clay, and peat moss in nanoscale titanium dioxide (nTiO ₂) retention and transport in geochemically heterogeneous media.....	78
4.1. Introduction.....	79
4.2. Materials and methods	83
4.2.1. Materials.....	83
4.2.2. Methods.....	86
4.2.2.1. Preparation of the nTiO ₂ suspension and background solution.....	86
4.2.2.2. Zeta potential (ZP) and hydrodynamic diameter (HDD) measurement	86
4.2.2.3. Column experiments.....	87
4.2.3. DLVO calculations.....	89
4.3. Results and discussions.....	89
4.3.1. Properties of the sediment, Fe oxyhydroxide coated sand, and illite.....	89
4.3.2. nTiO ₂ transport.....	90
4.3.2.1. nTiO ₂ transport and retention mechanisms at pH = 5	93
4.3.2.2. nTiO ₂ transport and retention mechanisms at pH = 9	98

4.4. Conclusions.....	102
Acknowledgments.....	103
Appendix 3. Supplementary data.....	103
Chapter 5. Summary	104
Appendices.....	107
Appendix 1. Supporting Information for Chapter 2.....	107
Appendix 2. Supporting Information for Chapter 3.....	112
Appendix 3. Supporting Information for Chapter 4.....	121
Appendix 4. All the original data for Chapter 2, 3, and 4 in electronic format	132
References.....	133

List of Tables

Table 1 . DLVO calculation results for particle-particle interactions.....	58
Table 2. DLVO calculation results for particle-collector interactions.....	63
Table 3. The fitted parameters for the nTiO ₂ breakthrough curves.	73

Supplementary Tables

Table S1. Hamaker constant applied in DLVO calculations.	114
Table S2. Physical and chemical conditions of column transport experiments using 100 mg/L nTiO ₂	117
Table 3. Physical properties of the column transport experiment. The Fe oxyhydroxide, illite, and peat moss mass reported is the dry mass in each column.	122

List of Figures

Fig. 1. Hydrodynamic diameter (HDD) (z-average) of nTiO₂ and illite in 1 mM NaCl (blue columns) and 0.5 mM CaCl₂ (orange columns) solutions at pH 5 and 9..... 27

Fig. 2. Zeta potential of nTiO₂, illite, and quartz sand in 1 mM NaCl (blue columns) and 0.5 mM CaCl₂ (orange columns) solutions at pH 5 and 9. 28

Fig. 3. Attachment of nTiO₂ and illite to 2 g quartz sand in the absence of the phosphate..... 31

Fig. 4. Adsorption of the phosphate to nTiO₂ and illite colloid in 1 mM NaCl (a) and 0.5 mM CaCl₂ solutions (b) at pH 5 and 9. 35

Fig. 5. Attachment of 100 mg/L nTiO₂ (a, b) and 100 mg/L illite (c, d) to 2 g quartz sand in 1 mM NaCl (a, c) and 0.5 mM CaCl₂ solutions (b, d) at pH 5 and 9. 40

Fig. 6. Zeta potential (a & b) and HDD (c and d) of various suspensions..... 57

Fig. 7. Measured (symbols) and fitted (lines) BTCs of nTiO₂ for experiments conducted in quartz sand (a & c) and Fe oxyhydroxide-coated sand (b & d) columns. 62

Supplementary Figures

Fig. S1. Interaction energy vs. separation distance between nTiO ₂ particles in 1 mM NaCl solution (a, c) and 0.5 mM CaCl ₂ solution (b, d) at pH 5 (a, b) and pH 9 (c, d).	107
Fig. S2. Interaction energy vs. separation distance between illite particles in 1 mM NaCl solution (a, c) and 0.5 mM CaCl ₂ solution (b, d) at pH 5 (a, b) and pH 9 (c, d).	108
Fig. S3. Zeta potential of nTiO ₂ as a function of pH in phosphate-free 1 mM NaCl solution. ..	109
Fig. S4. Interaction energy vs. separation distance between nTiO ₂ and quartz sand in 1 mM NaCl solution (a, c) and 0.5 mM CaCl ₂ solution (b, d) at pH 5 (a, b) and pH 9 (c, d).....	110
Fig. S5. Interaction energy vs. separation distance between illite colloid and quartz sand in 1 mM NaCl solution (a, c) and 0.5 mM CaCl ₂ solution (b, d) at pH 5 (a, b) and pH 9 (c, d).	111
Fig. S6. SEM image (a) and energy dispersive X-ray (EDX) spectrum of element distribution (b) of representative Fe oxyhydroxide-coated sand surface.	118
Fig. S7. Effluent pH for quartz sand column (a and b) and Fe-oxyhydroxide coated sand column (c and d).	119
Fig. S8. Stability (a) and zeta potential (b) of nTiO ₂ suspension over time before (blue diamonds) and after (green squares) adding 10 mg/L phosphate at pH 5 and 1 mM NaCl background.....	120
Fig. S9. X-ray diffraction (XRD) spectra of the sediment.....	123
Fig. S10. Grain size distribution of sediment (blue squares) and quartz sand (gray circles).....	124
Fig. S11. Grain size distribution of illite (green circles) and quartz sand (gray circles).	125
Fig. S12. Average of duplicate nTiO ₂ breakthrough curve experiments with standard deviation as error bars.	126
Fig. S13. Effluent pH and electrical conductivity (EC) vs. pore volume for columns with various medium.	127

Fig. S14. Effluent DOC measurement for columns with various medium. 128

Fig. S15. Electrostatic interactions between nTiO₂ and various collectors using pH 5 (a & c) and pH 9 (b & d) influent suspensions. 129

Fig. S16. Particle-collector interaction energy vs. separation distance between nTiO₂ particles and (a) quartz sand, (b) Fe coating, (c) illite, and (d) peat moss in 1 mM NaCl solution at pH 5. ... 130

Fig. S17. Particle-collector interaction energy vs. separation distance between nTiO₂ particles and (a) quartz sand, (b) Fe coating, (c) illite, and (d) peat moss in 1 mM NaCl solution at pH 9. ... 131

List of Abbreviations and Symbols

Al - aluminum

Al₂O₃ - aluminum oxide

AOD - ammonium oxalate under darkness

BaCl₂ - barium chloride

BTC - breakthrough curve

°C - Degree Celsius

Ca - calcium

C/C₀ - ratio of recovered concentration to concentration in the influent

cm - centimeter

C60 - Fullerenes

DCB - dithionite citrate bicarbonate

DLS - Dynamic light scattering

DLVO theory - theory by Derjaguin, Landau, Verwey, and Overbeek explaining stability of colloids

DOC - dissolved organic carbon

DOM - dissolved organic matter

EDL - electrical double layer

EDX- energy dispersive X-ray

ENP - engineered nanoparticle

Fe - iron

g - gram

g/mL - milligrams per milliliter

HDD - hydrodynamic diameter

ICP-MS - inductively coupled plasma mass spectrometry

IS - ionic strength

J - joule

$k_B T$ - energy unit equals 4.11×10^{-21} J

kg - kilogram

L - liter

LW - London–van der Waals

$\mu\text{g/L}$ - microgram per liter

μm - micrometer

M - mole

mg - milligram

mL - milliliter

mL/min - milliliters per minute

mg/kg - milligrams per kilogram

mg/L - milligrams per liter

mm- millimeter

mL/min – milliliter per minute

mM - millimole

mol/L - moles per liter

mV - millivolts

nm - nanometer

nTiO₂ - nanoscale titanium dioxide

NaCl - sodium chloride

NaOH - sodium hydroxide

NOM - natural organic matter

pH - power of hydrogen; a measure of hydrogen ion activity

PZC - point of zero charge

PV - pore volume

rpm - revolutions per minute

SEM - scanning electron microscope

SI - supporting information

SOC - soil organic carbon

SOM - soil organic matter

VDW - van der Waals

XRD - X-ray diffraction

ZP - zeta potential

Chapter 1. Introduction and overview

1.1. Environmental context

Ultrafine particles with lengths between 1 nm and 100 nm in at least two dimensions are defined as nanoparticles and are omnipresent in environmental and aquatic systems (Delay and Frimmel, 2012). Nanoparticles exhibit unique physicochemical properties that are different from either molecules or macroscopic materials (Schramm, 2006). Nanotechnology represents an expanding economic sector due to the novel properties of nanoparticles, which can decrease costs and increase productivity and functionality (Solovitch et al., 2010). Although various types of nanoparticles (e.g. natural, artificial, organic, inorganic) exist, this study focuses on the occurrence of engineered inorganic nanomaterials as a part of the nanoparticles present in the environment. Engineered nanoparticles are among the most promising manufactured materials that are commercially used across several industrial processes (Klaine et al., 2012; Lin et al., 2010). Among the engineered nanoparticles, nanoscale titanium dioxide (nTiO_2) is one of the most popular (Sharma, 2009; Wiesner et al., 2006). The increasingly common practice of using nTiO_2 in various commercial products (cosmetics, food, medicine, textiles, paints, etc.) (Chen and Mao, 2007) has led to increasing concerns about the fate of this potentially hazardous nanomaterial and its adverse effects on ecosystems. nTiO_2 may accidentally find its way to natural environments during the production, processing, and transport stage, and it can detach from used and disposed products (Mackevica and Foss Hansen, 2016; Windler et al., 2012). It has been demonstrated that interaction between nTiO_2 and heavy metals (e.g. Pb (II), Cu (II), and Zn (II)) can enhance the heavy metals' mobility in the environment and increase their toxicity (Hu and Shipley, 2012). Moreover, nTiO_2 is a photoactive material, and it has been confirmed that UV-illumination enhanced nTiO_2 toxicity on bacterial suspensions (Prasad et al., 2009). Moreover, it has been

reported that nTiO₂ is toxic to living creatures (Bang et al., 2011; Rehn et al., 2003), affirming the need for extensive research on the fate and transport of nTiO₂ in the ecosystem. The risks and hazards that nanoparticles may pose to the ecosystem are directly associated with their mobility in aquatic systems. Therefore, the factors and mechanisms affecting nanoparticle mobility and retention in complex natural water systems need to be considered.

1.2. Factors and mechanisms affecting nTiO₂ transport

1.2.1. Effect of water chemistry

Nanoparticle movement is a function of the properties of the particles and groundwater chemistry. The water pH, ionic strength, dissolved components of groundwater including the anions (e.g., phosphate, chloride), cations (e.g. Na⁺, Ca²⁺, and Mg²⁺), dissolved organic matter (DOM), and suspended clay particles are found to influence the stability and transport of nTiO₂. In the aquatic environment, difference in pH and ionic strength (IS) may alter the surface properties of nanoparticles and their transport behavior. A substantial number of studies on the aggregation and dispersion of nanoparticles indicate that particles tend to aggregate at a pH near their point of zero charge (French et al., 2009; Ren et al., 2017; Wang, 2017). High IS facilitates aggregate formation since the double layers are compressed at a high ionic strength and the repulsive electrostatic forces between particles are reduced (French et al., 2009). Fang et al. (2013) found that both IS and pH have considerable influence on nTiO₂ transport, with lower IS (e.g., 1.0 and 10 mM) and higher pH (e.g., 7.1 and 9.6) causing unfavorable conditions for nTiO₂ deposition and thus higher mobility in sand columns.

Divalent cations (e.g., calcium and magnesium) are normally found in natural groundwater and surface waters that favor aggregate formation and the attachment of nanoparticles (Wiesner et al., 2006). It has been demonstrated that electrolyte valence influences nanoparticle stability, with

divalent electrolytes enhancing aggregate formation more effectively than monovalent electrolytes (Akaighe et al., 2012; Chen et al., 2011; French et al., 2009). In fact, divalent cations are more efficient than monovalent cations in “screening” the surface charge of nanoparticles (Baalousha et al., 2013). It has been demonstrated that Ca^{2+} affects nanoparticle aggregation more strongly than Mg^{2+} because Ca^{2+} can bridge nanoparticles, whereas Mg^{2+} destabilizes nanoparticles through electrostatic forces (Chen et al., 2006). Bridging and electrostatic forces are commonly used to explain the behavior of nTiO_2 in the presence of divalent ions (Philippe and Schaumann, 2014). McCarthy and McKay (2004) found that particle deposition rates in solutions with Ca^{2+} were higher those in solutions with Na^+ , which can be described as the effects of screening repulsive surface interaction energies between particles and solid surfaces in the aquatic environment (McCarthy and McKay, 2004). Moreover, in the presence of the Ca^{2+} electrolyte, nTiO_2 is retained more in comparison with the Na^+ electrolyte, although the Na^+ concentration is higher than the Ca^{2+} concentration (Chen et al., 2011).

Furthermore, studies indicate that anions (e.g. phosphate) may affect the stability of nTiO_2 particles. Chen et al. (2015) stated that although nTiO_2 tended to aggregate in the presence of a low phosphate concentration at pH 6.5, the aggregated nanoparticles dispersed with an increase in phosphate concentration. Similarly, the stability of nTiO_2 enhanced with an increasing phosphate concentration at pH 7.5 due to the more negative charges on nTiO_2 . nTiO_2 has been reported to adsorb phosphate anions at $\text{pH} < \text{pH}_{\text{pzc}}$ (point of zero charge) of nTiO_2 , resulting in a change in nTiO_2 surface charge and, in turn, its attachment and transport (Chen et al., 2015). Kang et al. (2011) showed that phosphate sorption onto nTiO_2 decreases with increasing pH. They explained that pH can simultaneously influence the aqueous species of phosphate and surface reactivity of nTiO_2 (Kang et al., 2011).

Natural organic matter (NOM) increased nTiO₂ stability through electrostatic repulsion and steric forces caused by NOM adsorption to nTiO₂ (Chen et al., 2012; Wu and Cheng, 2016). Numerous studies indicate that increasing DOC concentration in aqueous systems is important to enhancing the mobility and potential risk of nanoparticles in aqueous systems (Cornelis et al., 2012; Jung et al., 2014; Li et al., 2013; Loosli et al., 2015; Walshe et al., 2010; Wang, 2017; Zhang et al., 2009). For example, Wu and Cheng (2016) reported that at pH 5, low humic acid concentrations partially neutralized the positive charges on nTiO₂ and Fe oxyhydroxide-coated sand, decreasing the repulsive electrostatic forces between the surfaces and eventually increasing nTiO₂ aggregation and attachment. Conversely, high humic acid concentrations reversed the surface charges of nTiO₂ and Fe oxyhydroxide-coated sand, resulting in stable nTiO₂ suspension and low nTiO₂ attachment. At pH 9, humic acid did not affect the stability and attachment of nTiO₂ since the nTiO₂ and Fe oxyhydroxide coating were negatively charged and humic acid adsorption was low.

In aquatic systems, clay particles, including kaolinite, montmorillonite, and illite are considered the most common mineral colloids (Wilson et al., 2014), and the stability and transport of nanoparticles are influenced by these colloids (Cai et al., 2014). Zhou et al. (2012) demonstrated that clay particles could destabilize and thus immobilize nanoparticles regardless of their surface charge. Tang and Cheng (2018) further explained that nTiO₂ in the co-presence of clay colloids can form hetero-aggregates (i.e., nTiO₂-clay aggregates) at a low pH when nTiO₂ and clay colloids are oppositely charged. The generated hetero-aggregates may either attach to the quartz sand grain or remain suspended, depending on their interactions with quartz sand.

1.2.2. Effect of porous media

In addition to water chemistry, nanoparticle transport is influenced by the environmental media the nanoparticles travel through. Natural media (e.g., soil and sediment) are mainly composed of a large variety of minerals, including quartz sands, Al/Fe oxyhydroxides, clay minerals, and organic matters (Bradl, 2004; Fisher-Power and Cheng, 2018). Each component can affect nanoparticle transport directly (e.g., providing the deposition sites) or indirectly through changing the water chemistry (Fisher-Power and Cheng, 2018; Zhou and Cheng, 2018). While extensive studies have been conducted to understand the influences of water chemistry on nanoparticle transport, less attention has been paid to the effect of the transport medium.

Natural media exhibit surface charge heterogeneity, and patches of iron (Fe) and aluminum (Al) oxyhydroxides are known as common sources of this heterogeneity. Tian et al. (2012) reported that metal oxyhydroxides' impurities on the medium surface, even at a trace level, significantly influence the transport of nanoparticles. Fe/Al oxyhydroxides have relatively high points of zero charge (pH_{pzc}). Therefore, the pH of groundwater and soil water is often below the pH_{pzc} of iron (~8.4) and aluminum oxyhydroxides (~9), causing these minerals to acquire a net positive surface charge (Ryan et al., 1999; Ryan and Gschwend, 1992). Hence, it is expected that Fe/Al oxyhydroxides decrease negatively-charged nanoparticles' mobility and enhance the transport of nanoparticles when they carry positive charges. It has been shown that nanoparticle mobility was considerably inhibited with Fe oxyhydroxide-coating due to the electrostatic attraction between negatively-charged nanoparticles and positively-charged iron oxyhydroxides (Han et al., 2014; Wang et al., 2013). Nevertheless, the effect of Fe/Al oxyhydroxides on the transport of positively-charged nanoparticles is poorly understood.

Clay particles are ubiquitous in subsurface environments and can be immobile in porous media (Bayat et al., 2015) or highly mobile (Cai et al., 2014) under certain geochemical conditions. Jung et al. (2014) reported that kaolinite packed in quartz sand columns increased the transport of nanoscale zero valent iron (nZVI) through increased electrostatic and steric repulsion. However, Bayat et al. (2015) found that clay minerals including illite, kaolinite, and montmorillonite in limestone porous media decreased the transport of Al_2O_3 and nTiO_2 nanoparticles due to the morphology of the clays and straining of the nanoparticles by the clays trapped at the pore throats (Bayat et al., 2015). Contradictory results on the effect of clay particles on nanoparticle transport are probably due to various nanoparticles' properties, different types of clay, the position of clay (e.g., suspended or in porous medium), and the physicochemical conditions of experiments and, therefore, require further investigation.

In the natural environment, natural organic matter (NOM) can exist as dissolved organic matter (DOM). As mentioned in Section 1.2., DOM in general mobilizes and facilitates nanoparticle transport. However, when NOM presents as solid organic matter (SOM) in the immobile phase of an aquifer, NOM is expected to attract nanoparticles, serve as a sink, and reduce their transport. Zhou and Cheng (2018) stated that peat moss in a quartz sand column attracted fine particles and decreased particle mobility when the energy barrier between the particle and peat moss was low or non-existent. Fisher-Power and Cheng (2018) indicated low nTiO_2 transport through sediment at pH 5, which was attributable to positively-charged nTiO_2 attracting to negatively-charged minerals and SOM.

1.2.3. Contributing mechanisms

1.2.3.1. Stability and aggregation

Recent studies indicate that a complex combination of various mechanisms can dominate the transport of fine particles through porous media. Typically, nanoparticles do not remain nano-sized when released into an aquatic environment. Therefore, the stability and aggregation of nanoparticles can influence their fate, toxicity, and transformation in aqueous media (Petosa et al., 2010). Nanoparticles, due to their surface charge characteristics and small size, tend to be suspended; however, they may aggregate or disperse due to changes in ambient conditions (Delay and Frimmel, 2012). The main factors influencing the stability of nanoparticle suspensions include nanoparticle properties such as zeta potential, concentration, size, and solution chemistry, such as pH and ionic strength (Chowdhury et al., 2011). Generally, aggregated nanoparticles are less mobile and can possibly be eliminated or trapped through sedimentation and straining (Farré et al., 2009; Sharma, 2009). pH was found to considerably affect the aggregation of nanoparticles; i.e., as the pH approaches the pH_{pzc} , the repulsive forces between nanoparticles of similar surface potentials decrease, making it easier for particles to aggregate (Guzman et al., 2006; Kosmulski, 2002; Tang and Cheng, 2018).

1.2.3.2. Attachment

Nanoparticle attachment to a collector surface is a crucial mechanism in nanoparticle retention and depends on a number of factors, such as particle and collector size, zeta potential, solution chemistry (e.g., pH, ionic strength, presence of anions/cations) of the suspending medium, the existence of chemical dispersing agents, aluminium (Al) or iron (Fe) oxides/hydroxides, dissolved organic matter and the Hamaker constant of the particle-collector (Elimelech et al., 1995). The transport patterns of the nanoparticles are directly influenced by the nanoparticles'

attachment to and detachment from the medium. The physical properties of the collector, such as surface roughness, determine the effects of the medium on nanoparticle attachment (Wu and Cheng, 2016; Zhou and Cheng, 2018). Cai et al. (2014) observed that the attachment of nTiO₂ in quartz sand was strongly pH dependent. At pH 5, nTiO₂ is positively charged but quartz sand is negatively charged. As a result, the attractive electrostatic force between nTiO₂ and quartz sand results in nTiO₂ attachment to quartz sand (Cai et al., 2014; Tang and Cheng, 2018). At pH 9, both nTiO₂ and quartz sand are negatively charged; therefore, nTiO₂ shows low retention in quartz sand columns (Chen et al., 2012).

1.2.3.3. Blocking

At high concentrations of nanoparticles, blocking occurs rapidly when the particle and collector surface are oppositely charged (Chowdhury et al., 2011). According to blocking effects, while favorable attachment sites on the solid surface become fully occupied, less attachment occurs. However, the attached particles can act the same as a solid surface for subsequent colloid attachment. As a result, the attachment may increase (ripening) (Bradford and Bettahar, 2006). Chowdhury et al. (2011) reported that the breakthrough of nanoparticles increased with increasing nanoparticle concentration at pH 5 due to blocking and subsequent particle–particle repulsion. Fisher-Power and Cheng (2018) observed decreasing nTiO₂ recovery with time consistent with ripening behavior, where nTiO₂ already deposited provided favorable deposition sites and attracted nTiO₂ with reversed charges. Higher concentrations of colloids introduced to the media may lead to a more rapid filling of favorable attachment sites in comparison to lower concentrations (Bradford and Bettahar, 2006).

1.2.3.4. Straining

Straining is another mechanism that controls nanoparticle retention and transport. Straining is the retention of particles in the pore structure because of trapping of particles in pore throats that are too small to allow particle passage (Bayat et al., 2015; Bradford and Bettahar, 2006). Straining usually occurs when the ratio of the particle-to-collector diameter is greater than a certain value (e.g., 0.002), suggesting that straining is a likely phenomenon involved in the majority of scenarios (Chowdhury et al., 2011). In the larger pores, nanoparticle transport is more likely, while particle retention will occur at pore throats and grain junctions that are below a critical size. Fang et al. (2013) demonstrated that a high IS (50 mM) and a low pH resulted in the high retention of nTiO₂ due to the enhanced aggregation and straining. Researchers have recently discovered that straining should be considered a potentially important mechanism for colloid deposition (Bradford and Bettahar, 2006).

1.3. Theoretical considerations

1.3.1. Zeta potential and hydrodynamic diameter (HDD)

Zeta potential is known as a fundamental factor in determining the stability of a colloidal system, which is the potential difference between the dispersion medium and the stern layer of fluid attached to the dispersed particle (Kirby and Hasselbrink, 2004). The zeta potential is usually determined by electrophoresis, and the measured electrophoretic mobility can be converted to zeta potential through Smoluchowski's theories (Hassellöv et al., 2008). As long as particles have the same large charge, either negative or positive, the suspension will be stable due to the repulsive forces between the particles and the magnitude of the zeta potential determines the degree of electrostatic repulsion and eventually the stability of dispersion. In fact, higher zeta potential leads to higher stability while in case of lower zeta potential the tendency for flocculation will increase.

pH plays a considerable role in the magnitude of zeta potential as quoting a zeta potential without an accompanying pH is almost meaningless. In various suspensions with different pH, by plotting the zeta potential versus pH, it can be seen that isoelectric point for a particular value of solution pH is different from the other pH values at which the flocculation is predominant and the colloidal system is extremely unstable (Kirby and Hasselbrink, 2004).

Particle size characterization is of particular importance to nano particles. When a dispersed particle moves through a suspension, its surface is surrounded by an electric dipole layer, which influences the movement of the particle. Therefore, this thin layer is considered when measuring the particle size and is called hydrodynamic particle diameter which is measurable via dynamic light scattering (DLS). (Malvern Panalytical Ltd., 2018). This should be noted that hydrodynamic parameter is only applicable to particles in a dispersion or molecules in solution.

1.3.2. DLVO calculations

Various forces contribute to the interactions among colloid particles, including London-van der Waals forces, electrostatic interaction, steric forces, etc. London-Van der Waals forces exist due to permanent or temporary dipole in the particles and are depend on the geometry and nature of the particles as well as the properties of their surrounding media (Liu and Neretniek, 2010). The presence of electrical double layer and its effect on electrostatic interaction between colloids, results in repulsive force which is determined by particle properties, such as the magnitude of zeta potential, particle concentration, as well as electrolyte chemistry, including pH and ionic strength (Tiede et al., 2008).

The stability and aggregation of nanoparticles in aqueous environments are controlled by the interaction energy among particles, which is described by the Deyaguin-Landau-Verwey-Overbeek (DLVO) theory. In this theory, the total interaction is supposed to be the overall effect

of van der Waals and double layer interactions (Gregory, 1981; Hogg et al., 1966; Van Olphen, 1963). The magnitude of the interactions is determined by particle properties, such as zeta potential, size, concentration, and electrolyte chemistry, including pH and ionic strength (Tiede et al., 2008). The DLVO equations are provided in the Appendices Section.

1.3.3. Modeling nTiO₂ transport

Transport modeling has been a beneficial approach to predict and understand the particle transport behaviors (Bradford et al., 2003; Bradford and Bettahar, 2006; Chen et al., 2011; Torkzaban et al., 2012). Due to the lack of methods for modeling in complex environmental systems, predicting nanoparticles' transport can be challenging. Therefore, more in-depth investigation is needed on involved mechanisms in ENPs' transport under heterogeneous conditions, which could also assist in modeling the transport of nanoparticles. Basically, nanoparticle transport is modeled based on the classic advection-dispersion-reaction equation (Equations and details are provided in Appendix 2) (Liu et al., 2013). The models that have been reported are one-site deposition remobilization, two-site deposition remobilization, one-site deposition remobilization and blocking, one-site deposition remobilization and depth dependent retention, one-site deposition remobilization, blocking, and depth dependent retention (Goldberg et al., 2014). Although modeling is essential for the assessment of concentrations of ENPs in the environment, modeling on fate and transport of nanoparticles is still in its early stages, therefore, more investigation is suggested in this field, especially in complex environmental systems.

1.3.4. Adsorption isotherms

Regarding the importance of adsorption process in contaminant transport, there has been a steadily growing interest in the application of isotherms modeling. How an adsorbent perform can be investigated by adsorption isotherm data, which can be obtained by conducting adsorption tests.

Modeling the adsorption isotherm data is crucial for predicting and comparing the adsorption performance of various adsorbents, which, in turn, is very important for determining the adsorbents' capacities (Chen, 2015). The two-parameter isotherm models that are often applied in modeling the adsorption data include Langmuir, Freundlich, Temkin, and Dubinin-Radushkevich et al. (Chen, 2015; Dubinin, 1947; Freundlich, 1906; Langmuir, 1916; Tempkin and Pyzhev, 1940). In fact, a modeled adsorption isotherm is a non-linear curve demonstrating the adsorption performance of an adsorbent at a constant temperature and pH. The modeling analysis develops the mathematical form for the correlation between the equilibrium concentration of the adsorptive and surface adsorbate, which is important for operational design and application of the adsorption systems (Foo and Hameed, 2010).

1.4. Thesis objectives

From an environmental point of view, water chemistry can be complicated as a result of a combination of different factors affecting nanoparticle attachment and mobility. Many studies have investigated the effects of a single water chemistry condition (e.g., pH, IS, electrolyte valence) on the fate and transport of nTiO₂ in porous media. However, nTiO₂ can encounter multiple water chemistry conditions simultaneously in aquatic systems, yet their combined effects on the transport of nTiO₂ have not been investigated. In addition, few nTiO₂ transport studies have been carried out using natural soil and sediment as the porous medium (Fang et al., 2011, 2009; Sun et al., 2015b) to accurately represent complex aquifer materials and examine the interactions of nTiO₂ with heterogeneous soil and sediment components. Various sediment components affect nTiO₂ transport differently. Clay particles and SOM are mainly negatively-charged under natural environment conditions, whereas the surface charge of Fe-oxyhydroxide is normally positively charged and dependent on pH. To better understand nTiO₂ transport in natural systems, the effects

of water chemistry conditions and natural sediment components on nTiO₂ transport need to be simultaneously investigated. The objectives of this study are to elucidate the following:

(1) the effects of complex water chemistry conditions (e.g., the combined effect of anions and divalent cations at various pH) on the stability and attachment, of nTiO₂ by conducting batch experiments.

(2) the influence of complex water chemistry (e.g., the combined effect of anions and suspended clay particles at various pH) and heterogeneous porous media containing quartz sand and Fe oxyhydroxide- coated sand on nTiO₂ transport by conducting column experiments.

(3) the influence of heterogeneous porous media containing various natural components (e.g., Fe oxyhydroxides, natural organic matters, and clay particles) on nTiO₂ transport by conducting column experiments.

Phosphate and Ca²⁺ were used in Chapter 2 as examples of anions and divalent cations, respectively. Illite colloids were studied to find the differences between engineered nTiO₂ and naturally-occurring illite colloids under similar conditions. Transport media, with varying degrees of heterogeneity ranging from quartz sand, Fe-oxyhydroxide-coated quartz sand (Chapter 3), quartz sand mixed with natural sediment, and Fe-oxyhydroxide-coated quartz sand mixed with natural sediments (to investigate the effect of Fe oxyhydroxides, natural organic matters, and clay particles) were used to examine the effects of porous media properties on the transport of nTiO₂ (Chapter 4). This type of study advances the knowledge on nTiO₂ transport in natural systems and provides knowledge that elucidates the applicability of laboratory column experiments' results to the natural environment.

1.5. Co-authorship statement

I, Zahra Sadat Rastghalam, hereby declare that this thesis incorporates materials from my own research as follows: in all cases, literature review, experimental designs, data analysis and interpretation, and writing were performed by the principal author under the supervision and guidance of Dr. Tao Cheng. Chapter 2 of the thesis (Rastghalam, Z.S., Cheng, T., Freake, B., 2018. Fine particle attachment to quartz sand in the presence of multiple interacting dissolved components. *Sci. Total Environ.* 645, 499–508.) was co-authored with Dr. Tao Cheng and Bradley Freake. Chapters 3 (Rastghalam, Z.S., Yan, C., Shang, J., Cheng, T., 2019. Nanoscale titanium dioxide ($n\text{TiO}_2$) aggregation and transport in the co-presence of dissolved phosphate, illite colloid, and Fe oxyhydroxide coating. *Colloids Surfaces A Physicochem. Eng. Asp.* 578, 123560) was co-authored with Dr. Tao Cheng, Chaorui Yan, and Dr. Jianying Shang, and Chapter 4 (Rastghalam, Z.S., Yan, C., Shang, J., Cheng, T. The role of Fe oxyhydroxide coating, illite clay, and peat moss in nanoscale titanium dioxide ($n\text{TiO}_2$) retention and transport in geochemically heterogeneous media. (Submitted to *Environmental pollution*)) of the thesis was co-authored with Dr. Tao Cheng, Chaorui Yan, and Dr. Jianying Shang. Bradley Freake contributed to performing the NaCl electrolyte experiments in Chapter 2, and Chaorui Yan and Dr. Shang contributed to the modeling analysis in Chapters 3 and data analysis in Chapter 4.

Chapter 2. Fine particle attachment to quartz sand in the presence of multiple interacting dissolved components

(Rastghalam, Z.S., Cheng, T., Freake, B., 2018. Fine particle attachment to quartz sand in the presence of multiple interacting dissolved components. *Sci. Total Environ.* 645, 499–508).

Abstract

In natural aquatic systems water chemistry is complicated and fine particles encounter multiple water components simultaneously, yet the combined effects of some multiple components on the fate and transport of these particles have not been elucidated. In this study nTiO₂ and illite colloid attachment to quartz sand was investigated in 1 mM NaCl and 0.5 mM CaCl₂ background solutions using a range of phosphate concentrations (0 to 10 mg/L) at pH 5 and 9. The results obtained from the batch experiments indicated that without using phosphate, nTiO₂ aggregation and attachment was strongly influenced by pH and Ca²⁺, both of which modified nTiO₂ surface charges. nTiO₂ attachment was high in CaCl₂ solution at pH 9 due to attractive forces between nTiO₂ and sand, as well as ripening. Furthermore, phosphate adsorption to nTiO₂ was higher in CaCl₂ solution at pH 9 than that at pH 5 due to attractive forces between nTiO₂ and phosphate anions, and also potential surface precipitation of Ca-P minerals at pH 9. Phosphate adsorption to illite was low owing to strong repulsive forces between illite and phosphate. The effect of phosphate on nTiO₂ and illite attachment to sand was influenced by pH and cation valency. A decreasing trend in nTiO₂ attachment with phosphate addition was observed in NaCl solution at pH 5 and 9, and in CaCl₂ solution at pH 5; however, in CaCl₂ solution at pH 9, the surface charge of nTiO₂ reversed from negative to positive and a substantial amount of nTiO₂ attached to sand. Moreover, illite attachment to sand was much lower than that of nTiO₂ under all the conditions

tested in this study. These findings are important for understanding of the fate and transport of nTiO₂ and illite colloids in natural aquatic systems where various anions and cations co-exist.

Keywords: nanoscale titanium dioxide particles (nTiO₂); illite colloids; phosphate; precipitation of Ca-phosphate minerals; cation valency; DLVO theory

2.1. Introduction

Engineered nanoscale titanium dioxide (nTiO₂) has become an important functional substance that can be commonly found in many commercial products, including paints, skin care products, foods, pharmaceuticals, rubbers, papers, plastics, etc. (Loosli et al., 2013). It is estimated that by 2025, 2.5 million tons of nTiO₂ will be manufactured annually (Godinez et al., 2013; Robichaud et al., 2009). Once released to the environment, nTiO₂ may migrate through aquatic systems, posing a potential risk to human health and the environment (Chen et al., 2015; Du et al., 2011). nTiO₂, as well as clay colloids, may also attach to viruses and bacteria and influence their transport in porous media (Chowdhury et al., 2012; Gentile and Fidalgo de Cortalezzi, 2016; Syngouna and Chrysikopoulos, 2013; Syngouna et al., 2017). To predict the fate and transport of nTiO₂ and evaluate the consequences of nTiO₂ discharge into subsurface environments, it is important to comprehend the mechanisms governing nTiO₂ aggregation and attachment to sediment grains, since aggregation and attachment are the most important processes that immobilizes fine particles in groundwater. Previous studies have shown that water chemistry and components such as pH (Chowdhury et al., 2011), ionic strength (Godinez et al., 2013), major cations (e.g., Na⁺, Ca²⁺) (French et al., 2009; Akaike et al., 2012) and anions (e.g., phosphate) (Chen et al., 2015), dissolved organic matter (DOM) (Wu and Cheng, 2016), as well as clay colloids (Cai et al., 2014) all influence the stability and attachment of engineered nanoparticles.

Clay particles including kaolinite, montmorillonite, and illite colloids are also common in soil and groundwater (Wilson et al., 2014). Among different kinds of clay minerals, illite is demonstrated to have a great capacity as an adsorbent (Xie et al., 2013), due to small particle size and good bonding ability (Dror et al., 2012). Stability and aggregation of clay colloids (Jiang et al., 2012; Novich and Ring, 1984) and the impacts of clay colloids on the transport of contaminants have been extensively studied (Cai et al., 2014; Tang and Cheng, 2018; Zhou et al., 2012). However, most of the studies are conducted under simple water chemistry conditions that do not adequately represent typical groundwater in which various cations and anions commonly co-exist.

Phosphate is not one of the major anions commonly found in pristine natural water. However, due to the use of phosphorous fertilizers in agriculture, phosphate is discharged into the aquatic environment. Most of the metal oxides interact with phosphate, adsorb these anions, and control the behavior and fate of the phosphate in aquatic systems (Connor and McQuillan, 1999; Lv et al., 2012). In groundwater, phosphate may encounter different fine particles such as nTiO₂ and clay colloids. It has been reported that phosphate can adsorb to the surface of nTiO₂ and alter its size and surface charge (He et al., 2017). Whether phosphate facilitates or inhibits fine particle transport depends on water chemistry. For example, with increasing pH, phosphate adsorption to TiO₂ declines, whereas with increasing ionic strength, phosphate adsorption to nTiO₂ increases (Kang et al., 2011). Enhanced nTiO₂ transport in the presence of phosphate was observed at pH 7.5 compared to that at pH 6.5 due to the more negative charges on nTiO₂ surface at higher pH (Chen et al., 2015).

The valency and concentration of background solution also affected the stability and transport of fine particles (Akaiqhe et al. 2012; Torkzaban et al. 2012; Baalousha et al. 2013). Higher retention of colloidal particles occurred in the presence of divalent cations compared to that in solutions

with monovalent cations at the same ionic strength, due to the stronger screening effect of the divalent cations (McCarthy and McKay, 2004). Chen et al. (2011) highlighted that nTiO₂ retention in a sand column was higher when CaCl₂ instead of NaCl background solution was used, even though the Ca²⁺ concentration was lower than that of Na⁺. It has been reported that at high pH, strong adsorption of divalent cations converts the surface charge of nTiO₂ from negative to positive. The mechanism resulting in nTiO₂ surface charge reversal is Ca²⁺ adsorption at the rutile-water interface (Jang and Fuerstenau, 1986). Therefore, it can be anticipated that nTiO₂ particles in solutions with divalent cations at high pH might attract negatively charged phosphate ions. For clay particles, it has been demonstrated that there are many sites with a charge imbalance (due to isomorphic substitution) on particle surface, resulting in an excessive amount of negative charges. Hence, multivalent cations like Ca²⁺ can strongly bind to the clay particles (Sposito, 2008; Torkzaban et al., 2012).

Although many studies have evaluated the various factors (e.g. pH, ionic strength, anions, cations) affecting the aggregation and attachment of fine particles, the behaviours of these particles in natural water is difficult to predict, since chemistry of natural water is far more complicated due to the co-presence of multi-components and their combined effects on water-borne particles. For example, the stability and attachment of nTiO₂ in groundwater are influenced not only by the presence of cations or anions, but also by concentration of the ions and their co-existence. While phosphate may increase the stability of nTiO₂ (Chen et al., 2011), Ca²⁺ decreases stability by promoting the formation of nTiO₂ aggregates (Loosli et al., 2015). Furthermore, due to the low solubility of Ca-phosphate minerals at high pH, Ca-phosphate precipitates may form (Ronson and McQuillan, 2002) and this in turn may affect nTiO₂ properties (e.g. zeta potential and size), and eventually its stability and transport. Phosphate concentration was also shown to have considerable

impacts on the aggregation and dispersion of nTiO₂ via changing the particles' surface charge (He et al., 2017). Several studies have been conducted to understand the aggregation and attachment of nTiO₂ particles (Cai et al., 2015; Chen et al., 2015; Chowdhury et al., 2011; Fang et al., 2013; French et al., 2009; Godinez et al., 2013; Tang and Cheng, 2018; Wu and Cheng, 2016); however, no study has investigated the influence of simultaneous presence of phosphate anions and Ca²⁺ cations at different pH on nTiO₂ attachment. Such studies will allow us to produce results applicable to aquatic environments contaminated by phosphate and where Ca²⁺ is present.

This paper aims at investigating the combined effects of phosphate and major cations' valency on nTiO₂ and illite colloid attachment to quartz sand, a representing aquifer material. The mechanisms involved in the attachment process were studied by conducting systematic laboratory batch experiments using dilute NaCl and CaCl₂ background solutions, with different concentrations of phosphate at pH 5 and 9. Zeta potentials and hydrodynamic diameter (HDD) of nTiO₂ and illite colloids were measured and used in Derjaguin–Landau–Verwey–Overbeek (DLVO) calculations. The resulting DLVO interaction energy profiles between particles and between particle and sand were compared to the experimental measurements to explore both the applicability and limitations of the DLVO theory.

2.2. Materials and methods

2.2.1. Preparation of nTiO₂ and illite colloid suspensions, stock solutions, and quartz sand

The reagents used throughout the experiments were certified ACS grade. All the solutions and suspensions were prepared using nano-pure water generated by a Barnstead Nano-pure Infinity ultrapure water system (with resistivity >18.2 MΩ × cm and dissolved organic carbon (DOC) concentration < 0.02 mg/L).

Aeroxide[®] TiO₂ P25 powder was purchased (Fisher Scientific) with a reported 99.5% purity, specific surface area of 50 ± 15 m²/g, and an average particle size of 21 nm. The term nTiO₂ is used throughout this paper to refer to nanoscale titanium dioxide particles. Rutile and anatase are two mineral forms of TiO₂ and they may have substantially different behaviours (Sygouni and Chrysikopoulos, 2015). X-ray diffraction (XRD) results showed that the Aeroxide[®] TiO₂ P25 used in this study consists of 90% anatase (particles size = 23 nm) and 10% rutile (particle size = 40 nm) (Wu and Cheng, 2016). 500 mg/L nTiO₂ stock suspension was prepared by mixing an appropriate amount of dry powder and nano-pure water and sonicating the suspension for 30 min by a Branson Digital Sonifier (Crystal Electronics) with 200 W power to obtain a homogeneous stock suspension.

The illite stock was prepared by suspending 4.0 grams of illite powder (IMt-2 Illite Cambrianshale, The Clay Mineral Society) in 1000 mL of nano-pure water in a glass beaker. The suspension was first vigorously stirred and then sonicated for 30 minutes (200 W power) to disperse the illite particles. The suspension was sealed and left unmoved for 24 hours to allow the large particles to settle and the supernatant was then transferred to a high-density polyethylene (HDPE) bottle using a pipette. Concentration of the illite stock suspension was measured gravimetrically by filtering 100 mL of the supernatant through a 0.1 µm pore-size polyethersulfone membrane filter. The mass of the illite colloids was obtained by calculating the weight difference between the initial and the final mass of the filter (after being oven dried at 80 °C).

Stock solution of 100 mg/L phosphate was prepared by weighing (using an analytical balance) and dissolving an appropriate amount of NaH₂PO₄·H₂O powder (for experiments with CaCl₂ background solution) or KH₂PO₄ powder (for experiments with NaCl background solution)

in nano-pure water. NaCl, CaCl₂·2H₂O powder, and nano-pure water were used to prepare background stock solutions with the concentration of 0.1 M.

Quartz sand (U.S. Silica) was sieved to the size range of 0.6 – 0.7 mm, acid washed, and oven dried, following the procedure described by Wu and Cheng (2016). The acid washing procedure was to ensure the sand surfaces were free of trace quantities of metal oxides and organics, which might affect surface properties of the sand and interfere with adsorption and particle attachment.

2.2.2. Batch experiments

2.2.2.1. nTiO₂ and illite colloid attachment to quartz sand

nTiO₂ and illite colloid attachment to quartz sand was investigated by conducting batch experiments in 1 mM NaCl and 0.5 mM CaCl₂ background solution at pH of 5 and 9. To obtain isotherms of particle attachment in the absence of phosphate, a fixed amount of quartz sand (2.00 g) was mixed with the particles (nTiO₂ or illite colloid) at a range of particle concentrations (0 to 100 mg/L) in 15 mL Falcon tubes. To investigate how phosphate influence particle attachment to quartz sand, fixed amount of quartz sand (2.00 g) and particle (100 mg/L nTiO₂ or illite colloid) were mixed. The nTiO₂ concentration used was much higher than its expected concentrations in natural subsurface environment. This high concentration was needed to facilitate sample analysis and comparable to those used in similar studies (Cai et al., 2014; Chowdhury et al., 2011; Solovitch et al., 2010; Wu and Cheng, 2016). The mixtures were spiked with phosphate stock solution to achieve the desired phosphate concentrations (0, 2, and 10 mg/L). Concentration of the background solution was adjusted by diluting 0.1 M NaCl or 0.1 M CaCl₂ solution. Proper volume of nano-pure water was added to maintain a constant total solution volume of 10 mL in each tube. pH of the suspensions was adjusted to 5.0 ± 0.05 and 9.0 ± 0.2 using 0.1 M HCl and 0.1 M NaOH. All

the tubes were sealed with the screw-caps and the mixture was shaken on an orbital shaker (Model 5000, VWR International Co.) at ~300 rpm for 180 mins. pH of the suspensions was monitored periodically to maintain the intended pH during shaking. After 180 min shaking, sand grains were separated from the supernatant by allowing the sample to settle for 60 seconds, and optical absorbance of the supernatant was measured using a ThermoScientific Genesys 10S UV-VIS at wavelength of 368 nm and 290 nm for nTiO₂ and illite respectively. For illite attachment experiments in 1 mM NaCl solution, a slightly different wavelength (257 nm) was used for measuring the optical absorbance. Although it might take more than 180 min for particle attachment to reach equilibrium, this time scale was long enough to observe the effects of water chemistry on particle attachment under our experimental conditions. The concentrations of nTiO₂ and illite colloids in the supernatant were calculated based on the optical absorbance and calibration curves, and the concentration of particles attached to the sand was calculated as the difference between the initial and final concentration of particle in the supernatant. All the attachment experiments were performed in duplicate at room temperature (~22 °C).

2.2.2.2. Phosphate adsorption to nTiO₂, illite colloid, and quartz sand

To study phosphate adsorption to particles, proper amount of the nTiO₂ or illite stock suspension was aliquoted into 15 mL Falcon tubes to obtain a final particle concentration of 100 mg /L. To study phosphate adsorption to quartz sand, 2.00 g sand was weighed using an analytical balance and added to the tube. Concentration of the background solution was adjusted by diluting 0.1 M NaCl or 0.1 M CaCl₂ solution. The mixtures were spiked with phosphate stock solution to achieve the desired phosphate concentration range (0 to 10 mg/L) and pH was adjusted. These tests were performed using a procedure similar to that described in section 2.2.2.1. After the shaking time (180 min) elapsed, the nTiO₂ or illite suspensions were filtered through 0.22 μm

nylon membrane filters, and phosphate concentration in the filtrate was measured using the molybdenum blue method (Chen et al, 2015). The light absorbance of each sample was measured using a ThermoScientific Genesys 10S UV-VIS spectrophotometer at a wavelength of 830 nm. The amount of phosphate absorbed was calculated as the difference between the initial phosphate concentration and phosphate concentration in the filtrate. The mean particle diameters under our experimental conditions were all much larger than 0.22 μm , therefore, the filtration procedure could effectively remove these particles from the suspensions under most of the conditions. For experiments with quartz sand, the samples were not filtered. Instead, the sand was separated by leaving the tube unmoved for 60 seconds, and the supernatant was used for phosphate measurement. All the adsorption experiments were performed in duplicate at room temperature ($\sim 22\text{ }^{\circ}\text{C}$).

2.2.3. Zeta potential and hydrodynamic diameter (HDD) measurement

Fine particle suspensions of nTiO_2 and illite colloids with a concentration of 100 mg/L were prepared using the procedure described in Section 2.2.2.1, and their zeta potential and HDD in two types of background solutions (1 mM NaCl or 0.5 mM CaCl_2) at pH 5 and 9, and at three phosphate concentrations (0, 2, and 10 mg/L) were measured at room temperature ($\sim 22\text{ }^{\circ}\text{C}$). To prepare the quartz sand for zeta potential measurement, the sand was crushed using a laboratory pulverizer (TE250, Angstrom) before being suspended in 2000 mL nano-pure water in a container, and the mixture was then vigorously stirred and sonicated for 30 min with 200 W power. The container was left untouched overnight to let the large particles to settle, and the supernatant was transferred into another container for storage. This quartz particle stock suspension was used to prepare samples in 1 mM NaCl and 0.5 mM CaCl_2 solutions at pH 5 and 9, with three phosphate concentrations (0, 2, and 10 mg/L) for zeta potential measurement. In addition, nTiO_2 zeta

potential in phosphate-free 1 mM NaCl solution was measured as a function of pH in order to determine the point of zero charge (pH_{pzc}) of nTiO₂.

A zetasizer Nano-ZS (Malvern) was used to determine the zeta potential and HDD of the particle suspensions. Laser Doppler velocimetry coupled with phase analysis light scattering was utilized to measure particle electrophoretic mobility, which was then converted to zeta potential using the Smoluchowski equation. The HDD was measured based on dynamic light scattering (DLS) (Elimelech et al., 2013). The experiments were duplicated, and the results were the mean of the two measurements.

2.2.4. DLVO interaction energy calculation

To calculate the interaction energies between particle-particle and between particle-sand, Derjaguin–Landau–Verwey–Overbeek (DLVO) theory (Van Olphen, 1963) was applied, with the assumption of sphere-sphere and sphere-plate geometry, respectively. For particle-particle energies, the Van der Waals (LW) and electrostatic double layer (EDL) energies were calculated according to Equation 1 and 2 respectively (Gregory, 1981; Hogg et al., 1966; Sun et al., 2015b). The Van der Waals and electrostatic double layer energies for particle-sand were calculated utilizing Equation 3 and 4 respectively (Gregory, 1981; Hogg et al., 1966; Sun et al., 2015b). The total particle-particle and particle-sand interaction energy is the sum of the LW and EDL energies.

$$\phi_{\text{LW}} = -\frac{A r_p}{12D} \left[1 + \frac{14D}{\lambda}\right]^{-1} \quad (1)$$

$$\phi_{\text{EDL}} = 2\pi \varepsilon_0 \varepsilon_r r_p \psi_p^2 \ln [1 + \exp(-\kappa D)] \quad (2)$$

$$\phi_{\text{LW}} = -\frac{A r_p}{6D} \left[1 + \frac{14D}{\lambda}\right]^{-1} \quad (3)$$

$$\phi_{\text{EDL}} = \pi \varepsilon_0 \varepsilon_r r_p \left\{ 2\psi_p \psi_s \ln \left[\frac{1 + \exp(-\kappa D)}{1 - \exp(-\kappa D)} \right] + (\psi_p^2 + \psi_s^2) \ln [1 - \exp(-2\kappa D)] \right\} \quad (4)$$

where A is Hamaker constant for particle-water-particle and particle-water-sand interactions, r_p refers to the radius of the particle, D is separation distance, and λ is the characteristic wavelength of interaction, usually taken to be 100 nm (Elimelech et al., 1995). ϵ_0 ($8.85 \times 10^{-12} \text{ C}^2\text{J}^{-1}\text{m}^{-1}$) is the permittivity of vacuum, ϵ_r (80) is the relative dielectric constant of the medium, ψ_p (V) and ψ_s are the zeta potential of particle and sand, and κ (m^{-1}) is the Debye–Hückel reciprocal length and can be calculated using Equation 5.

$$\kappa = \left(\frac{e^2 \sum n_{i0} z_i^2}{\epsilon_0 \epsilon_r k_B T} \right)^{1/2} \quad (5)$$

where e is the electron charge (1.602×10^{-19} coulombs), n_{i0} is the number concentration of ion i in the bulk solution (m^{-3}), z_i is the valence of ion i in bulk solution, k_B is the Boltzmann constant ($1.38 \times 10^{-23} \text{ m}^2 \text{ kg s}^{-2} \text{ K}^{-1}$), and T is the absolute temperature (K) of the system.

For particle-particle interactions, a Hamaker constant (A) of 3.5×10^{-20} J was used for nTiO₂-water-nTiO₂ (Gómez-Merino et al., 2007), and 2.2×10^{-20} J for illite-water-illite (Long et al., 2006). For particle-sand interactions, a Hamaker constant (A) of 1.4×10^{-20} J was used for nTiO₂-water-sand (Butt et al., 2005; Petosa et al., 2010; Wu and Cheng, 2016), and for illite-water-sand, $A = 6.31 \times 10^{-21}$ J was calculated using Equation 6.

$$A_{132} = (\sqrt{A_{11}} - \sqrt{A_{33}})(\sqrt{A_{22}} - \sqrt{A_{33}}) \quad (6)$$

In this study 1 is illite, 2 is quartz sand, and 3 is water. The following constants were applied in Equation 6: $A_{\text{illite-illite}} = 8.60 \times 10^{-20}$ J (Médout-Marère, 2000), $A_{\text{SiO}_2\text{-SiO}_2} = 6.55 \times 10^{-20}$ J (Hough and White, 1980), and $A_{\text{H}_2\text{O-H}_2\text{O}} = 3.7 \times 10^{-20}$ J (Israelachvili, 2011).

2.3. Results and discussion

2.3.1. nTiO₂ and illite colloid aggregation

The HDD of nTiO₂ in 1 mM NaCl solution demonstrated low aggregation (i.e. HDD < 1000 nm) at pH 5 in the absence of phosphate, and at pH 9 with or without phosphate (Fig. 1-a & 1-b).

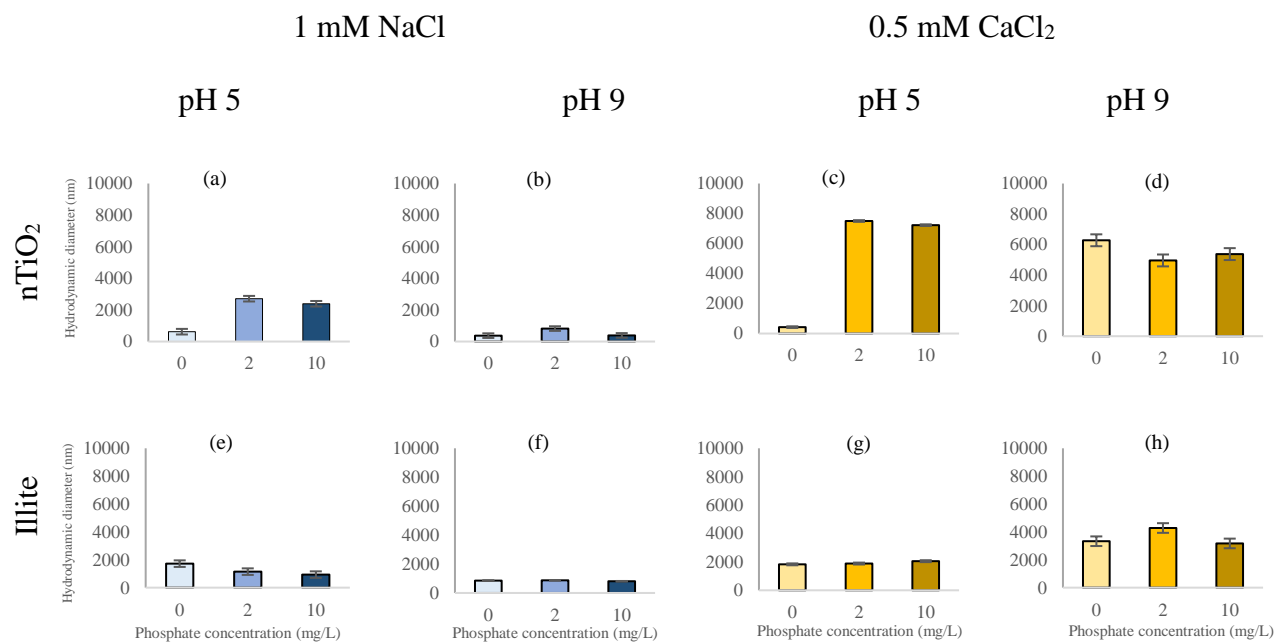


Fig. 1. Hydrodynamic diameter (HDD) (z-average) of nTiO₂ and illite in 1 mM NaCl (blue columns) and 0.5 mM CaCl₂ (orange columns) solutions at pH 5 and 9. Increasing color intensity indicating increasing PO₄³⁻ concentration (0, 2, and 10 mg/L).

These results were consistent with the predicted high energy barrier between the particles (Fig. S1-a & S1-c, Supporting Information (SI)), and in agreement with previous results under similar conditions (Tang and Cheng, 2018).

At phosphate concentrations of 2 and 10 mg/L, moderately large aggregates were formed at pH 5 (2390-2710 nm) (Fig. 1-a). At a phosphate concentration of 2 mg/L, a low magnitude of zeta potential (-8.5 mV) (Fig. 2-a) and the resultant low energy barrier (7.8 k_BT) with a secondary minimum of -0.9 k_BT might have contributed to aggregation (Fig. S1-a, SI).

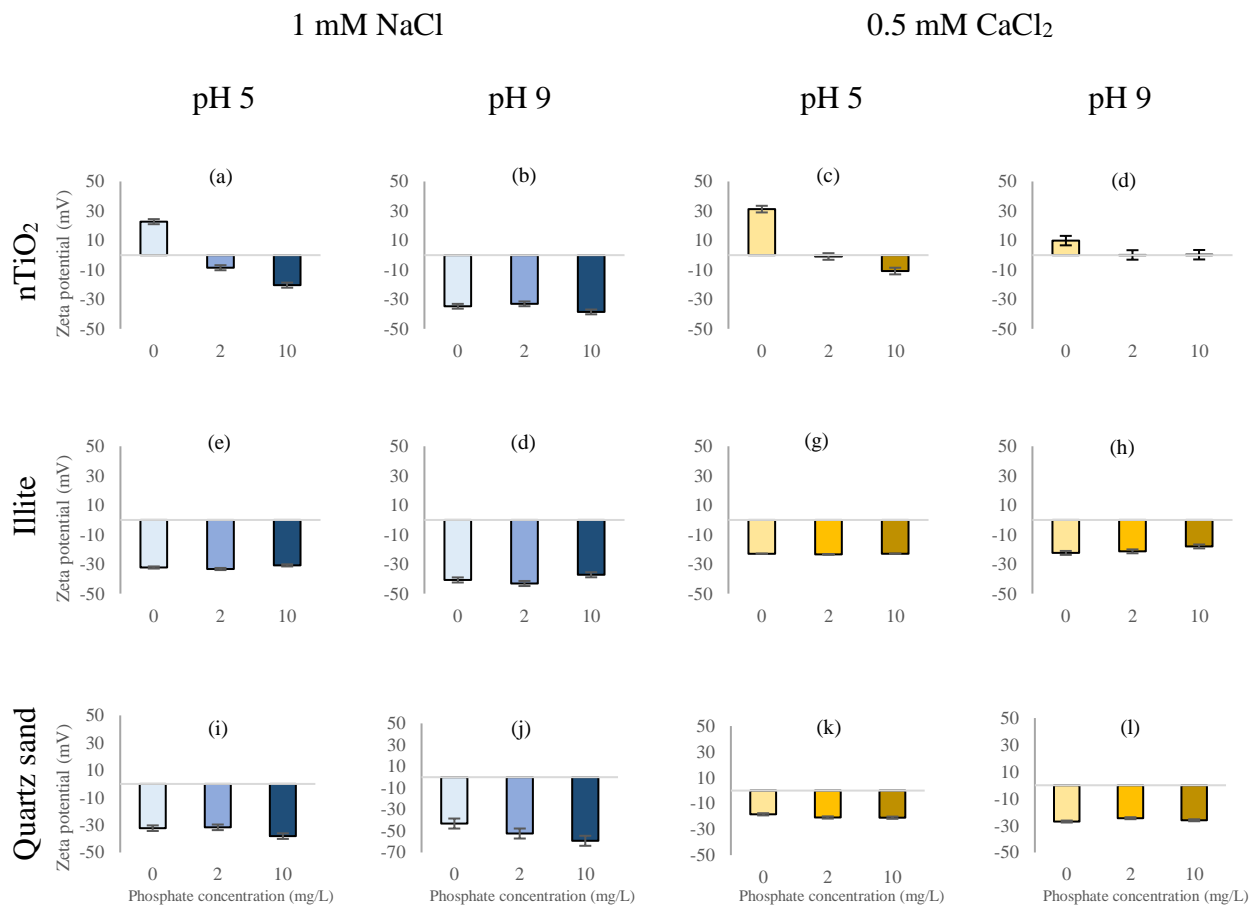


Fig. 2. Zeta potential of nTiO₂, illite, and quartz sand in 1 mM NaCl (blue columns) and 0.5 mM CaCl₂ (orange columns) solutions at pH 5 and 9. Increasing color intensity indicating increasing PO₄³⁻ concentration (0, 2, and 10 mg/L).

However, the energy barrier and secondary minimum by themselves were not strong enough to cause aggregation when compared with a mean kinetic energy of 1.5 k_BT for colloid particles reported by Treumann et al. (2014). At a phosphate concentration of 10 mg/L, where high energy barrier (155.9 k_BT) was calculated with no secondary minimum (Fig. S1-a, SI), the high HDD cannot be explained by the DLVO theory. nTiO₂ aggregation in the presence of phosphate was probably related to the bridging effect, i.e., phosphate was adsorbed by two nTiO₂ particles and therefore served as a bridge to connect the particles. Previous study showed that phosphate binds strongly to colloidal TiO₂ particles as a bidentate surface species and may potentially serve as a bridge between particles (Connor and McQuillan, 1999).

For CaCl₂ solution, considerable difference in aggregation was observed at pH 5 and 9 in the absence of phosphate (Fig. 1-c & 1-d). The HDD of nTiO₂ were 425.2 and 6282.4 nm at pH 5 and 9 respectively. At pH 5, the low aggregation was attributable to the high energy barrier (89.9 k_BT) (Fig. S1-b, SI), whereas at pH 9, the high aggregation was explained by the low energy barrier (16.4 k_BT) and a relatively deep secondary minimum (-3.6 k_BT) (Fig. S1-d, SI).

In CaCl₂ solution, much larger nTiO₂ aggregates (up to 7501.5 nm) were observed in the presence of phosphate compared to that of NaCl solution at pH 5 (Fig. 1-c vs. 1-a; Fig. 1-d vs. 1-b). Calculated DLVO interaction energy profiles demonstrated favorable aggregation conditions at pH 9 for both phosphate concentrations (2 and 10 mg/L), and at pH 5 when phosphate concentration = 2 mg/L (Fig. S1-b & S1-d, SI), consistent with the large HDD observed. The large HDD at pH 5 with 10 mg/L phosphate was due to a notable secondary minimum (-6.7 k_BT) and low energy barrier (11.8 k_BT) (Fig. S1-b, SI). The aggregation of nTiO₂ also influenced its attachment to the quartz sand, which was discussed in the subsequent sections.

The aggregation of illite colloids were less sensitive to changes in pH and phosphate concentration, but noticeably influenced by cation valency. In NaCl solutions, the HDD were generally low (935.8 to 1723 nm at pH 5, and 810.5 to 874.5 nm at pH 9) (Fig. 1-e & 1-f), whereas in CaCl₂ solutions, the HDD were higher (1829.0 to 2052.2 nm at pH 5, and 3172.8 to 4280.3 nm at pH 9) (Fig. 1-g & 1-h). In contrast to nTiO₂, very large aggregates (HDD > 5000 nm) were not formed under any of the conditions for illite colloids.

DLVO energy profiles showed high energy barriers between illite colloids in NaCl solutions at both pH (Fig. S2-a & S2-c, SI), in agreement with the low aggregation observed. It was also noted that changing phosphate concentration did not have a considerable impact on the zeta potential of illite (Fig. 2-e to 2-h). The relatively large HDD in CaCl₂ solutions was presumably due to the less negative zeta potentials (Fig. 2-e to 2-h), and therefore lower energy barriers (Fig. S2, SI). Overall, aggregation is not considered as a critical process affecting illite attachment to the quartz sand.

2.3.2. Effect of cation valency on nTiO₂ and illite colloid attachment to quartz sand

In NaCl solution at pH 5 substantial nTiO₂ attachment to the quartz sand was observed (Fig. 3-a).

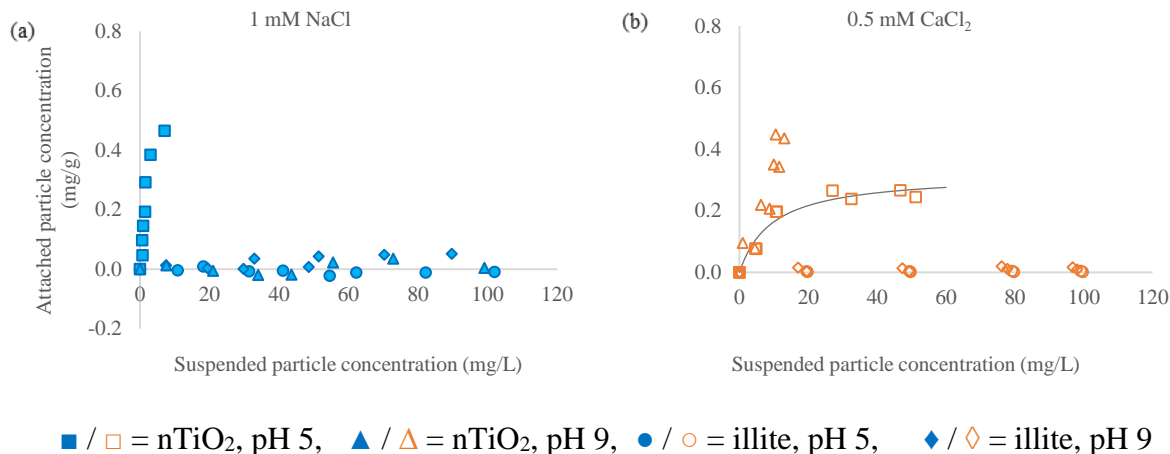


Fig. 3. Attachment of nTiO₂ and illite to 2 g quartz sand in the absence of the phosphate. Total nTiO₂ and illite concentrations varied from 0 to 100 mg/L in 1 mM NaCl (a) and 0.5 mM CaCl₂ solutions (b). Symbols: experimental measurements; line: simulated Langmuir adsorption isotherm. R² of the fitting and calculated q_{max} are 0.95 and 0.32 mg/g respectively for CaCl₂ solution at pH 5.

Attached nTiO₂ concentration increased with suspended particle concentration without showing a plateau, indicating that attachment saturation was not reached. The maximum attached concentration was 0.46 mg/g under the experimental conditions. At pH 9, nTiO₂ attachment was practically zero (Fig. 3-a). Other studies (Chowdhury et al., 2011; Fang et al., 2013; Virkutyte et al., 2014) also found high nTiO₂ attachment to sand at pH below the p*H*_{pzc} of nTiO₂, and low attachment at pH higher than the p*H*_{pzc}. p*H*_{pzc} of the nTiO₂ in this study was determined to be ~6.8 (Fig. S3, SI), close to the values previously reported (Loosli et al., 2013; Zhou and Cheng, 2018). Very low nTiO₂ adsorption capacity of quartz sand in column experiments at high pH in dilute monovalent cation background solutions was reported previously. Zhou and Cheng (2018) showed an adsorption capacity of 0.005 mg/g in 1 mM NaCl solution at pH 9. Toloni et al. (2014) found the adsorption capacity of quartz sand in 5 mM KCl solution at pH 10 ranging from 0.006–0.06 mg/g, depending on water velocity. The high nTiO₂ attachment at pH 5 can be explained by the

attractive electrostatic forces between the positively charged nTiO₂ (+22.7 mV) and negatively charged quartz sand (-32.3 mV) (Fig. 2-a & Fig. 2-i). At pH 9, however, both nTiO₂ and quartz sand were negatively charged, resulting in low attachment. The interaction energy between nTiO₂ and quartz sand calculated based on DLVO theory confirmed attractive forces at pH 5 (Fig. S4-a, SI) and high energy barriers at pH 9 (Fig. S4-c, SI), consistent with our experimental results.

In contrast to that in NaCl solution (Fig. 3-a), nTiO₂ attachment to quartz sand in CaCl₂ solutions was substantial at both pH (Fig. 3-b). In addition, the attachment in CaCl₂ solution was lower at pH 5 but higher at pH 9 (Fig. 3-b). At pH 5 in CaCl₂ solution, the attached concentration increased with suspended concentration and reached a plateau of ~0.25 mg/g (Fig. 3-b). At pH 9, attached concentration increased linearly with suspended concentration without reaching a plateau (Fig. 3-b). The sharp increase and linear pattern of the isotherm at pH 9 indicated high capacity for nTiO₂ adsorption and that the majority of the surface sites were not occupied. Langmuir adsorption isotherm model adequately simulated nTiO₂ attachment for pH 5 and showed an adsorption capacity (calculated q_{\max}) of 0.32 mg/g. nTiO₂ adsorption capacity of a pre-cleaned quartz sand with grain diameter range of 0.425–0.600 mm in 1 mM NaCl solution at pH 5 was reported as 0.29 mg/g (Wu and Cheng, 2016), comparable to the adsorption capacity determined in this study for quartz sand in 0.5 mM CaCl₂ solution at the same pH. Based on a specific surface area of 0.128 m²/g (Solovitch et al., 2010) for pre-cleaned quartz sand with a mean grain diameter of 650 μm (the same as the mean sand-grain diameter of this study), the surface-area normalized adsorption capacity of the sand under our experimental conditions was calculated as 2.50 mg/m².

The high nTiO₂ attachment in CaCl₂ solution at both pH was due to the positive zeta potentials of nTiO₂ in CaCl₂ solution (Fig. 2-c & 2-d). Even at pH 9, the zeta potential of nTiO₂ was positive in CaCl₂ solution, and therefore, nTiO₂ were strongly attracted by the negatively

charged quartz sand (Fig. 2-k & 2-l). DLVO calculations confirmed no energy barrier between nTiO₂ and sand in CaCl₂ solution at both pH (Fig. S4-b & S4-d, SI).

The much higher nTiO₂ attachment to sand at pH 9 compared to that at pH 5 in CaCl₂ solution cannot be explained by the calculated interaction energy between nTiO₂ and sand based on DLVO theory, i.e., the nTiO₂ and sand were oppositely charged for either pH (Fig. 2), and the magnitude of the particle-sand attractive interaction energies at pH 5 and 9 were similar (Fig. S4-d, SI). The higher deposition at pH 9 was attributable to ripening, which has been shown to promote nTiO₂ attachment to quartz sand (Chen et al., 2012). As described in Section 2.3.1, particle-particle interaction energy profile at pH 9 showed a relatively deep secondary minimum (-3.6 k_BT) and low energy barrier (16.4 k_BT), suggesting potential of aggregation and ripening. The favorable condition for aggregation was confirmed by the large particle size measured in CaCl₂ solution at pH 9 (HDD = 6282.3 nm) (Fig. 1-d). Therefore, at pH 9, nTiO₂ not only attached to quartz sand surface via electrostatic attraction, but also to the previously attached nTiO₂ via ripening, resulting in higher nTiO₂ attachment. At pH 5, conversely, the energy barrier between nTiO₂ particles was high (89.9 k_BT) with no secondary minimum, and the measured particle size confirmed no aggregation (HDD = 425.1 nm) (Fig. 1-c). Consequently, the only attachment mechanism was electrostatic attraction between particle and quartz sand surface.

Illite showed zero or close to zero attachment to the sand in both NaCl and CaCl₂ solutions (Fig. 3). The low attachment was due to the repulsive forces between illite colloid and the quartz sand, both of which were negatively charged in all our experiments. Previous studies using column experiments showed that the adsorption capacity of clean quartz sand for illite colloids in 1 mM NaCl solution in the pH range of 4.6–7.4 was zero (Gao and Saiers, 2004), consistent with our observations. Although Ca²⁺ cations in solution led to less negative charges on the illite surface

(Fig. 2-g & 2-h), the reduction in the absolute values of the zeta potential was not sufficient to considerably enhance illite attachment. This may be caused by a relatively low amount of Ca^{2+} in the systems. Jiang et al. (2012) illustrated that the illite particle diameter was not sensitive to the presence of Ca^{2+} or Na^+ in the solutions with a concentration of 1 mM or lower. DLVO calculations confirmed the presence of sizable energy barriers between illite colloids and sand under all the conditions tested (Fig. S5, SI).

2.3.3. Phosphate adsorption to nTiO₂, illite colloid, and quartz sand

In NaCl solution at pH 5, phosphate had notable adsorption to the nTiO₂, and the adsorbed concentration (q) increased with the aqueous concentration (C_{aq}) until the maximum adsorbed concentration was reached ($q_{\text{max}} = \sim 4.8 \text{ mg/g}$) (Fig. 4-a).

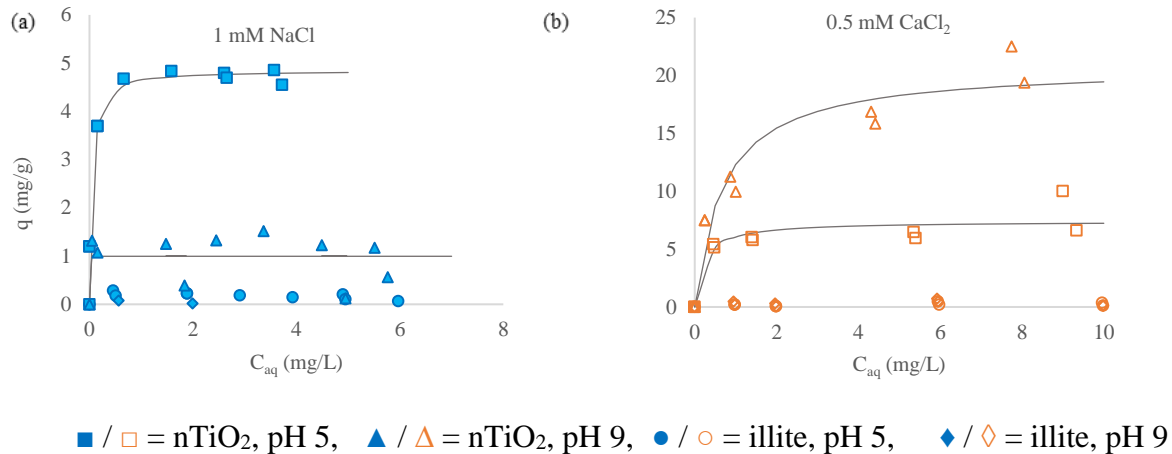


Fig. 4. Adsorption of the phosphate to nTiO₂ and illite colloid in 1 mM NaCl (a) and 0.5 mM CaCl₂ solutions (b) at pH 5 and 9. Particle concentration in all the experiments was 100 mg/L. q (mg/g) is adsorbed phosphate concentration and C_{aq} (mg/L) is aqueous phosphate concentration after 3 hours of mixing. Symbols: experimental measurements; lines: simulated Langmuir adsorption isotherms. R^2 of the fitting are 0.91 (pH 5) and 0.31 (pH 9) for NaCl solution, and 0.87 (pH 5) and 0.94 (pH 9) for CaCl₂ solution. Calculated q_{max} for NaCl solution at pH 5 and 9 are 4.9 and 1.0 mg/g respectively, and CaCl₂ solution are 7.3 and 20.8 mg/g respectively.

At pH 9, phosphate adsorption was much lower, with $q_{max} = \sim 1.2$ mg/g. These results are consistent with previous studies which showed that phosphate adsorption to nTiO₂ was pH dependent and decreased with increasing pH (Chen et al., 2015; Kang et al., 2011). Langmuir adsorption isotherm model simulated the experimental isotherm reasonably well at both pH, and the maximum adsorption capacity (calculated q_{max}) based on Langmuir isotherm were 4.9 and 1.0 mg/g, respectively, close to the experimental measurements.

The pH dependence of phosphate adsorption to nTiO₂ was attributable to the zeta potential change of nTiO₂. When pH is above the point of zero charge (pH_{pzc}) of nTiO₂, nTiO₂ becomes negatively charged due to H⁺ dissociation from functional groups (Tang and Cheng, 2018). In our experiments, the zeta potentials of nTiO₂ in NaCl solution in the absence of phosphate were +22.7

mV at pH 5 and -34.7 mV at pH 9 (Fig. 2-a & 2-b). Our measured zeta potentials were in agreement with the measured $\text{pH}_{\text{pzc}} \sim 6.8$ for nTiO_2 in dilute NaCl solutions and explained the higher adsorption at pH 5 and lower adsorption at pH 9, since phosphate is negatively charged at these pH. Additionally, phosphate becomes more negative at higher pH, i.e., H_2PO_4^- is the dominant species in the pH range of 2.1–7.2; however, in the pH range of 7.2–12.7, the dominant phosphate species is HPO_4^{2-} (Kang et al., 2011), which is more negative and repelled more by the negatively-charged nTiO_2 .

In CaCl_2 solution, phosphate adsorption was higher than that in NaCl solution (Fig. 4-b vs. 4-a), and the influence of pH on phosphate adsorption was different from that in NaCl solution (Fig. 4-a), i.e., in CaCl_2 solution, phosphate adsorption at pH 5 was lower than that at pH 9. In CaCl_2 solution at pH 5, the adsorbed phosphate concentration plateaued at ~ 6.6 mg/g when $C_{\text{aq}} > 1$ mg/L. At pH 9, the adsorbed phosphate concentration increased with increasing C_{aq} and then levelled off at ~ 20 mg/g. Langmuir adsorption isotherm model showed that the maximum adsorption capacity (calculated q_{max}) were 7.3 and 20.8 mg/g respectively at pH 5 and 9 in CaCl_2 solution, close to the experimentally measured maximum adsorbed concentrations.

The higher phosphate adsorption in CaCl_2 solution was due to the change of nTiO_2 zeta potential in the presence of Ca^{2+} . At pH 5, the zeta potential of nTiO_2 was +31.2 mV in CaCl_2 solution in the absence of phosphate (Fig. 2-c), more positive compared to that in NaCl solution (+22.7 mV) (Fig. 2-a), which resulted in higher attractive forces between nTiO_2 and phosphate, and therefore higher phosphate adsorption (i.e., $q_{\text{max}}(\text{CaCl}_2) > q_{\text{max}}(\text{NaCl})$).

At pH 9 in CaCl_2 solution, the zeta potential of nTiO_2 was positive (+9.8 mV) in the absence of phosphate (Fig. 2-d). The positive zeta potential at this high pH is presumably caused by Ca^{2+} adsorption to nTiO_2 (Loosli et al., 2015). As previously discussed, phosphate possesses

negative charges at both pH 5 and 9. Therefore, the positive surface charge of nTiO₂ resulted in strong attraction between phosphate and nTiO₂, and hence high phosphate adsorption at pH 9 in CaCl₂ solution.

In CaCl₂ solution, the higher phosphate adsorption at pH 9 compared to that at pH 5 cannot be justified based on the zeta potentials at these pH, i.e., at pH 9, the zeta potential was less positive compared to that at pH 5 (+9.8 vs. +31.2 mV), and the less positive zeta potential should lead to lower rather than higher adsorption. At pH 9, the solution was over-saturated with hydroxyapatite (Ca₅(PO₄)₃(OH)), as shown by the saturation index (SI = 14.37) calculated by Visual MINTEQ 3.0 (Gustafsson, 2010). However, phosphate removal from the aqueous phase was not observed in the illite experiments under the same water chemistry conditions (Fig. 4-b), indicating precipitation was probably kinetically hindered. The high phosphate adsorption is more likely due to surface precipitation of Ca²⁺ and phosphate on nTiO₂. The strong binding of Ca²⁺ to nTiO₂ at high pH increases Ca²⁺ concentration near the surface of nTiO₂ and causes further phosphate adsorption. The induced phosphate adsorption may occur via Ca²⁺, which could serve as a linkage to the previously adsorbed phosphate (Ronson and McQuillan, 2002). Previous studies showed that the influence of Ca²⁺ on phosphate adsorption is more significant at higher pH (Rietra et al., 2001; Ronson and McQuillan, 2002)

Phosphate adsorption to the illite colloids was much lower compared to that to nTiO₂. At pH 5 and 9 in NaCl solution, the maximum adsorbed phosphate concentration on illite was ~0.2 and ~0.02 mg/g, respectively (Fig. 4-a). In CaCl₂ solution, phosphate adsorption to illite was also low, but slightly higher than that in NaCl solution, i.e., up to 0.4 mg/g at pH 5 and up to 0.7 mg/g at pH 9 (Fig. 4-b). Zeta potential of illite remained highly negative in all NaCl and CaCl₂ solutions when the pH changed from 5 to 9 (Fig. 2-e – 2-h), which is consistent with the point of zero charge

for illite ($\text{pH}_{\text{pzc}} = \sim 2.5$) (Hussain et al., 1996). Therefore, strong repulsive force existed between illite and phosphate, leading to low adsorption. The slightly higher phosphate adsorption in CaCl_2 solution was due to the less negative zeta potential of illite in the presence of Ca^{2+} (Fig. 2-e – 2-h), resulting in lower repulsive forces. Divalent cations such as Ca^{2+} and Mg^{2+} adsorb to clay minerals via cations exchange sites (Torkzaban et al., 2012) and partially neutralize the negative charges of clay minerals. Additionally, divalent cations are more effective in screening the charges of clay colloids, resulting in less negative zeta potential (Tang and Cheng, 2018).

It should be noted that the pore size of the filter ($0.22 \mu\text{m}$) used in our phosphate adsorption experiments for separating the particles (nTiO_2 and illite) from the dissolved phase was smaller than the mean HDD under all the conditions (Fig. 1), indicating that most of the particles could be effectively removed. However, in the suspensions with small HDD (i.e., $\text{HDD} < 800 \text{ nm}$), particle size distribution determined by the zetasizer indicated that a small fraction of the nTiO_2 particles had diameter $< 0.22 \mu\text{m}$ (data not shown), suggesting that these smaller particles may pass through the filter and cause under-estimation of phosphate adsorption. Nonetheless, under most of the conditions, even the smallest nTiO_2 particles in the suspensions were larger than $0.22 \mu\text{m}$. Therefore, the filtration method used in our experiments was a reasonable method for separating the particles from the dissolved phase.

Phosphate adsorption to quartz sand was practically zero in both NaCl and CaCl_2 solutions at both pH ($< 0.002 \text{ mg/g}$ in NaCl solutions, $< 0.005 \text{ mg/g}$ in CaCl_2 solutions) (data not shown). The zeta potential of sand in NaCl solution was highly negative (-32.3 mV) at pH 5 and became more negative (-43.1 mV) as the pH increased to 9 (Fig. 2-i & 2-j). The zeta potentials of the sand in CaCl_2 solution were less negative (-18 mV and -27 mV at pH 5 and 9, respectively) (Fig. 2-k & 2-l). Quartz sand has been shown to have negative zeta potentials above $\text{pH}_{\text{pzc}} = 2.44$ in various

background solutions (e.g. NaCl and CaCl₂ solution) under low ionic strength conditions (Elimelech et al., 2000; Jada et al., 2006; Kaya and Yukselen, 2005). Kaya and Yukselen (2005) explained that Ca²⁺ can compress the diffuse electrical double layer of quartz, resulting in a considerable increase in zeta potential; yet, it does not reverse the surface charge of quartz sand. The strong repulsive forces between highly negatively charged sand and phosphate under our tested conditions contributed to the low phosphate adsorption. Additionally, hydroxyl surface functional groups on quartz sand surface are fairly unreactive in comparison to the reactive exchangeable sites on clay minerals' surfaces (Konecny, 2001), which also contributed to the low phosphate adsorption to quartz sand.

2.3.4. Effect of phosphate on nTiO₂ and illite colloid attachment to quartz sand

In NaCl solution, the attachment of nTiO₂ to the sand surface decreased in the presence of the phosphate (Fig. 5-a).

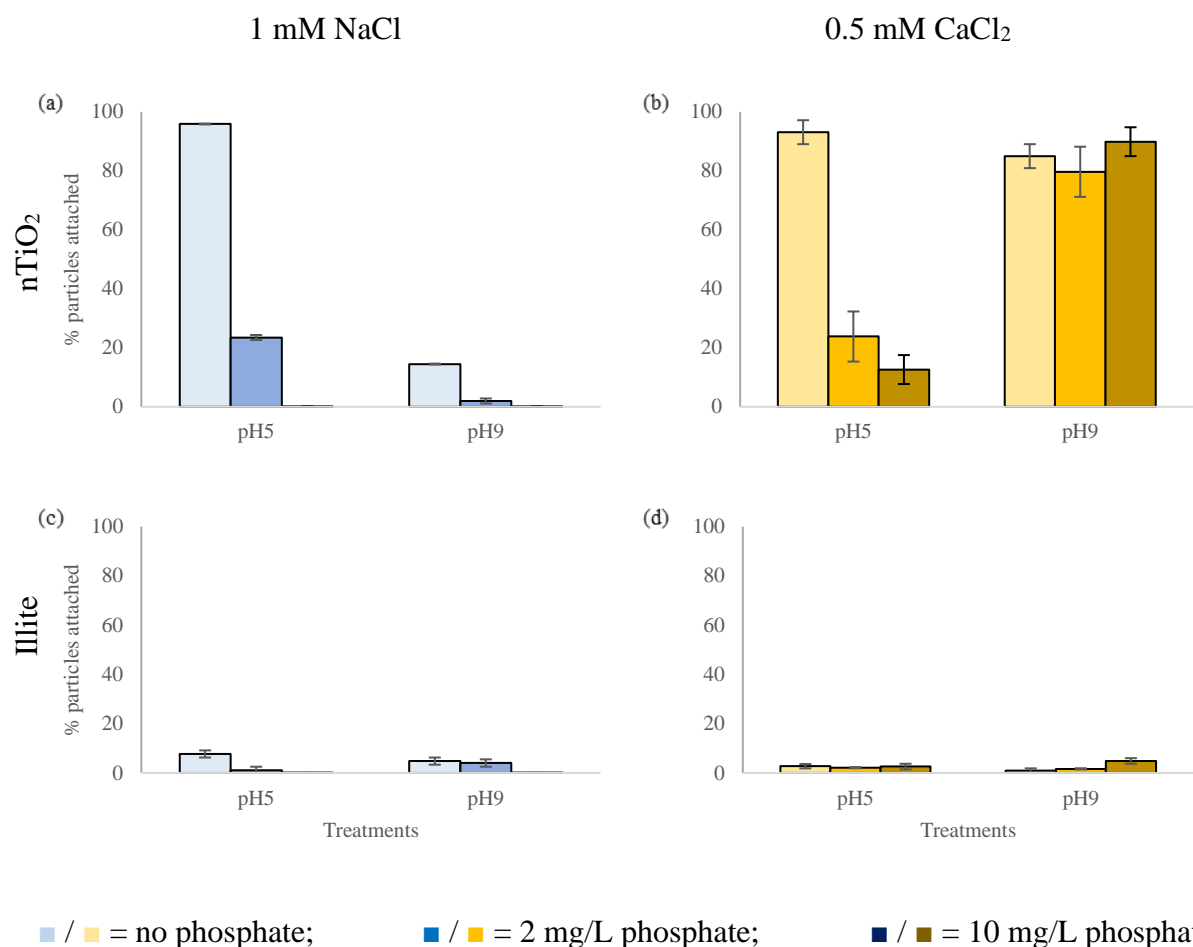


Fig. 5. Attachment of 100 mg/L nTiO₂ (a, b) and 100 mg/L illite (c, d) to 2 g quartz sand in 1 mM NaCl (a, c) and 0.5 mM CaCl₂ solutions (b, d) at pH 5 and 9. Increasing color intensity indicating increasing PO₄³⁻ concentration (0, 2, and 10 mg/L).

The decrease in attachment was the result of the changes in the zeta potential of nTiO₂ (Fig. 2-a). In the absence of phosphate, zeta potential of the nTiO₂ was positive (+22.7 mV) at pH 5, therefore, there was strong attraction between nTiO₂ and the negatively charged quartz sand, resulting in high attachment. Percentage of particle attached reduced to ~24% in the presence of 2 mg/L phosphate (Fig. 5-a), due to the lower zeta potential of nTiO₂ (-8.5 mV) (Fig. 2-a). The negative surface charge of nTiO₂ implies repulsion between nTiO₂ and the negatively charged quartz surface, which limited nTiO₂ attachment. A further increase in phosphate concentration to

10 mg/L resulted in a zeta potential of -20.3 mV (Fig. 2-a), and consequently a further reduction in nTiO₂ attachment (Fig. 5-a). At pH 9, nTiO₂ attachment also decreased with increasing phosphate concentration, and was generally much lower than that at pH 5, with the percentage of particle attached ranging from 15% to zero (Fig. 5-a). The low attachment at pH 9 is attributable to the negative zeta potentials of nTiO₂ at this high pH (Fig. 2-b), and the presence of phosphate slightly decreased the zeta potential and therefore nTiO₂ attachment. The influence of phosphate on nTiO₂ attachment can be explained by the interaction energy between nTiO₂ and the quartz sand (Fig. S4, SI). At pH 5, phosphate changed the overall interaction energy from attractive to repulsive (Fig. S4-a, SI), while at pH 9, the overall interaction energies were repulsive both in the absence and presence of phosphate (Fig. S4-c, SI). Chen et al. (2015) reported similar results, showing that the presence of phosphate favored the transport of nTiO₂ in quartz sand columns, due to the more negative charges and greater repulsive forces between nTiO₂ and the quartz sand.

In CaCl₂ solution, nTiO₂ attachment was generally much higher than that in NaCl solution (Fig. 5-b). At pH 5, phosphate also decreased nTiO₂ attachment in CaCl₂ solution, however, even at a phosphate concentration of 10 mg/L, nTiO₂ attachment was still substantial in CaCl₂ solution (~13%) (Fig. 5-b). When phosphate concentration was zero or 2 mg/L, the high attachment in CaCl₂ solution was caused by the positive or close to zero zeta potential (Fig. 2-c), which resulted in attractive DLVO forces between nTiO₂ and the sand (Fig. S4-b, SI). At a phosphate concentration of 10 mg/L, nTiO₂ carried weak negative charge (Fig. 2-c), and an energy barrier (39.3 k_BT) existed between nTiO₂ and the sand (Fig. S4-b, SI). However, a relatively deep secondary minimum (-3.4 k_BT) was also present (Fig. S4-b inset, SI), which explains the relatively high attachment (percentage of particle attached = 13%). At the same pH and phosphate concentration, the secondary minimum in NaCl solutions was much weaker (-0.4 k_BT) (Fig. S4-a

inset, SI), and therefore did not affect particle retention. In CaCl₂ solution at pH 9, nTiO₂ attachment was high for all the phosphate concentrations tested (Fig. 5-b). The zeta potentials of nTiO₂ under these conditions were either positive or close to zero (Fig. 2-d), which resulted in attractive DLVO forces. The calculated DLVO interaction energy confirmed no energy barriers (Fig. S4-d, SI), indicating favorable conditions for nTiO₂ attachment.

In either NaCl or CaCl₂ solutions, illite attachment to sand at either pH was very low and not notably influenced by phosphate (Fig. 5-c & 5-d), because of the negative zeta potentials of nTiO₂ and negligible effect of phosphate on the zeta potential of illite (Fig. 2-e to 2-h). The calculated DLVO interaction energy profiles confirmed high energy barriers between the illite colloid and quartz sand under the various experimental conditions (Fig. S5, SI). Co-presence of Ca²⁺ and phosphate did not have a big effect on illite attachment to quartz sand. Illite, as a natural colloid, demonstrated a low affinity for phosphate in comparison to nTiO₂ particles, and therefore no considerable influence on illite attachment was observed in the co-presence of Ca²⁺ and phosphate.

2.4. Conclusions

Aggregation and attachment, which are among the most important mechanisms governing the fate and transport of fine particles in subsurface environment, have been investigated in this research under complex water chemistry conditions (i.e., co-presence of multiple interacting anions and cations at various pH). The results illustrated that nTiO₂ aggregation and attachment to quartz sand is strongly influenced by the interactions between phosphate and major cations, which depend on pH and valency of the major cation involved. The effect of pH on nTiO₂ attachment in NaCl background solutions was attributed to the changes in nTiO₂ zeta potential. Strong attractive forces at pH 5 (< pH_{pzc} ~ 6.8) between oppositely charged nTiO₂ and quartz sand led to notable

attachment, whereas at pH 9 ($> \text{pH}_{\text{pzc}} \sim 6.8$), negatively-charged nTiO_2 was repelled by sand surface. In CaCl_2 solution, nTiO_2 attachment to quartz sand was high at both pH due to the attractive interaction energy between oppositely charged particle and collector surface. The much higher attachment at pH 9 in comparison to that at pH 5 in CaCl_2 solution, which was inconsistent with the calculated particle-to-collector interaction energy, was attributable to ripening. Similar to nTiO_2 attachment to quartz sand, phosphate adsorption to nTiO_2 was also influenced by pH and valency of the major cation. At pH 5, phosphate adsorption to nTiO_2 was high due to attractive forces between positively-charged nTiO_2 and phosphate anions. However, at pH 9 phosphate adsorption was hindered since phosphate was repelled by negatively-charged nTiO_2 . In CaCl_2 background solution, notable phosphate adsorption was observed at pH 5 due to highly positive nTiO_2 zeta potential in the presence of Ca^{2+} . At pH 9, phosphate adsorption was even higher, presumably due to surface precipitation of Ca-P minerals. Phosphate attachment to illite was negligible because of strong repulsive forces between negatively charged illite colloids and phosphate anions. Furthermore, this study showed that phosphate decreased nTiO_2 attachment to the quartz sand due to phosphate adsorption to nTiO_2 , which changed the zeta potential of nTiO_2 from positive to negative, and therefore increased the energy barriers between nTiO_2 and the sand. At pH 9, however, nTiO_2 attachment was substantially higher in the presence of phosphate in CaCl_2 solution compared to that in NaCl solution. This can be attributed to the nearly zero zeta potential of nTiO_2 in CaCl_2 solution, causing high attraction between nTiO_2 and the sand, whereas in NaCl solution, highly negative zeta potential prevented nTiO_2 attachment to the sand. Illite showed a negligible affinity for quartz sand under all experiments conditions due to the strong repulsive forces between illite and the sand. This study showed that the attachment of illite colloid to quartz sand can be much less sensitive to the water chemistry changes compared to that of

nTiO₂. These findings are important for understanding the fate and transport of nTiO₂ and illite colloids in natural aquatic systems where various interacting anions and cations co-exist under low ionic strength conditions. Further research on the effect of varying ionic strength and mixed types of cations will be beneficial to understand the behaviour of these particles under a wider range of natural water chemistry conditions.

Acknowledgments

This work was supported by Natural Sciences and Engineering Research Council of Canada's Discovery Grant (No. 402815-2012) and Canada Foundation of Innovation's Leaders Opportunity Fund (No. 31836).

Appendix 1. Supplementary data

Supplementary material related to this chapter can be found, in the Appendices. All the original data are provided in electronic format.

Chapter 3. Nanoscale titanium dioxide (nTiO₂) aggregation and transport in the co-presence of dissolved phosphate, illite colloid, and Fe-oxyhydroxide coating

(Rastghalam, Z.S., Yan, C., Shang, J., Cheng, T., 2019. Nanoscale titanium dioxide (nTiO₂) aggregation and transport in the co-presence of dissolved phosphate, illite colloid, and Fe oxyhydroxide coating. *Colloids Surfaces A Physicochem. Eng. Asp.* 578, 123560)

Abstract

Many studies have been conducted to understand the fate and transport of nanoscale titanium dioxide (nTiO₂) in subsurface environments. However, most of these studies are under simplified conditions which do not represent the complex physicochemical conditions in the natural environment, where nTiO₂ simultaneously encounter various groundwater/aquifer components. To better understand the mechanisms that control the transport of this emerging contaminant in groundwater, column experiments were conducted under low ionic strength conditions at pH 5 and 9 to clarify the influence of co-present dissolved component, suspended natural particle, and medium geochemical heterogeneity on nTiO₂ transport through water-saturated porous media. Results showed that when using nTiO₂ as influent at pH 5, Fe oxyhydroxide coating increased the nTiO₂ mobility owing to the repulsive forces between positively charged nTiO₂ and the Fe oxyhydroxide coating. Conversely, illite inhibited nTiO₂ transport due to illite straining and nTiO₂ entrapment. Phosphate served as a bridge between nTiO₂ particles at pH 5, resulting in large aggregates and consequent straining, and therefore inhibited transport. At pH 9, the mobility of nTiO₂ was high in quartz sand columns, regardless of the presence of phosphate/illite colloids, due to the repulsive forces between negatively charged nTiO₂, phosphate, illite colloids, and quartz surface. However, Fe oxyhydroxide coating reduced nTiO₂ mobility, attributable to pH buffering, which resulted in attractive electrostatic forces

between the Fe oxyhydroxide coating and the negatively charged nTiO₂. Findings from this study showed that under complex physicochemical conditions nTiO₂ transport is controlled by the interactions between nTiO₂ and common groundwater/aquifer components, as well as the interactions between these components.

Keywords: Nanoscale titanium dioxide (nTiO₂); Phosphate; Illite colloid; Fe oxyhydroxide coating; DLVO theory

3.1. Introduction

With the rapid development and application of nanotechnology, many engineered nanoparticles, which are toxic and detrimental to ecosystems, have found their way into subsurface environments. Nanoscale titanium dioxide (nTiO₂) is one of the most commonly used nanomaterials and extensive research has been conducted to understand its fate and transport in subsurface environments (French et al., 2009; Laxman et al., 2016; Lv et al., 2016; Sharma, 2017; Toloni et al., 2014; Xu, 2018). To date, most studies on the aggregation and transport of engineered nanoparticles have focused on the influence of one or two environmental factor(s) (e.g., pH, ionic strength, cation or anion valence, clay colloids, natural organic matter, Fe oxyhydroxide coating on quartz sand), and have been performed in highly simplified matrices, such as homogeneous porous media (e.g., clean quartz sand or glass beads) and solutions with a single background electrolyte (e.g., NaCl). While these studies are necessary and valuable for the unambiguous identification of the mechanisms that govern nanoparticle behavior in the environment, they cannot represent the complexity and heterogeneity of natural environments.

When released into soil and groundwater, engineered nanoparticles will inevitably encounter multiple water-borne components as well as different minerals and organics in soil/sediments. Many of these aqueous and solid-phase components interact with engineered

nanoparticles and influence particle aggregation and transport (Chen et al., 2015; Domingos et al., 2009; Fisher-Power and Cheng, 2018; He et al., 2017; Tang and Cheng, 2018; Zhou and Cheng, 2018). Geo-genic cations and anions such as Na^+ , Ca^{2+} , Mg^{2+} , Al^{3+} , Cl^- , and SO_4^{2-} are ubiquitous in natural water. Other ions such as NO_3^- and PO_4^{3-} can also be found in natural water due to anthropogenic sources, e.g., excessive use of fertilizers. It is well established that cation valence and concentration affect particle aggregation and transport due to their influence on the electrical double layer (Loosli et al., 2015; Rastghalam et al., 2018; Tang and Cheng, 2018). It was also reported that anions such as phosphate could play a key role in the aggregation, mobilization, and transport of nTiO_2 due to phosphate adsorption to particle and medium surfaces, which changes surface charge and aggregation form (Chen et al., 2015; Guo et al., 2018; He et al., 2017; Rastghalam et al., 2018).

Besides dissolved ions, suspended clay colloids, which are abundant in many soil and groundwater, affect the behaviours of engineered nanoparticles. Cai et al. (2014) found increased nTiO_2 transport in the presence of bentonite colloids, whereas Zhou et al. (2012) reported destabilization and immobilization of nTiO_2 with the presence of montmorillonite particles. nTiO_2 adsorbs to clay colloids to form nTiO_2 -clay aggregates at $\text{pH} < \text{pH}_{\text{pzc}}$ of nTiO_2 due to electrostatic attraction, and retention of nTiO_2 by the transport medium under such conditions is governed by the nature of the interactions between nTiO_2 -clay aggregate and the medium (Tang and Cheng, 2018). Guo et al. (Guo et al., 2018) found enhanced nTiO_2 retention in quartz sand columns with the co-presence of montmorillonite or diatom particles as a result of larger size and less negative charged aggregates. They also showed that the co-present phosphate ion diminished the effect of the montmorillonite or diatom particles (Guo et al., 2018), attributable to phosphate adsorption to nTiO_2 , which increased the repulsive forces between particle and sand. Similar to phosphate,

humic acid was found to adsorb to nTiO₂ and reduce nTiO₂ retention caused by clay colloids (Tang and Cheng, 2018). Clay colloids and dissolved anionic species such as phosphate and humic acid often co-exist in natural water, therefore the simultaneous interactions between nanoparticle and dissolved species and between nanoparticle and clay colloid must be considered to predict how engineered nanoparticles would behave under such conditions.

When evaluating aggregation and transport of engineered nanoparticles in subsurface environments, another crucial consideration is mineralogical and organic composition of the transport media (Chen et al., 2012; Chowdhury et al., 2012; Domingos et al., 2009; Fang et al., 2009; Fisher-Power and Cheng, 2018; Loosli et al., 2015; Zhou and Cheng, 2018). Fe oxyhydroxide coating on sand grains, a common mineral component in soil and sediments, has received much attention due to its unique electrostatic property. Fe oxyhydroxides were reported to have a pH_{pzc} within the range of 8.1–8.5, and therefore carry positive charges in water with acidic or near neutral pH (Huang, 1995). As a result, Fe oxyhydroxide coatings have high affinity for negatively charged particles and are reported to increase the deposition of clay colloids. It was found that positively charged Fe oxyhydroxide is the dominant factor that controls the deposition of negatively charged particles (Cary et al., 2015; Han et al., 2014). In contrast, Fe oxyhydroxide coatings are shown to decrease the deposition of positively charged nTiO₂ due to electrostatic repulsion (Wu and Cheng, 2016).

In soil and groundwater, interactions among different natural components may also influence fine particle aggregation and mobility (Baalousha et al., 2013; Han et al., 2014; Loosli et al., 2015; Rastghalam et al., 2018; Tang and Cheng, 2018; Zhou and Cheng, 2018). For example, humic acid was found to reduce the retention of biochar nanoparticle and nTiO₂ in Fe oxyhydroxide-coated sand columns (Han et al., 2014; Wang et al., 2013). The reduction in particle

retention was attributable to adsorption of negatively charged humic acid to Fe oxyhydroxide coating, which reserved the positive charges on Fe oxyhydroxide and hence reduced the attractive forces between fine particles and the sand (Han et al., 2014; Wang et al., 2013). Montmorillonite and diatomite particles were shown to decrease nTiO₂ mobility due to hetero-aggregate formation, whereas the co-presence of phosphate with these particles increased the particle-particle and particle-sand repulsive forces and thereby enhanced nTiO₂ transport (Guo et al., 2018). Under natural conditions, interactions between multiple aqueous and solid-phase components are expected to be much more complicated than those in simplified laboratory systems, therefore the synergistic effect of multiple environmental components on particle aggregation and transport is not readily inferable from the individual effects. To understand the environmental fate of engineered nanoparticles, it is necessary to conduct experimental studies under complex physicochemical conditions similar to those found in the natural environment.

The objective of this research is to investigate nTiO₂ aggregation and transport under complex physicochemical conditions in order to better understand the behaviour of nTiO₂ in natural subsurface environments. nTiO₂ aggregation and transport were experimentally studied using batch and column experiments in the presence of one or more of the following components: dissolved phosphate, illite colloid, and Fe oxyhydroxide coating on quartz sand, all of which are commonly found in soil and groundwater. The co-presence of these components is used to mimic conditions in natural subsurface environments where nanoparticles could be simultaneously influenced by multiple processes from the dissolved species, suspended particles, and mineralogical heterogeneity of porous media. By comparing the hydrodynamic diameter (HDD), zeta potential, and breakthrough curves (BTCs) of the particles among different experiments, the influence of individual component as well as combined influence from multiple components were

identified. Derjaguin–Landau–Verwey–Overbeek (DLVO) theory was used to calculate the interaction energy, and a mathematical model was applied to simulate the BTCs. Based on the experimental results and theoretical analysis, geochemical processes that control nTiO₂ transport in the co-presence of multiple groundwater/aquifer components were proposed.

3.2. Materials and methods

3.2.1. Stock solutions and suspensions

All chemical reagents used in this study were of ACS analytical grade, and all experiments were conducted at room temperature (~22 °C). 100 mg/L phosphate stock solution was prepared by dissolving an appropriate quantity of NaH₂PO₄·H₂O powder in nano-pure water (resistivity >18.2 MΩ × cm, dissolved organic carbon < 0.02 mg/L). NaCl and NaOH solids were dissolved in nano-pure water to prepare the 0.1 M NaCl and 0.1 M NaOH solutions. Concentrated HCl solution (36.5 -38.0%) was diluted using nano-pure water to prepare the 0.1 M HCl solution. For accurate pH adjustment, 0.01 M NaOH and HCl solutions were prepared by dilution of the 0.1 M solutions.

Aeroxide[®] TiO₂ P25 powder (Fisher Scientific) with a reported purity of > 99.5%, an average particle size of 21 nm, and a specific surface area of 50 ± 15 m²/g was used to prepare nanoscale titanium dioxide (nTiO₂) suspensions. The X-ray diffraction (XRD) pattern indicated that Aeroxide[®] TiO₂ P25 consists of 90% anatase (particles size = 23 nm) and 10% rutile (particle size = 40 nm) (Wu and Cheng, 2016). nTiO₂ stock suspension (500 mg/L) was prepared by suspending the Aeroxide[®] TiO₂ powder in nano-pure water. The mixture was sonicated at 200 W for 30 minutes by a Branson Digital Sonifier (Crystal Electronics) to disperse the particles and achieve a homogeneous suspension.

To prepare the illite stock suspension, 4.0 g illite powder (IMt-2 Illite Cambrian shale, Clay Mineral Society) was suspended in 1000 mL nano-pure water. The mixture was stirred vigorously and subjected to a sonifier for 30 minutes at 200 W before being allowed to settle for 24 hours to remove larger particles. The supernatant was gently transferred to a high-density polyethylene (HDPE) bottle and used as the illite stock suspension. Illite concentration of the stock suspension was determined gravimetrically by filtering 100 mL of the suspension through a 0.1 μm pore-size polyethersulfone membrane filter. The filter was oven dried at 80 °C and weighed using an analytical balance before and after filtration to find out the mass of the illite colloids for calculating colloid concentration.

3.2.2. Transport media

Clean quartz sand and Fe oxyhydroxide-coated quartz sand were prepared and used as porous media. Quartz sand (U.S. Silica) with the size range of 0.6–0.7 mm was acid washed using the procedure of Wu and Cheng (Wu and Cheng, 2016) to ensure the sand surface was free of trace quantities of metal oxides and organics. The quartz sand was then rinsed, and oven dried at 120°C overnight before being stored until use.

The same type of quartz sand was used for the preparation of Fe oxyhydroxide coated-sand following the procedure described previously (Wu and Cheng, 2016). 200 g quartz sand was mixed with 20 g FeCl_3 and dissolved in 400 mL nano-pure water in a 1 L HDPE (high-density polyethylene) bottle. The initial pH of the mixture was adjusted to approximately 4.5 by adding aliquots of concentrated NaOH solution. To maximize the contact of sand grains with the solution, the mixture was shaken vigorously on a VWR orbital shaker at 300 rpm for 24 hours. The pH of the suspension was continuously monitored, and extra portions of NaOH were added to the bottle if needed to maintain the pH around 4.5–5.0. 20 bottles were set up to prepare an adequate quantity

of Fe oxyhydroxide-coated sand. After the shaking time had elapsed, the coated sand was thoroughly rinsed with nano-pure water and then soaked in a 0.01 M NaOH solution for 12 hours to make sure the loose iron precipitates were removed from the mixture. The sand was rinsed with deionized water multiple times until the color and pH of the flushing fluid did not change. Afterward, all the coated sand grains were mixed thoroughly and oven-dried at 120°C overnight before being stored and used in subsequent experiments.

Scanning electron microscopy (SEM) coupled with energy dispersive X-ray (EDX) was used to determine the fraction of the sand surface covered by Fe oxyhydroxide (Wang et al., 2012; Wu and Cheng, 2016). The amount of Fe oxyhydroxide coating on the sand was measured following the EPA Method 3050B, with modification (USEPA, 1996). One gram of the sand was digested by mixing the sand sample with 10 mL concentrated HNO₃, covering the container with a watch glass, and heating the mixture to 90 °C ± 5 °C for 15 minutes without boiling. The sample was allowed to cool for 5 minutes before another portion (5 mL) of concentrated HNO₃ was added and the sample was re-heated to 90 °C ± 5 °C for another 30 minutes. The mixture remained untouched to settle and cool for 15 minutes, and the supernatant was collected for ICP-MS analysis. The digestion procedure of the Fe oxyhydroxide-coated sand was performed in replicate, and a blank sample was carried out using the clean quartz sand.

3.2.3. Zeta potential and HDD measurement

Four types of nTiO₂ suspensions (i.e., nTiO₂ alone, nTiO₂-phospahte, nTiO₂-illite, and nTiO₂-phospahte-illite) were prepared by diluting the nTiO₂, illite, and phosphate suspensions/solutions at appropriate ratios. nTiO₂ concentration was 100 mg/L in each of the suspensions. The high nTiO₂ concentration used in this work is intended to facilitate sample analysis and help to identify various nTiO₂ aggregation and retention mechanisms. In the

suspensions with phosphate and/or illite, the concentrations of phosphate and illite colloids were 10 mg/L. Concentrations of suspended clay minerals such as illite colloids and phosphate in natural groundwater could span a wide range. Previous studies on stability and transport of clay colloids have been performed using various concentrations from a few mg/L (Syngouna and Chrysikopoulos, 2013) to hundreds of mg/L (Novich and Ring, 1984). The 10 mg/L phosphate in our study is close to the phosphate concentrations reported for some contaminated groundwater (Singh et al., 2012). In the nTiO₂-phosphate-illite suspension, illite and phosphate were mixed before nTiO₂ addition. An illite alone suspension with illite colloid concentration of 100 mg/L was also prepared. For all the suspensions, NaCl stock solution was added to adjust the ionic strength to 1 mM, and the pH was adjusted with 0.1/0.01 M HCl or 0.1/0.01 M NaOH to obtain a final pH of 5 or 9.

The quartz sand was powdered using a laboratory pulverizer (TE250, Angstrom) and mixed with 2000 mL nano-pure water in a container. The mixture was first vigorously stirred for 5 minutes and then sonicated for 30 minutes with 200 W power. The container was left untouched overnight to allow the large particles to settle, and the supernatant was gently transferred into another container and stored. The quartz particle stock suspension was diluted, and the ionic strength and pH of the samples were adjusted before being used for zeta potential measurement.

A zetasizer Nano-ZS (Malvern) was utilized to measure the zeta potential and HDD of the suspensions. Laser Doppler velocimetry coupled with phase analysis light scattering was used to determine particle electrophoretic mobility, which was then converted to zeta potential using the Smoluchowski equation. The HDD was measured based on dynamic light scattering (DLS). All the zeta potential and HDD measurements were performed in duplicate and within one hour after the samples were prepared.

3.2.4. Column experiments

A cylindrical Kontes Chromaflex chromatography column (15 cm long and 2.5 cm inner diameter, made of borosilicate glass) was used for the column experiments. The column was set up vertically and packed by adding small amounts of sand (described in Section 3.2.2) in ~ 1 cm increment to the column with a small volume of 1 mM NaCl background solution. The column was tapped during packing to minimize layering or entrapment of air bubbles. A Masterflex peristaltic pump (Cole-Parmer) was used to supply more background solution to the column during packing. When fully packed, the column was tightened with high-density polyethylene bed support (pore size = 20 μm) on both ends. The mass of the sand and background solution used to saturate the column was recorded to determine the bulk density, porosity, and pore volume for each column.

The packed column was pre-equilibrated with a 1 mM NaCl background solution at the desired pH (5 or 9) overnight at a flow rate of 1 mL/min (average water velocity = 0.51 cm/min) using the Masterflex peristaltic pump. Following pre-equilibration, nTiO_2 suspensions (described in Section 3.2.3) were pumped upward into the columns at the same flow rate. Sixteen column experiments were performed, and the column experiments were distinguishable based on the type of the porous media (clean quartz sand vs. Fe oxyhydroxide-coated sand), influent composition (nTiO_2 alone, nTiO_2 -phospahte, nTiO_2 -illite, and nTiO_2 -phospahte-illite), and pH (5 or 9) (Table S2, SI). All the column experiments were performed in duplicate at room temperature (~ 22 $^\circ\text{C}$). During each experiment, the influent suspension was stirred periodically to avoid gravity settling. The pH of the suspensions was monitored and maintained within the range of 5.0 ± 0.05 or 9.0 ± 0.2 by adding small amounts of 0.1/0.01 M NaOH and/or 0.1/0.01 M HCl solutions. The influent container was covered with parafilm to minimize the suspension's contact with air. Meanwhile, the effluent samples were collected by a fraction collector (Spectrum Laboratories CF-2). Upon

completion of nTiO₂ injection, the influent suspension was switched back to the background solution, and injection of the background solution was ended when light absorbance of the effluent approached zero.

Light absorbance of the nTiO₂ in the effluent was measured by a Thermo Scientific GENESYS 10S UV-vis spectrophotometer at a wavelength of 368 nm for experiments with no illite colloid in the influent, but at 600 nm for experiments with illite colloid in the influent to eliminate the interference from illite particles (Cai et al., 2014; Tang and Cheng, 2018). Based on the calibration curves, light absorbance of the effluent was converted to nTiO₂ concentration, and breakthrough curves (BTCs) were obtained by plotting the relative effluent concentration (C/C_0) (C and C_0 are effluent and influent nTiO₂ concentration respectively) as a function of pore volumes (PV) passing through the columns. Effluent pH was recorded during the injection to detect any changes in pH.

3.2.5. Theoretical considerations

3.2.5.1. DLVO calculations

Following the classic Derjaguin-Landau-Verwey-Overbeek (DLVO) theory (Derjaguin and Landau, 1941; Verwey and Overbeek, 1948), particle-to-particle and particle-to-collector interaction energy profiles were calculated with the assumption of sphere-sphere and sphere-plate geometry respectively. Details on the interaction energy calculation were described in the SI.

3.2.5.2. Modeling nTiO₂ transport

The transport and deposition of nTiO₂ in the quartz sand and Fe oxyhydroxide-coated sand columns were simulated using a one-site or two-site kinetic model that is incorporated in HYDRUS-1D as described in the SI.

3.3. Results and discussions

3.3.1. Zeta potential and HDD of the influent suspensions

pH 5. High zeta potential (+30.4 mV) and small HDD (211 nm) was shown for the nTiO₂ suspension with no phosphate or illite (Fig. 6-a & 6-c). According to the DLVO calculations, the small HDD was attributable to the energy barrier (46.7 k_BT) between positively charged nTiO₂ particles (Table 1).

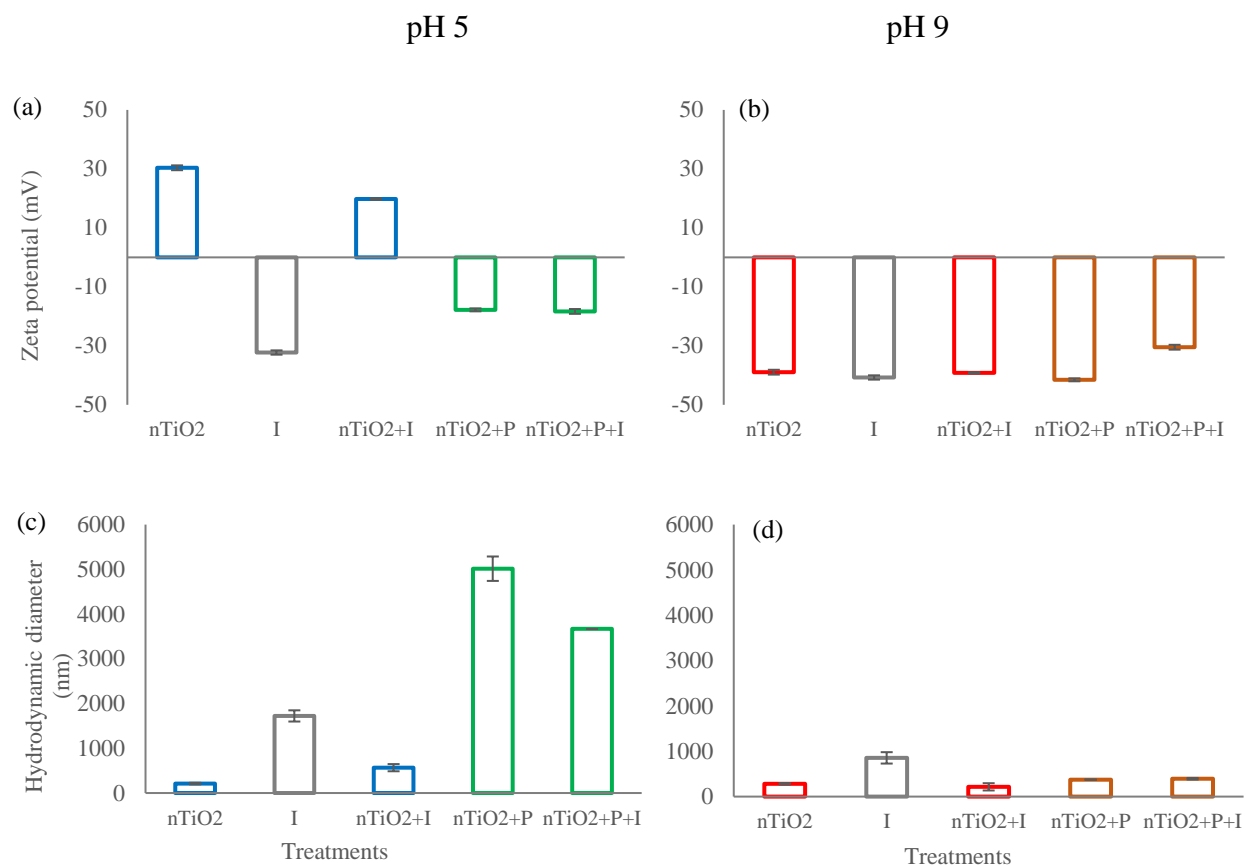


Fig. 6. Zeta potential (a & b) and HDD (c and d) of various suspensions. Background solution was 1 mM NaCl, nTiO₂ = 100 mg/L, illite colloid (I) = 10 mg/L (for the illite only treatment 100 mg/L illite was used), and phosphate (P) = 10 mg/L. Data is expressed as mean \pm standard deviation of duplicate measurement. (For interpretation of the colors used in this figure, the reader is referred to the colored version of this article).

Table 1 . DLVO calculation results for particle-particle interactions.

pH	Suspension	Particle-particle	Hamaker constant ($\times 10^{-20}$ J)	nTiO ₂	nTiO ₂	Φ_{\max} (k _B T)	$\Phi_{2\min}$ (k _B T) ^a
				zeta potential (mV)	HDD (nm)		
5	nTiO ₂	nTiO ₂ -nTiO ₂	3.5	30.4±0.5	211±80	46.7	
	Illite	Illite-illite	2.2	-32.3±0.2	1723±125	443.5	
	nTiO ₂ -illite	ND ^b	ND ^b	19.8±0.3	567±109	ND ^b	ND ^b
	nTiO ₂ -phosphate	nTiO ₂ -nTiO ₂	3.5	-17.8±0.7	5014±273	214.9	-1.7
	illite-phosphate	Illite-illite ^c	2.2	-30.8±1.0	936±59	192.4	
	nTiO ₂ -phosphate-illite	nTiO ₂ -illite ^d	2.0	-18.3±0.4	3670±64	137.5	-2.0
	nTiO ₂	nTiO ₂ -nTiO ₂	3.5	-38.9±1	282±51	112.9	
9	Illite	Illite-illite ^d	2.2	-40.7±0.5	854±81	381.1	
	nTiO ₂ -illite	nTiO ₂ -illite ^d	2.0	-39.2±0.2	215±80	295.2	-1.7
	nTiO ₂ -phosphate	nTiO ₂ -nTiO ₂	3.5	-41.5±0.9	373±11	161.0	
	illite-phosphate	Illite-illite ^c	2.2	-37.2±0.9	810±29	267.6	
	nTiO ₂ -phosphate-illite	nTiO ₂ -illite ^d	2.0	-30.5±0.5	394±6	239.8	-0.3

^a Blanks indicate secondary energy minimum ($\Phi_{2\min}$) did not exist. ^b ND: not determined. Zeta potential and HDD measurements in this mixed suspension reflected the mean properties of 3 dissimilar particles (nTiO₂, illite colloid, and nTiO₂-illite aggregate) and, therefore, the zeta potential or HDD for each of the individual particle cannot be determined. As a result, DLVO calculations were not performed. ^c In the presence of 10 mg/L phosphate, the zeta potential and HDD of the illite suspensions were measured by Rastghalam et al. (2018). ^d For the mixed particle (i.e., nTiO₂-illite) suspensions, the zeta potential and HDD in the individual suspensions (i.e., nTiO₂ suspension and illite suspension respectively) were used for the DLVO calculations.

Zeta potential of the nTiO₂-illite suspension was +19.8 mV, less positive than that of the nTiO₂ alone suspension (+30.4 mV) (Fig. 6-a). The lower zeta potential of the nTiO₂-illite suspension was due to the negatively charged illite colloids, which reduced mean zeta potential of the suspension. At pH 5, illite colloid and nTiO₂ were oppositely charged, indicating formation of hetero-aggregates with large HDD (Tang and Cheng, 2018). The HDD of the nTiO₂-illite suspension, measured within one hour after preparing the mixture, was 567 nm. This HDD was

between those of nTiO₂ and illite colloid in the nTiO₂ alone and illite alone suspensions (211 and 1723 nm respectively) (Fig. 6-c). This relatively small HDD of the nTiO₂-illite suspension (567 nm) was attributable to the low concentration ratio of illite to nTiO₂ in the experiment (1:10). Due to the low concentration ratio of illite to nTiO₂, only a small fraction of the nTiO₂ were consumed in the nTiO₂-illite formation, and therefore most of the particles in the suspension were nTiO₂ particles. Additionally, formation of the nTiO₂-illite hetero-aggregates is a slow process (Tang and Cheng, 2018), therefore the aggregation was still at its early stage and large aggregates had not yet formed by the time when we made the measurement (i.e., < 1 hour after preparation). With 10 mg/L phosphate added, zeta potential of the nTiO₂ suspension was reversed from positive (+30.4 mV) to negative (-17.8 mV) (Fig. 6-a). The reduction in zeta potential was due to adsorption of negatively charged phosphate ions to the positive nTiO₂ surface. Previous studies showed that the zeta potential of nTiO₂ at pH < pH_{pzc} changed from positive to negative due to phosphate addition (He et al., 2017; Rastghalam et al., 2018). As shown in Fig. 6-c, the HDD of the nTiO₂-phosphate suspension was much larger than that of the nTiO₂ alone suspension (5014 vs. 211 nm). The large HDD in the presence of phosphate was not explainable by the DLVO calculation, which indicated a high energy barrier (214.9 k_BT, Table 1). A secondary minimum of -1.7 k_BT, which was comparable to the mean kinetic energy of nanoparticles (~1.5 k_BT) reported by Treumann et al. (2014), was also present. This suggested that the nTiO₂ could be trapped by secondary minimum, contributing to the formation of the large nTiO₂ aggregates. Nevertheless, secondary minimum did not result in such large HDD under similar conditions (Tang and Cheng, 2018). Connor and McQuillan (1999) demonstrated that phosphate has the potential to bind to TiO₂ particles as a bidentate surface species and may serve as a bridge between particles. Hence, we hypothesized that phosphate bridging is the main mechanism for nTiO₂ homo-aggregation (i.e.,

aggregate formation by one type of particle) in the nTiO₂-phosphate suspension, similar to that in a previous study (Rastghalam et al., 2018).

In the co-presence of nTiO₂, phosphate, and illite colloids, the zeta potential of the suspension was negative (-18.3 mV) (Fig. 6-a), and the HDD was large (3670 nm) (Fig. 6-c), indicating particle aggregation. In this system, phosphate adsorption to positively charged nTiO₂, and formation of nTiO₂-illite aggregates (due to electrostatic attraction) could occur concurrently. While nTiO₂-illite aggregate formation was a relatively slow process (Tang and Cheng, 2018), phosphate adsorption to nTiO₂ was much faster (Fig. S8, SI), which made the zeta potential of nTiO₂ negative and prevented nTiO₂-illite aggregate formation. Therefore, the high HDD of the nTiO₂-phosphate-illite suspension was due to the formation of large nTiO₂ aggregates via phosphate bridging, as discussed for the nTiO₂-phosphate suspension. In contrast, very few nTiO₂-illite hetero aggregates were expected to form. The HDD of the nTiO₂-phosphate-illite suspension was smaller than that of the nTiO₂-phosphate suspension (3670 vs. 5014 nm, Fig. 6-c). This was due to the presence of illite colloids (HDD = 1723 nm), which reduced the suspension's mean HDD.

pH 9. At pH 9, the nTiO₂ was negatively charged (-38.9 mV) and the HDD was small (282 nm) (Fig. 6-b & 6-d), consistent with the energy barrier between nTiO₂ particles (112.9 k_BT) predicted by the DLVO theory (Table 1). The zeta potential and HDD of the illite colloid alone suspension were -40.7 mV and 854 nm, respectively (Fig. 6-b & 6-d), and the energy barrier (381.1 k_BT) between the illite colloids was high (Table 1).

At pH 9, both nTiO₂ and illite colloids carried negative charges (Fig. 6-b). As a result, mixing the two did not produce large changes in the zeta potential and HDD of the suspension (zeta potential = -38.9 mV and HDD = 282 nm for the nTiO₂ suspension vs. zeta potential = -39.2

mV and HDD = 215 nm for the nTiO₂–illite suspension). A high energy barrier (295.2 k_BT) between illite colloid and nTiO₂ was indicated by the DLVO calculation (Table 1), similar to the results of Zhou et al. (Zhou et al., 2012), who showed a high energy barrier between negatively charged nTiO₂ and montmorillonite at pH 8.

The zeta potential and HDD of the nTiO₂–phosphate suspension was similar to those of the nTiO₂ alone suspension at pH 9 (Fig. 6-b & 6-d). Phosphate did not affect the zeta potential and HDD of nTiO₂ at pH 9 due to very low phosphate adsorption to nTiO₂ (Rastghalam et al., 2018). In a mixture containing all the three components (nTiO₂, illite colloid, and phosphate), the suspension's zeta potential was negative (-30.5 mV) and the HDD was small (394 nm) (Fig. 6-b & 6-d). This is qualitatively consistent with the calculated high energy barriers between nTiO₂ and illite colloid (Table 1), which prevented aggregate formation. Guo et al. (2018) reported small HDDs for nTiO₂ and clay colloid mixtures in the presence of phosphate as a result of the strong electrostatic repulsions between negatively charged nTiO₂ and clay particles.

3.3.2. nTiO₂ transport

3.3.2.1. nTiO₂ suspension at pH 5 (blue diamonds (◇) in Fig. 7-a & 7-b)

Quartz sand column. For the quartz sand column using the pH 5 nTiO₂ suspension as influent, nTiO₂ were first detected in the effluent at PV = ~4.5 (Fig 2-a). Hereafter, the C/C₀ increased notably and then leveled off at 0.86. At pH 5, nTiO₂ was positively charged (Fig. 6-a), whereas quartz sand's zeta potential was negative (-32.3 mV) (Rastghalam et al., 2018), indicating favorable deposition conditions (Table 2).

Quartz sand

Fe-coated sand

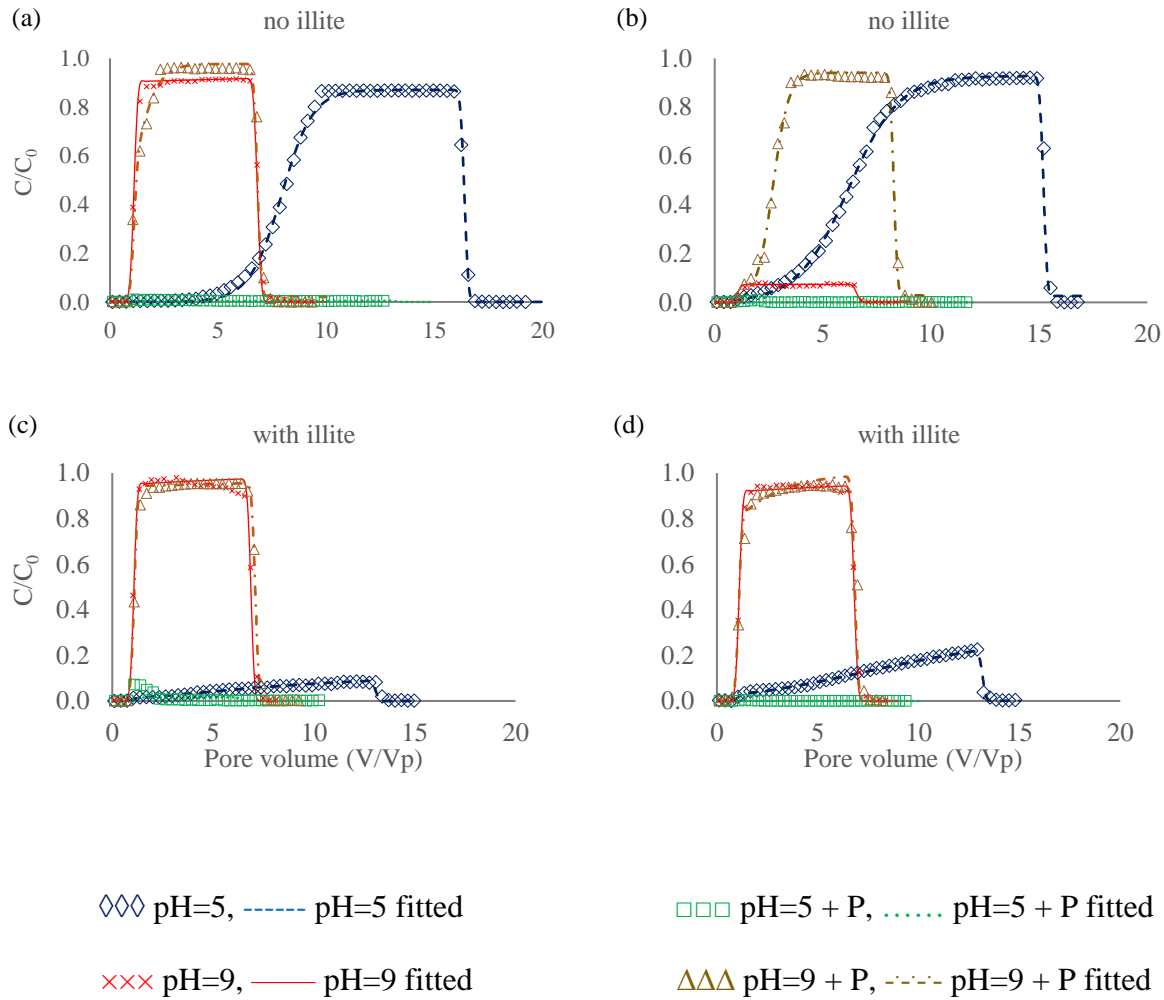


Fig. 7. Measured (symbols) and fitted (lines) BTCs of $n\text{TiO}_2$ for experiments conducted in quartz sand (a & c) and Fe oxyhydroxide-coated sand (b & d) columns. Background solution = 1 mM NaCl. Flowrate= 1 mL/min. $n\text{TiO}_2$ = 100 mg/L. Illite colloid = 10 mg/L. Phosphate (P) = 10 mg/L. C_0 and C represent influent and effluent particle concentration, respectively. (For interpretation of the colors used in this figure, the reader is referred to the colored version of this article).

Table 2. DLVO calculation results for particle-collector interactions.

pH	Suspension	Particle	Collector	Hamaker constant ($\times 10^{-20}$ J)	nTiO ₂ zeta potential (mV)	nTiO ₂ HDD (nm)	Illite zeta potential (mV)	Illite HDD (nm)	Collector zeta potential (mV) ^{a, b}	Φ_{\max} (k _B T) ^c	$\Phi_{2\min}$ (k _B T)	
5	nTiO ₂	nTiO ₂	Quartz sand	1.4	30.4±0.5	211±80	-	-	-32.0±8.0	90.1		
			Fe coating	12.6					40.3±6.0			
	Illite	Illite	Quartz sand	0.6	-	-	-32.3±0.2	1723±125	-32.0±8.0	106.3		
			Fe coating	6.4					40.3±6.0			
	nTiO ₂ -illite	nTiO ₂ -illite	Quartz sand	-	-	-	-	-	-	ND ^d	ND ^d	
			Fe coating	-					-			
	nTiO ₂ -phosphate	nTiO ₂	Quartz sand	1.4	-17.8±0.7	5014±273	-	-	-32.0±8.0	152.7	-1.0	
			Fe coating	12.6					40.3±6.0			
	nTiO ₂ -phosphate-illite ^e	nTiO ₂	Quartz sand	1.4	-17.8±0.7	5014±273	-	-	-32.0±8.0	152.7	-1.0	
			Fe coating	12.6					40.3±6.0			
	9	nTiO ₂	nTiO ₂	Quartz sand	1.4	-38.9±1.0	282±51	-	-	-43.0±1.0	27.9	
				Fe coating	12.6					-15.9±13.9	35.7	
Illite		Illite	Quartz sand	0.6	-	-	-40.7±0.5	854±81	-43.0±1.0	90.4		
			Fe coating	6.4					-15.9±13.9	151.9		
nTiO ₂ -illite ^f		nTiO ₂	Quartz sand	1.4	-38.9±1.0	282±51	-	-	-43.0±1.0	27.9		
			Fe coating	12.6					-15.9±13.9	35.7		
nTiO ₂ -phosphate	nTiO ₂	Quartz sand	1.4	-41.5±0.9	373±11	-	-	-43.0±1.0	51.8			
		Fe coating	12.6					-15.9±13.9	33.1			
nTiO ₂ -phosphate-illite ^g	nTiO ₂	Quartz sand	1.4	-41.5±0.9	373±11	-	-	-43.0±1.0	51.8			
		Fe coating	12.6					-15.9±13.9	33.1			

^a Our primarily experiments showed that phosphate did not affect the zeta potential of the quartz sand due to the negligible phosphate adsorption to the quartz sand. Hence, the zeta potential of quartz sand measured in the phosphate-free samples was used for the DLVO calculations. ^b Fe oxyhydroxide zeta potential measurements were performed by Wu and Cheng (2016). ^c Blanks indicate energy barrier (Φ_{\max}) or secondary energy minimum ($\Phi_{2\min}$) did not exist. ^d ND: not determined, due to unknown nTiO₂ or illite colloid zeta potential and HDD. ^e The zeta potential

and HDD of the nTiO₂-phosphate suspension at pH 5 were used for the DLVO calculations.^f The zeta potential and HDD of the nTiO₂ suspension at pH 9 were used for the DLVO calculations.^g The zeta potential and HDD of the nTiO₂-phosphate suspension at pH 9 were used for the DLVO calculations.

The nTiO₂ elution from the column showed that the favorable deposition sites had become saturated, preventing incoming particles from deposition (i.e., blocking effect). Saturation of favorable deposition sites was previously reported. Chowdhury et al. (Chowdhury et al., 2011) showed that with increasing nTiO₂ concentration in the influent from 100 mg/L to 800 mg/L at pH 5, nTiO₂ elution from the column increased from $C/C_0 = 0.04$ to 0.91 despite favorable deposition conditions, attributable to site saturation. Wu and Cheng (2016) measured a deposition capacity of 0.29 mg nTiO₂ per gram quartz sand at pH 5 in 1 mM NaCl using batch methods.

Fe oxyhydroxide-coated sand column. At pH 5, for the Fe oxyhydroxide-coated sand column, earlier breakthrough of nTiO₂ compared to that of the quartz sand column (1 PV vs. 4.5 PV) was observed. SEM results demonstrated that $14 \pm 3\%$ of the Fe oxyhydroxide-coated sand surface was covered with Fe oxyhydroxide, while the remaining surface was uncoated quartz (Fig. S6, SI). The concentration of Fe oxyhydroxide coating was determined to be 107 ± 15 mg Fe per kg sand by ICP-MS. At pH 5, the zeta potential of nTiO₂ and Fe oxyhydroxide coating in 1 mM NaCl were both positive (Wang et al., 2015; Wu and Cheng, 2016), while the zeta potential of quartz was negative (Rastghalam et al., 2018). Therefore, in the Fe oxyhydroxide-coated sand column, interactions of nTiO₂ with two distinct surfaces (i.e., quartz and Fe oxyhydroxide) need to be considered (Fig. 7-b). Although attractive electrostatic forces existed between nTiO₂ and quartz surface, patchy Fe oxyhydroxide coating on the sand surface decreased the favorable deposition site density due to the repulsive electrostatic forces between nTiO₂ and Fe

oxyhydroxide coating (with an energy barrier of 90.1 k_BT) (Table 2), resulting in earlier breakthrough. The blocking shape (i.e., a gradual increase followed by a plateau at high effluent concentration) of nTiO₂ BTC indicated a decrease in nTiO₂ deposition. This is most likely caused by those previously deposited particles, which repelled other particles attempting to attach to the quartz sand surface (Elimelech et al., 2013).

3.3.2.2. nTiO₂-illite suspension at pH 5 (blue diamonds (◇) in Fig. 7-c & 7-d)

Quartz sand column. With the nTiO₂-illite suspension used as influent, effluent nTiO₂ concentration was considerably lower ($C/C_0 = 0.08$) compared to that with the nTiO₂ suspension used as influent ($C/C_0 = 0.86$) (Fig. 7-c vs. 7-a). Additionally, effluent nTiO₂ concentration increased slowly and linearly during the injection of the nTiO₂-illite suspension without reaching a steady state concentration. Previous studies showed that suspended clay colloids could either enhance, hinder, or do not influence the transport of nTiO₂ (Bayat et al., 2015; Cai et al., 2014; Guo et al., 2018). Cai et al. (Cai et al., 2014) found increased nTiO₂ transport in the co-presence of bentonite particle, where bentonite acted as a carrier for nTiO₂ transport. In contrast, Guo et al. (2018) observed lower nTiO₂ transport in the co-presence of suspended montmorillonite or diatomite colloids. Bayat et al. (Bayat et al., 2015) showed that clay colloids trapped at the pore throats of the porous media, which enhanced straining and hindered nTiO₂ transport. Additionally, they observed that trapped illite colloids, due to their fibrous structure, provided sites for nTiO₂ retention (Bayat et al., 2015). In our experiments, the illite colloids were negatively charged and repelled by the like-charged quartz sand. However, the illite particles were large in size, and the particle-to-collector grain diameter ratio (d_p/d_c), $= 2.7 \times 10^{-3}$, was greater than the reported value of 2×10^{-3} at which straining occurs (Auset and Keller, 2006; Chowdhury et al., 2011; Xu et al., 2006). As a result, the illite colloids could be strained in the sand column, and the strained colloids, in

turn, provided sites for nTiO₂ immobilization, considering the electrostatic attraction between nTiO₂ and illite colloid, and the fibrous structure of the illite. Another result of the electrostatic attraction between nTiO₂ and illite colloid was the formation of nTiO₂-illite hetero-aggregates during the course of the experiment. Tang and Cheng (2018) reported continuous formation of nTiO₂-illite aggregates over a 6 hour period in nTiO₂-illite suspensions under similar conditions used in our experiments (i.e., 1 mM NaCl background solution at pH 5). The nTiO₂-illite hetero-aggregates had a larger size but less negative electrical charge than those of the pure illite colloid, therefore, straining of the nTiO₂-illite hetero-aggregates was under more favourable conditions in comparison to the pure illite colloids. Moreover, surface charge heterogeneity of the nTiO₂-illite aggregates could also facilitate retention when the positively charged portion of the particle surface was attracted to the quartz surface.

Fe oxyhydroxide-coated sand column. With the nTiO₂-illite suspension used as influent, shape of the breakthrough curve was similar for the Fe oxyhydroxide-coated sand column and the quartz sand column (i.e., both showed linear increase in nTiO₂ concentration) (Fig. 7-c & 7-d). In the Fe oxyhydroxide-coated sand column, transport of nTiO₂ was also inhibited by the co-present illite colloids. Effluent nTiO₂ concentration was less than 0.22 when nTiO₂-illite was used as the influent, compared to that of 0.92 when nTiO₂ was used as influent (Fig. 7-d vs. 7-b). Similar to that discussed for the quartz sand column, the lower transport was due to straining of the large illite colloids and nTiO₂-illite aggregates, which served to immobilize nTiO₂ via straining and electrostatic attraction. With the nTiO₂-illite suspension used as influent, nTiO₂ transport was higher in the Fe oxyhydroxide-coated sand column compared to that in the quartz sand column, as indicated by the larger slope of the linear BTC. The higher transport was the result of the Fe oxyhydroxide-coating, which carried positive charge and repelled the like-charged nTiO₂.

3.3.2.3. nTiO₂–phosphate suspension at pH 5 (green squares (□) in Fig. 7-a & 7-b)

Quartz sand and Fe oxyhydroxide-coated sand columns. At pH 5, phosphate considerably restrained nTiO₂ transport, i.e., the effluent nTiO₂ concentration was close to zero during injection (~12.7 PV) (Fig. 7-a). Zeta potential measurements showed that zeta potential of the nTiO₂–phosphate suspension was negative (Fig. 6-a), and the DLVO calculations confirmed a high energy barrier between nTiO₂ and quartz sand (152.7 k_BT) (Table 2), suggesting low attachment and high transport, which contradicted the experimental results. As previously mentioned, phosphate bridging between nTiO₂ led to the fast formation of large nTiO₂ aggregates (5014 nm). The low nTiO₂ mobility in this experiment was attributed to straining. Based on nTiO₂ HDD ($d_p = 5014$ nm) (Fig. 7-b) and the sand grain size ($d_c = 0.6-0.7$ mm), in our experiment with the nTiO₂–phosphate suspension as influent, particle to collector grain diameter ratio (d_p/d_c) was $\sim 7.5 \times 10^{-3}$, greater than the reported value of 2×10^{-3} at which straining occurs (Auset and Keller, 2006; Chowdhury et al., 2011; Xu et al., 2006). We visually observed large particle aggregates trapped near the column inlet when the nTiO₂–phosphate suspension was used as influent, suggesting retention via physical straining and/or gravity sedimentation, as opposed to electrostatic attraction (Yan et al., 2019). The straining was much more effective in the nTiO₂–phosphate experiment compared to that in the nTiO₂–illite experiment due to the fast formation of the aggregates in the presence of phosphate.

Similar to that for the quartz sand column, when nTiO₂–phosphate suspension was injected, nTiO₂ did not pass through the Fe oxyhydroxide-coated sand column ($C/C_0 = 0$ after ~10.3 PV) (Fig. 7-b) as a result of straining of the large nTiO₂ aggregates.

3.3.2.4. nTiO₂–phosphate–illite suspension at pH 5 (green squares (□) in Fig. 7-c & 7-d)

Quartz sand and Fe oxyhydroxide-coated sand columns. At pH 5 using the nTiO₂–phosphate–illite suspension as influent, effluent nTiO₂ concentration was practically zero for the quartz sand column (Fig. 7-c). Zeta potential measurement showed that all the particles were negatively charged in the suspensions containing phosphate (Fig. 6-a), and DLVO calculations confirmed that high energy barrier between nTiO₂ and the quartz sand (Table 2), indicating high nTiO₂ mobility. The low nTiO₂ mobility was mainly caused by straining of the large nTiO₂ aggregates ($HDD > 3670$ nm, $d_p/d_c > 5.5 \times 10^{-3}$). In addition, the were nTiO₂ also repelled by the illite colloids, therefore, the presence of illite did not show a substantial effect on nTiO₂ transport under this condition.

Using the nTiO₂–phosphate–illite suspension as influent, effluent nTiO₂ concertation was also close to zero for the Fe oxyhydroxide-coated sand column (Fig. 7-d), as a result of straining of the large nTiO₂ aggregates.

3.3.2.5. nTiO₂ suspension at pH 9 (red times (×) in Fig. 7-a & 7-b)

Quartz sand column. A pH 9 using the nTiO₂ suspension as influent, effluent nTiO₂ concentration increased quickly and reached a plateau of $C/C_0 \sim 0.91$ at $= 1$ PV (Fig. 7-a). At pH 9, nTiO₂ were negatively charged and repelled by the quartz sand. DLVO calculations showed a high energy barrier between nTiO₂ and the quartz sand (Table 2), indicating low retention and high mobility.

Fe oxyhydroxide-coated sand column. With the nTiO₂ suspension as influent, effluent nTiO₂ concentration was substantially lower for the Fe oxyhydroxide-coated sand column compared to that for the quartz sand column ($C/C_0 < 0.07$ vs. $C/C_0 = 0.91$) (Fig. 7-b vs. 7-a). However, DLVO calculations predicted an energy barrier of 27.9 k_BT between nTiO₂ and quartz, and 35.7 k_BT

between nTiO₂ and Fe oxyhydroxide coating, indicating high mobility. Additionally, the HDD of nTiO₂ was small at pH 9 (Fig. 7-d), and therefore straining was not expected. The low nTiO₂ mobility in this experiment was presumably related to changing pH along the column. Although pH of the influent was 9, due to pH buffering of the Fe oxyhydroxide coating, the effluent pH was reduced to 8.2 (Fig S2-d, SI), which was close to the p*H*_{pzc} ~8.4 for Fe oxyhydroxide (Wang et al., 2012; Wu and Cheng, 2016). As a result, the Fe oxyhydroxide near the effluent side of the column could be electrostatic neutral or carry weak positive charges while the nTiO₂ and quartz remained negatively charged. Previous studies illustrated that in chemically heterogeneous porous media, colloids deposition is controlled by the fraction of the porous media having the most favorable deposition sites (Elimelech et al., 2000; Han et al., 2014). Therefore, in our experiment, it is likely that the fraction of porous media covered by the Fe oxyhydroxide provided favorable sites for nTiO₂ deposition. Changes in pH along flow path, which consequently changed the zeta potential of particle and the medium surfaces, were previously reported (Fisher-Power and Cheng, 2018). In all the column experiments reported in this paper, the effluent pH was different from that of the influent (Fig. S7, SI). However, the change in pH became crucial only in the Fe oxyhydroxide-coated sand columns when the pH changed from 9 to a pH lower than the p*H*_{pzc} of Fe oxyhydroxide (~8.4), since the surface charge of Fe oxyhydroxide reversed under this condition. Moreover, surface roughness of the Fe oxyhydroxide coating could also have contributed to the higher nTiO₂ retention in the Fe oxyhydroxide coated sand column compared to that in the quartz sand column (Fig. 7-b vs. 7-a). Roughness has been shown to considerably reduce or even eliminate energy barrier, leading to favorable deposition conditions (Bradford et al., 2017; Hwang et al., 2018; Wu and Cheng, 2016; Zhou and Cheng, 2018).

3.3.2.6. nTiO₂-illite suspension at pH 9 (red times (×) in Fig. 7-c & 7-d)

Quartz sand column. For the quartz sand column, when the nTiO₂-illite suspension was used as influent, the BTC was similar to that when the nTiO₂ suspension was used as influent (Fig. 7-c vs. 7-a). At pH 9, quartz sand, nTiO₂, and illite colloids were all negatively charged. Hence, nTiO₂ and illite colloids were present as individual particles and repelled by the quartz sand. DLVO calculations confirmed high particle-to-particle and particle-to-quartz sand energy barriers (Table 1 & 2). Size of the illite colloids was much smaller than that at pH 5 (854 vs. 1723 nm). As a result, straining was unlikely at pH 9 (i.e., $d_p/d_c = 1.3 \times 10^{-3}$, smaller than the cut-off value of 2×10^{-3}).

Fe oxyhydroxide-coated sand column. Interestingly, nTiO₂ mobility was high in the Fe oxyhydroxide-coated sand column and hit a plateau of $C/C_0 = 0.95$ at ~1 PV when illite colloids were present in the influent (Fig. 7-d). Both nTiO₂ and illite colloids were negatively charged in this experiment and therefore, repelled each other and were repelled by the quartz sand (Table 2). The effluent pH (~8.1) (Fig. S7-d, SI), however, was below the pH_{pzc} of Fe oxyhydroxide, indicating that the Fe oxyhydroxide coating could carry positive charges and attract nTiO₂ and illite colloids. The much higher nTiO₂ transport in this experiment compared to that in the absence of illite (Fig. 7-d vs. 7-b) was presumably the result of illite competition for deposition sites on the Fe oxyhydroxide coating, which reduced nTiO₂ deposition and enhanced its transport. Previous column tests demonstrated that the competition from nutrients (Han et al., 2013), perfluorooctanoic acid (PFOA) (Wu et al., 2016), or bacteria (Han et al., 2016) for deposition sites could be a major contributor to enhanced fine particle transport. Cai et al. (Cai et al., 2013) also found that the co-presence of nC60 nanoparticles in the influent suspensions increased nTiO₂ mobility in sand columns due to nC60 competition for deposition sites.

3.3.2.7. nTiO₂-phosphate suspension at pH 9 (brown triangle (Δ) in Fig. 7-a & 7-b)

Quartz sand column. At pH 9 with the nTiO₂-phosphate suspension as influent, effluent nTiO₂ concentration plateaued at $C/C_0 = \sim 0.96$ after ~ 1 PV for the quartz sand column (Fig. 7-a). The high nTiO₂ mobility can be explained by the repulsive force between nTiO₂ and quartz sand, both of which were negatively charged with an energy barrier of 51.8 k_BT (Table 2).

Fe oxyhydroxide-coated sand column. Effluent nTiO₂ concentration was high for the Fe oxyhydroxide-coated sand column ($C/C_0 = \sim 0.93$). Effluent pH of the Fe oxyhydroxide-coated sand column also reduced from that of the influent (9.0 - 8.2) (Fig. S7-d, SI). As previously discussed, at this lower pH of 8.2, the Fe oxyhydroxide coating carried positive charges and could provide favorable sites for nTiO₂ deposition, which might result in low transport. The experimentally observed high nTiO₂ transport could be explained by phosphate adsorption to the Fe oxyhydroxides coating. When the nTiO₂-phosphate suspension was injected into the column, phosphate could adsorb to the Fe oxyhydroxide coating, especially at pH lower than the pH_{pzc} of Fe oxyhydroxide, where the Fe oxyhydroxide was positively charged (Borggaard et al., 2005). Phosphate adsorption could neutralize the positive charges or even make the surface charge of Fe oxyhydroxides negative (Bolan and Barrow, 1984). This could reduce the electrostatic attraction between negatively charged nTiO₂ and the Fe oxyhydroxide coating, and thus increase nTiO₂ transport. For the Fe oxyhydroxide-coated sand column, it was noted that the maximum effluent concentration did not occur until ~ 3.5 PV. The delay in nTiO₂ transport was related to higher nTiO₂ deposition rate at the beginning of injection, when the amount of phosphate adsorbed to the Fe oxyhydroxide coating was low and the Fe oxyhydroxide coating was still positively charged. Furthermore, as previously discussed, surface roughness of the Fe oxyhydroxide coating could

reduce energy barrier and increase retention, also contributing to the delay in nTiO₂ breakthrough (Fig. 7-b).

3.3.2.8. nTiO₂–phosphate–illite suspension at pH 9 (brown triangle (Δ) in Fig. 7-c & 7-d)

Quartz sand and Fe oxyhydroxide-coated sand columns. The BTCs for the quartz sand column and Fe oxyhydroxide-coated sand column when the nTiO₂–phosphate–illite suspension was used as influent (Fig. 7-c & 7-d) was similar to that for the quartz sand column when nTiO₂–phosphate suspension was used as influent (Fig. 7-a). The high mobility in the nTiO₂–phosphate–illite experiments was due to the repulsive forces between each of the particles (nTiO₂ and illite colloid) and between nTiO₂ and medium surfaces (quartz and Fe oxyhydroxide) (Table 2), all of which were negatively charged because of high pH and phosphate adsorption. The faster breakthrough of nTiO₂ in the presence of illite in the Fe oxyhydroxide coated column (Fig. 7-d vs. 7-b) can be explained by the competition from illite colloids for the favorable deposition sites on the Fe oxyhydroxide coating, which decreased nTiO₂ retention.

3.3.3. Modeling nTiO₂ transport

The optimized parameters for nTiO₂ retention ($S_{1\max}$, $S_{2\max}$, k_{1att} , k_{2att} , and k_{str}) are summarized in Table 3. The one-site model provided good simulation for all the BTCs at pH 9 (except for the Fe oxyhydroxide sand column with nTiO₂–phosphate suspension as influent, for which a two-site model was required), whereas the two-site model was required to properly simulate the nTiO₂ BTCs at pH 5, due to the complex mechanisms involved in the nTiO₂ retention, such as blocking and straining (Fig. 7 & Table 3).

Table 3. The fitted parameters for the nTiO₂ breakthrough curves.

pH	Influent suspension	Medium type	k _{1att} (1/min)	S _{1max} (μg/g)	k _{2att} (1/min)	S _{2max} (μg/g)	k _{str} (1/min)	R ²	BTC shown in	
5	nTiO ₂	Quartz sand	0.376±0.018	1.816±0.029	0.004±0.001	1.445±0.067		0.99	Fig. 7-a (◇)	
		Fe-coated sand	0.174±0.012	0.416±0.002	0.004±0.003	1.111±0.115		0.99	Fig. 7-b (◇)	
	nTiO ₂ -illite	Quartz sand	0.087±0.007	0.442±0.184			0.437±0.044	0.92	Fig. 7-c (◇)	
		Fe-coated sand	0.087±0.002	1.044±0.154			0.222±0.018	0.98	Fig. 7-d (◇)	
	nTiO ₂ -phosphate	Quartz sand							Fig. 7-a (□)	
		Fe-coated sand							Fig. 7-b (□)	
	nTiO ₂ -phosphate-illite	Quartz sand							Fig. 7-c (□)	
		Fe-coated sand							Fig. 7-d (□)	
	9	nTiO ₂	Quartz sand	0.003±8×10 ⁻⁴	0.220±0.113				0.99	Fig. 7-a (×)
			Fe-coated sand	0.099±0.003	8.117±2.880				0.88	Fig. 7-b (×)
		nTiO ₂ -illite	Quartz sand	0.001±9×10 ⁻⁴	0.060±0.109				0.98	Fig. 7-c (×)
			Fe-coated sand	0.002±4×10 ⁻⁴	0.030±6.444				0.99	Fig. 7-d (×)
nTiO ₂ -phosphate		Quartz sand	0.017±0.004	0.074±0.013				0.98	Fig. 7-a (Δ)	
		Fe-coated sand	0.171±0.029	0.513±0.003	0.003±0.003	0.373±0.046		0.98	Fig. 7-b (Δ)	
nTiO ₂ -phosphate-illite		Quartz sand	0.002±9×10 ⁻⁴	0.090±0.041				0.99	Fig. 7-c (Δ)	
		Fe-coated sand	0.007±0.002	0.090±0.020				0.97	Fig. 7-d (Δ)	

Blanks indicate a value for the parameter did not exist.

3.3.3.1. nTiO₂ and nTiO₂-illite suspension at pH 5 (blue diamonds (◇) in Fig. 7)

Modeling results indicated that in the experiments using the pH 5 nTiO₂ suspension as influent, the two-site model fitted well. The calculated deposition site density and deposition rate coefficient for the quartz sand column (S_{1max} = 1.816 and S_{2max} = 1.445 μg/g, k_{1att} = 0.376 1/min)

were greater compared to those for the Fe oxyhydroxide-coated sand column ($S_{1\max} = 0.416$ and $S_{2\max} = 1.111 \mu\text{g/g}$, $k_{1\text{att}} = 0.174 \text{ 1/min}$) (Fig. 7-a vs. 7-b). This was consistent with our previous discussion of the repulsive forces between nTiO₂ and the patchy Fe oxyhydroxide coating, which decreased the overall deposition relative to that in the quartz sand column.

The two-site model with straining provided a good simulation for the BTCs from experiments using the pH 5 nTiO₂-illite suspension. Even though nTiO₂ retention was more pronounced with the nTiO₂-illite suspension as influent than that with the nTiO₂ suspension as influent at pH 5 (Fig. 7-c and 2-d), the total reversible site density ($S_{1\max}$) for the nTiO₂-illite suspension experiments ($0.442 \mu\text{g/g}$ for quartz sand and $1.044 \mu\text{g/g}$ for Fe oxyhydroxide-coated sand) was lower compared to the total reversible site density (i.e., $S_{1\max} + S_{2\max}$) for the nTiO₂ suspension experiments ($S_{1\max} + S_{2\max} = 3.261 \mu\text{g/g}$ for quartz sand, and $S_{1\max} + S_{2\max} = 1.527 \mu\text{g/g}$ for Fe oxyhydroxide-coated sand). Modeling results indicated that the higher nTiO₂ retention in the nTiO₂-illite experiments was caused by straining with straining coefficients in the range of $0.222\text{--}0.437 \text{ 1/min}$ (Table 3). These results were in agreement with our discussion in Section 3.3.2 that straining was an important retention mechanism when illite colloids were present in the influent.

3.3.3.2. nTiO₂ and nTiO₂-illite suspension at pH 9 (red times (×) in Fig. 7)

The $S_{1\max}$ and $k_{1\text{att}}$ for the quartz sand column experiment with the pH 9 nTiO₂ suspension as influent were low ($S_{1\max} = 0.220 \mu\text{g/g}$, $k_{1\text{att}} = 0.003 \text{ 1/min}$). The calculated $S_{1\max}$ and $k_{1\text{att}}$ were also low for the experiments with the nTiO₂-illite suspension as influent ($S_{1\max} = 0.030\text{--}0.060 \mu\text{g/g}$) and $k_{1\text{att}}$ ($0.001\text{--}0.002 \text{ 1/min}$). These low $S_{1\max}$ and $k_{1\text{att}}$ values were due to the repulsive forces between the negatively charged nTiO₂ and collector surfaces (i.e., quartz and Fe oxyhydroxide), as discussed in Section 3.3.2. Much higher $S_{1\max}$ ($8.117 \mu\text{g/g}$) and $k_{1\text{att}}$ (0.099

1/min) values were calculated for the Fe oxyhydroxide-coated sand column with the pH 9 nTiO₂ suspension as influent. As discussed in Section 3.3.2, the higher deposition in this case was caused by the Fe oxyhydroxide coating, which provided favorable deposition sites at pH < the p*H*_{pzc} of the Fe oxyhydroxide.

3.3.3.3. nTiO₂–phosphate and nTiO₂–illite–phosphate suspensions at pH 9 (brown triangles (Δ) in Fig. 7)

For all the column experiments with phosphate in the influent at pH 9, except the Fe oxyhydroxide-coated sand column with the nTiO₂–phosphate suspension as influent (Fig. 7-b), the calculated S1_{max} and k_{1att} were very small (Table 3). These low S1_{max} and k_{1att} reflected the high mobility of the particle, which was due to the high energy barriers between the negatively charged nTiO₂ and medium surfaces (i.e., quartz and/or Fe oxyhydroxide coating with modified surface charge upon encountering phosphate). In the Fe oxyhydroxide-coated sand column with the nTiO₂–phosphate suspension as influent (Fig. 7-b), the two-site model with blocking worked well. The values of S1_{max} (0.513 μg/g), S2_{max} (0.373 μg/g), k_{1att} (0.171 1/min), and k_{2att} (0.003 1/min) were higher compared to those for the other experiments at pH 9 with phosphate in the influent (Table 3). This was in agreement with the delay in nTiO₂ release in that experiment and due to the attractive electrostatic forces between the nTiO₂ and Fe oxyhydroxide coating at the early stage of injection when the Fe oxyhydroxide coating was still positively charged (discussed in Section 3.3.2.7).

3.4. Conclusions

This study showed that the co-presence of common groundwater and aquifer components such as dissolved phosphate, suspended illite colloids, and Fe oxyhydroxide coating on quartz sand could significantly influence nTiO₂ aggregation and transport, and the nature of such influence

was strongly pH dependent and governed by the interactions between nTiO₂ and these components and between different components. At pH 5, in the absence of phosphate, Fe oxyhydroxide coating was found to increase nTiO₂ transport via electrostatic repulsion, whereas illite colloid was found to attract and entrap nTiO₂ and hence reduce its transport. Dissolved phosphate at pH 5 had high affinity for nTiO₂ and served as bridges between nTiO₂ particles, resulting in large aggregates, which were immobilized due to physical straining. At pH 9, neither illite colloid nor phosphate influenced nTiO₂ aggregation or transport in quartz sand since phosphate adsorption to all surfaces was negligibly low, and all the particle and media surfaces carried negative charges and repelled each other. In contrast, Fe oxyhydroxide coating considerably hindered nTiO₂ transport when influent pH = 9, as a result of pH buffering by Fe oxyhydroxide, which decreased pH to the range between the p*H*_{pzc} of nTiO₂ and that of Fe oxyhydroxide (i.e., 6.8 < pH < 8.4), and thus made the Fe oxyhydroxide and nTiO₂ oppositely charged. Under such conditions, both phosphate and illite colloid enhanced nTiO₂ transport, as they competed against nTiO₂ for deposition sites on the positively charged Fe oxyhydroxide coating and reduced nTiO₂ retention. Findings from this study illuminated some of the geochemical reactions that need to be considered when evaluating the behaviours of engineered nanomaterials under complex physicochemical conditions, which help to better understand the fate and transport of these emerging contaminants in the natural environment.

Acknowledgments

This work was supported by Natural Sciences and Engineering Research Council of Canada's Discovery Grant (No. 402815-2012) and Canada Foundation of Innovation's Leaders Opportunity Fund (No. 31836).

Appendix 2. Supplementary data

Supplementary material related to this chapter can be found, in the Appendices. All the original data are provided in electronic format.

Chapter 4. The role of Fe oxyhydroxide coating, illite clay, and peat moss in nanoscale titanium dioxide (nTiO₂) retention and transport in geochemically heterogeneous media

(Rastghalam, Z.S., Yan, C., Shang, J., Cheng, T. The role of Fe oxyhydroxide coating, illite clay, and peat moss in nanoscale titanium dioxide (nTiO₂) retention and transport in geochemically heterogeneous media. (Submitted to Environmental pollution))

Natural media such as soil and sediment contain mineralogical/organic components with distinct chemical, surface, and electrostatic properties. To better understand the role of various mineralogical/organic components, columns were packed with quartz sand and natural sediment with added Fe oxyhydroxide coating, illite clay, and peat moss to investigate how these added components influence nTiO₂ retention and transport in geochemically heterogeneous medium. Results showed that nTiO₂ transport was low at pH 5, attributable to the electrostatic attraction between positively-charged nTiO₂ and negatively-charged medium. While illite did not notably affect nTiO₂ transport at pH 5, Fe oxyhydroxide coating increased nTiO₂ transport due to electrostatic repulsion between Fe oxyhydroxide and nTiO₂. Peat moss also increased nTiO₂ transport at pH 5, attributable to the increased DOC concentration, resulting in a higher DOC adsorption to nTiO₂ and the intensified electrostatic repulsions between nTiO₂ and the medium. At pH 9, nTiO₂ transport was high due to the electrostatic repulsion between negatively-charged nTiO₂ and medium surfaces. Fe oxyhydroxide coating at pH 9 slightly delayed nTiO₂ transport due to electrostatic attraction, while illite clay and peat moss substantially inhibited nTiO₂ transport via electrostatic attraction and/or straining/entrapment. Overall, this study demonstrated that pH has a considerable effect on how mineral/organic component of a medium influence nTiO₂ transport. At low pH, electrostatic interaction was the dominant mechanism, therefore, nTiO₂ transport was low regardless of the differences in minerals/organic components. Conversely,

nTiO₂ mobility was substantial at high pH and sensitive to the soil/sediment minerals and organic matter content due to straining and surface roughness.

Keywords: Nanoscale titanium dioxide particle (nTiO₂) retention and transport, Natural sediment, Fe oxyhydroxide, Illite clay, Peat moss.

4.1. Introduction

Transport of water-borne contaminants (e.g., dissolved ions, virus, and bacteria) in soil and groundwater is influenced by water chemistry and property of the transport media (Hu and Shipley, 2012; Sasidharan et al., 2017, 2016; Zhang et al., 2013). Due to the development and application of nanotechnology, engineered nanoparticles (ENPs) such as nanoscale titanium dioxide (nTiO₂) are being released into the aquatic environment (Nowack and Bucheli, 2007; Pachapur et al., 2016). To evaluate environmental impacts of these emerging contaminants, extensive laboratory research has been conducted to understand their transport in porous media (Lin et al., 2010; Park et al., 2016; Sharma, 2009; Xu, 2018). Many of these studies focus on the influence of water chemistry (e.g., pH, ionic strength, dissolved ions and NOM), and quartz sand or glass bead columns are often used as surrogates for natural transport media (Bradford and Bettahar, 2006; Chen et al., 2012; Lv et al., 2016; Solovitch et al., 2010; Tian et al., 2012). Nonetheless, natural media such as soil and sediments are composed of distinct mineralogical and organic components, and each of these components has very different surface and electrostatic properties in comparison to quartz sand or glass bead. Natural porous media can influence particle transport by providing deposition sites and changing pore water chemistry. (Cornelis et al., 2013; Fang et al., 2011, 2009; Park et al., 2016; Sun et al., 2015a). To date, however, less attention has been paid to the effect of porous media, and therefore more studies are required to clarify the effect of mineralogical and organic components in the medium on ENP transport, especially in highly complex media such as

natural soil/sediments (Akanbi et al., 2018; Ben-Moshe et al., 2010; Chowdhury et al., 2012; Kim et al., 2015; Pachapur et al., 2016; Wang et al., 2014). .

Natural organic matter (NOM), Fe/Al oxyhydroxides, and clay minerals are the most important natural components in soil/sediments that adsorb and influence the transport of dissolved contaminants such as heavy metal and radionuclide ions (Cheng et al., 2004; Fisher-Power et al., 2019; Mizutani et al., 2017; Shi et al., 2007). Size, surface morphology, and electrostatic properties of NOM, Fe/Al oxyhydroxides, and clay minerals are very different from those of quartz sand. Besides, NOM, Fe/Al oxyhydroxides, and clay minerals can change water chemistry via pH buffering and by releasing/adsorbing NOM and multivalent cations in/from pore water (Fisher-Power and Cheng, 2018; Zhou and Cheng, 2018). As a result, an in-depth insight and discussion of the mechanisms involved, and the identification of the predominant ones, would be necessary while investigating the influence of NOM, Fe/Al oxyhydroxides, and clay minerals on ENP transport in natural porous media. NOM occurs both in the solid and aqueous phase in subsurface environments. As a ubiquitous component in soil water and groundwater, dissolved organic matter (DOM) has been shown to adsorb to mineral surface and influence the stabilization, deposition, and transport of colloids and ENPs, and the nature of such influence depends on pH, DOM concentration, and cation type (Li et al., 2013; Tang and Cheng, 2018; Wilkinson et al., 1997; Wu and Cheng, 2016; Zhang et al., 2009). The role of NOM in the transport media (i.e., solid phase) has been less researched (Carstens et al., 2018; Westerhoff and Nowack, 2013). El Hadri et al. (2018) demonstrated that NOM, which decreases the influence of native surface chemistry and functional coatings, is a key factor controlling Au nanoparticle adhesion to matrix. Partial dissolution of solid soil organic matter (SOM) in soil and sediment releases DOM to the pore water. The negatively charged DOM can adsorb to the positively charged nTiO₂ at pH < p*H*_{pzc} of

nTiO₂, while hardly adsorbs negatively charged nTiO₂ at pH > pH_{pzc} of nTiO₂ due to electrostatic repulsion (Wu and Cheng, 2016).

Fe/Al oxyhydroxides often exist as patch-wise coatings on soil/sediment grains (Ryan et al., 1999; Ryan and Gschwend, 1992). Unlike most other natural minerals and organics, Fe/Al oxyhydroxides have a high point of zero charge (PZC) (> 8) (Huang, 1995; Parks, 1965; Wang et al., 2012). As such, Fe/Al oxyhydroxides can carry positive charges in the pH range of natural water and patchy Fe/Al oxyhydroxide coatings on soil/sediment grains could result in surface charge heterogeneity. While a number of studies demonstrated that at acidic or near neutral pH, electrostatic attraction between ENP and Fe oxyhydroxide coating on quartz sand (or silica beads) dominated ENP deposition (Han et al., 2014; Lin et al., 2011; Wang et al., 2013, 2012; Wu and Cheng, 2016), effect of Fe/Al oxyhydroxide coatings in natural soil/sediments on particle transport is more complicated but less studied. A recent study showed that in the pH range 5–6 (< pH_{pzc} of Fe/Al oxyhydroxides and nTiO₂), nTiO₂ mobility in a natural sediment with Fe/Al oxyhydroxides depleted was lower than that in the unmodified sediment, but higher than that in the same sediment with NOM depleted (Fisher-Power and Cheng, 2018). It was proposed that the interactions between NOM and Fe/Al oxyhydroxides as well as between NOM and nTiO₂ need to be considered to elucidate the role of Fe/Al oxyhydroxides in natural sediments (Fisher-Power and Cheng, 2018).

Water-borne clay colloids are ubiquitous in soil water and groundwater and they influence nanoparticle transport by attracting nanoparticles and forming clay-ENP heteroaggregates (Tang et al., 2018; Tang and Cheng, 2018; Zhou et al., 2012). Depending on the size and surface charge of the heteroaggregates formed, clay colloids either promote or hinder the transport of ENPs. (Cai et al., 2014). When occurring in porous limestone media, clay minerals are reported to increase

ENP retention, attributable to the increased straining and entrapment of ENPs in the fibrous structure of the clay minerals (Bayat et al., 2015). In another study, however, it is observed that retention of nanoscale zero valent iron (nZVI) in quartz sand columns decreased with increasing mass of kaolinite clay in the column (Jung et al., 2014), as a result of stronger electrostatic repulsion between nZVI and kaolinite in comparison to that between nZVI and quartz (Jung et al., 2014). While a number of studies have reported that clay minerals may either inhibit or promote the mobility of dispersed colloids, the effect of clay minerals depends not only on the amount of clay, but also on other factors such as pH and other soil/sediment components. How pH controls the influence of clay mineral on nTiO₂ transport in geochemically heterogeneous media has not been investigated before. When various mechanisms are at work in complex systems, the effect of a single soil/sediment component on particle transport is not predictable in the absence of systematic experiments. Although some progress has been made towards the understanding of how porous media influences ENP transport, substantial knowledge gaps exist, especially in terms of the effect of diverse mineralogical and organic components in media with *natural soil/sediment*. In previous studies (Bayat et al., 2015; Jung et al., 2014; Zhou and Cheng, 2018), simplified media (such as quartz sand or limestone), which does not represent well the geochemical heterogeneity of natural soils/sediments, were used. Hence, it is not clear if the results from previous studies can be extrapolated to heterogeneous natural media. Whereas in this study, natural sediment was used in the transport medium. The sediment used in this study was similar to natural medium in terms of its mineralogical and organic matter composition, not its structure. Additionally, in most of these studies, only one type of the component (e.g., NOM, Fe/Al oxyhydroxide, or clay mineral) was examined. At the same time, the medium type (e.g., limestone vs. quartz sand), water chemistry, and hydrological conditions were quite different across studies. Therefore, it is difficult

to make a direct comparison of the effect of NOM, Fe/Al oxyhydroxide, and clay mineral under similar conditions. To better distinguish the distinct roles of NOM, Fe/Al oxyhydroxides, and clay minerals, it would be valuable to determine the effect of these minerals/organics using the same type of medium under similar water chemistry and hydrological conditions. The objective of this current study is aimed at elucidating the role of NOM, Fe oxyhydroxides and clay minerals in nTiO₂ transport in a geochemically heterogeneous medium at different pH. The pH range we applied in this study is comparable to the pH of natural soil/sediment used in many similar studies (Fang et al., 2011, 2009; Larue et al., 2018). The pH selected (5 and 9) can mimic different scenarios which are likely to occur under natural conditions, where nTiO₂ particles are either positively charged or negatively charged. Columns were packed using the mixture of quartz sand and a well-characterized natural sediment. Sphagnum peat moss, Fe-oxyhydroxide, and illite powder were added to some of the columns as representing NOM, Fe oxyhydroxide, and clay mineral. Sphagnum peat moss, or Fe oxyhydroxide, or illite powder was well mixed with quartz sand and sediment before being used in some of the columns. By comparing the nTiO₂ breakthrough curves (BTCs) from different column experiments, coupled with zeta potential and hydrodynamic diameter (HDD) measurements, as well as theoretical consideration, the role of NOM, Fe-oxyhydroxide, and clay minerals in nTiO₂ transport was identified and the retention mechanisms were proposed.

4.2. Materials and methods

4.2.1. Materials

All chemical reagents used in this study were of ACS analytical grade and nanopure water (resistivity >18.2 MΩ × cm, dissolved organic carbon (DOC) < 0.02 mg/L) was used for preparing all the solutions and suspensions. Aeroxide[®] TiO₂ P25 powder was purchased from Fisher

Scientific (Ontario, Canada) with a reported purity of > 99.5%, a specific surface area of 50 ± 15 m²/g, and a primary average particle size of 21 nm. XRD analysis showed that the TiO₂ P25 powder was mainly composed of anatase (90%) with low quantities of rutile (10%) (Wu and Cheng, 2016).

A natural sediment sample was collected from a depth of 0.6–1.0 m at a site located in the south coast of the Island of Newfoundland, Canada. The sediment was air-dried, exogenous impurities removed and sieved through a 2 mm sieve. Sediment pH was determined using a sediment–nanopure water mixture with a ratio of 1:5 (w/v). The mixture was shaken on a VWR Standard Analog Shaker at 300 rpm for 30 minutes before pH measurement. Sediment sand, silt and clay content was determined by a Horiba LA-960 Laser Particle Size Analyzer. X-ray diffraction (XRD) spectra of the sediment were generated using a Rigaku Ultima IV diffractometer. Soil organic carbon (SOC) of the sediment was measured by elemental combustion analysis using a Carlo Erba NA1500 Series II Elemental Analyzer. The total extractable Fe (both amorphous and crystalline) of the sediment was quantified by Citrate-bicarbonate-dithionite (CBD) extraction method (Mehra and Jackson, 1960). Concentrations of amorphous Fe/Al oxyhydroxides in the sediment were determined by acid ammonium oxalate extraction under darkness (AOD) method (McKeague and Day, 1966). The Fe and Al concentrations of the extraction solutions were measured by an ICP-MS.

Quartz sand (U.S. Silica) was sieved to the size range of 0.6–0.7 mm. To remove metal oxides and organic impurities, the sand was acid washed using the procedure of Wu and Cheng (2016). After acid washing, the quartz sand was rinsed repeatedly with nanopure water until the pH was near 7 and then oven-dried at 120°C overnight.

Fe oxyhydroxide-coated quartz sand was prepared following the procedure described by Wu and Cheng (2016). Briefly, the pre-treated quartz sand (described above) was mixed with FeCl_3 solution, with the pH of the mixture adjusted to ~ 4.5 , before the mixture was shaken vigorously on a VWR orbital shaker at 300 rpm for 24 hours. After shaking, the coated sand was thoroughly rinsed with 0.01 M NaOH solution followed by deionized water multiple times until the color and pH of the flushing fluid became stable. Afterward, the coated sand was oven-dried at 120°C overnight. Scanning electron microscopy (SEM) coupled with energy dispersive X-ray (EDX) was used to determine the fraction of the sand surface covered by Fe oxyhydroxide using the procedure by (Wang et al., 2012; Wu and Cheng, 2016). The mass concentration of the Fe oxyhydroxide coating on the sand was measured using the digestion procedure of EPA method 3050b with modification (USEPA, 1996), followed by ICP-MS analysis as described in a previous paper (Rastghalam et al., 2019). Illite powder (IMt-2 Illite-Cambrianshale, Clay Mineral Society) was purchased from the Clay Minerals Society. The illite powder was passed through a 2 mm sieve to exclude coarse grains and the grain size distribution of the sieved illite was determined by a Horiba LA-960 Laser Particle Size Analyzer.

Peat moss (Hoffman 15503, Canadian sphagnum peat moss, 10 quarts, premium grade) was sieved to < 2 mm in size and oven dried at 80°C . The moisture content of the peat moss (8 ± 1 %) was determined by the mass difference before and after oven drying. The pH (6.8 ± 0.1), grain size distribution, d_{50} (682 ± 93 μm), and organic carbon content (40.2 ± 4.5 %) of the peat moss were previously determined (Zhou and Cheng, 2018).

4.2.2. Methods

4.2.2.1. Preparation of the nTiO₂ suspension and background solution

Aqueous nTiO₂ suspension (100 mg/L) was prepared by suspending the Aeroxide[®] TiO₂ powder in nanopure water. To achieve a homogeneous and dispersed nTiO₂ suspension, the mixture was sonicated at 200 W for 30 minutes by a Branson Digital Sonifier that includes a converter, a disruptor, and a probe (Crystal Electronics). Solid NaCl was dissolved in nanopure water to prepare the 0.1 M NaCl solution for ionic strength adjustment. Concentrated HCl solution (36.5–38.0%) was diluted using nanopure water to prepare the 0.1 M HCl solution, and solid NaOH was dissolved in nanopure water to prepare the 0.1 M NaOH solution. The pH of the nTiO₂ suspension and the background solution was adjusted to 5 ± 0.05 or 9 ± 0.1 using small volumes of the 0.1 M HCl and NaOH solutions, and the ionic strengths of the suspension and background solution were adjusted to 1 mM using the 0.1 M NaCl solution.

4.2.2.2. Zeta potential (ZP) and hydrodynamic diameter (HDD) measurement

Zeta potential and HDD of the nTiO₂ suspensions were measured utilizing a zetasizer Nano-ZS (Malvern). Laser Doppler velocimetry coupled with phase analysis light scattering was used to determine particle electrophoretic mobility, which was then converted to zeta potential using the Smoluchowski equation. The HDD was measured based on dynamic light scattering (DLS).

Samples for sediment zeta potential measurement was prepared by mixing 1 g of the dry sediment with 40 mL of 1 mM NaCl solution, adjusting the pH to 5 and 9, shaking on a VWR shaker at 300 rpm overnight, and re-adjusting the pH. Zeta potential of the supernatant was measured by the zetasizer Nano-ZS after 1 hour of gravity settling.

The zeta potentials of quartz sand and illite clay (Rastghalam et al., 2018), Fe oxyhydroxide powder (Wu and Cheng, 2016), and peat moss (Zhou and Cheng, 2018) were determined previously.

4.2.2.3. Column experiments

Eight column experiments, distinguishable based on the influent pH (5 and 9) and the components in the transport media, were conducted. For each experiment, dry natural sediment and quartz sand (or Fe-coated quartz sand) were well mixed at a 1:4 mass ratio before being used for packing the column. For some of the experiments, 2.6 g illite clay per column (2 wt%) or 0.26 g peat moss per column (0.2 wt%) was added to the quartz sand–sediment mixture for packing (Table S1, SI). Quartz sand–sediment mixture, rather than sediment sample itself, was used to maintain sufficient hydraulic conductivity and ensure that the column stoppers were not clogged by high concentrations of the fine particles from the sediment. Quartz is a natural component of the sediment (Section 4.3.1), therefore mixing of quartz sand with the sediment did not introduce additional types of minerals to the sediment.

A cylindrical column (Kontes Chromaflex chromatography) (length of 15 cm and inner diameter of 2.5 cm) was used to hold the transport media. The column consisted of a borosilicate glass barrel and two high-density polyethylene bed supports (20 μm pore size) on both ends and was set up vertically. Small portions of medium materials were poured into the column followed by gently pumping nTiO₂–free background solution upward using a Masterflex peristaltic pump. Then more medium materials were added to the column and more background solution pumped until the column was fully packed. The column was tapped several times during the packing step to ensure uniform packing and to remove any air bubbles. The mass of the medium and the solution

used to saturate the medium was recorded to determine the bulk density, porosity, and pore volume for each column.

Once a column was packed, nTiO₂-free background solution with pH and background electrolyte matching those of the influent suspension was introduced into the column for ~16 hours at a flow rate of 1 mL/min (average water velocity = 0.51 cm/min) using the Masterflex peristaltic pump. The 16-hour flushing was used to equilibrate the system chemically and hydrodynamically. nTiO₂ suspension was then injected into the column (~6 PV for the pH 5 experiments and ~5 PV for the pH 9 experiments) at the same flow rate, followed by injection of the nTiO₂-free background solution until no particles could be detected in the effluent.

The pH of the influent suspensions was monitored and maintained within the range of 5.0 ± 0.05 or 9.0 ± 0.1. Light absorbance of the influent suspension was monitored by a Thermo Scientific GENESYS 10S UV-vis spectrophotometer at a wavelength of 368 nm (Wu and Cheng, 2016). The calibration curves were conducted in each experiment by plotting the light absorbance vs. concentration using particle-free 1 mM NaCl solutions as blanks and standards with known nTiO₂ concentrations. Effluent samples were collected using a fraction collector (Spectrum Laboratories CF-2) and their light absorbance measured at a wavelength of 368 nm by the spectrophotometer and converted to nTiO₂ concentration based on calibration curves. Our experimental results showed that the interfere from DOC is negligible at this wavelength. nTiO₂ breakthrough curves (BTCs) were generated by plotting relative effluent concentration (C/C_0) (C and C_0 are the effluent and influent nTiO₂ concentration respectively) as a function of pore volume (PV) (i.e., V/V_0 , where V is cumulative effluent volume, and V_0 is column pore volume). The pH and electrical conductivity (EC) were measured for the effluent samples collected at ~1, 3, and 6 PV, representing the effluent at the beginning, middle and towards the end of the injection phase.

The effluent samples were then combined into a composite sample to determine the mean effluent zeta potential, HDD, and DOC during injection. All the column experiments were performed in duplicate at room temperature (~ 22 °C).

4.2.3. DLVO calculations

Particle-to-collector (quartz sand, Fe oxyhydroxide coating, illite, and peat moss) interaction energy profiles were calculated with the assumption of sphere-plate geometry, following the classic Derjaguin-Landau-Verwey-Overbeek (DLVO) theory (Derjaguin and Landau, 1941; Verwey and Overbeek, 1948). Details on the interaction energy calculation were described in the Supporting information (SI).

4.3. Results and discussions

4.3.1. Properties of the sediment, Fe oxyhydroxide coated sand, and illite

The organic carbon content of the sediment was 5.8 ± 0.1 mg/g and the pH of the sediment in nanopure water was 5.7 ± 0.04 . The XRD analysis showed the presence of quartz, albite, anorthite, and Fe oxyhydroxides in the sediment (Fig. S9, SI). The Fe/Al oxyhydroxide concentrations of the sediment were: CBD extractable Fe = 4.0 ± 0.6 mg/g, AOD extractable Fe = 3.2 ± 0.1 mg/g, and AOD extractable Al = 2.5 ± 0.02 mg/g. For the Fe oxyhydroxide coated sand, SEM-EDX analysis showed that 13.5 ± 3 % of the surface was coated with Fe oxyhydroxide, and the Fe concentration was 0.10 ± 0.02 mg Fe per g of sand measured by ICP-MS (Rastghalam et al., 2019). Grain size distribution analysis showed that the sediment was composed of 78.1 ± 1.9 % sand, 21.3 ± 1.9 % silt, and 0.6 ± 0.1 % clay, with a median diameter (d_{50}) of 212 ± 36 μm (Fig. S10, SI). For the illite clay used in this experiment, the median diameter (d_{50}) was determined to be 150 ± 26 μm (Fig. S11, SI).

4.3.2. nTiO₂ transport

The flow velocity, column pore volume, porosity, and bulk density were similar between different columns, indicating that these properties were not considerably influenced by the Fe oxyhydroxide, illite clays, or peat moss addition to the columns (Table S3, SI).

The pH and medium type considerably influenced nTiO₂ transport. For each medium type, effluent nTiO₂ concentrations at pH 5 were much lower than those at pH 9 (Fig. 8), with nTiO₂ mass recovered from the effluent ranging from 11%–15% for the pH 5 experiments and from 73%–95% for the pH 9 experiments (Table S3, SI).

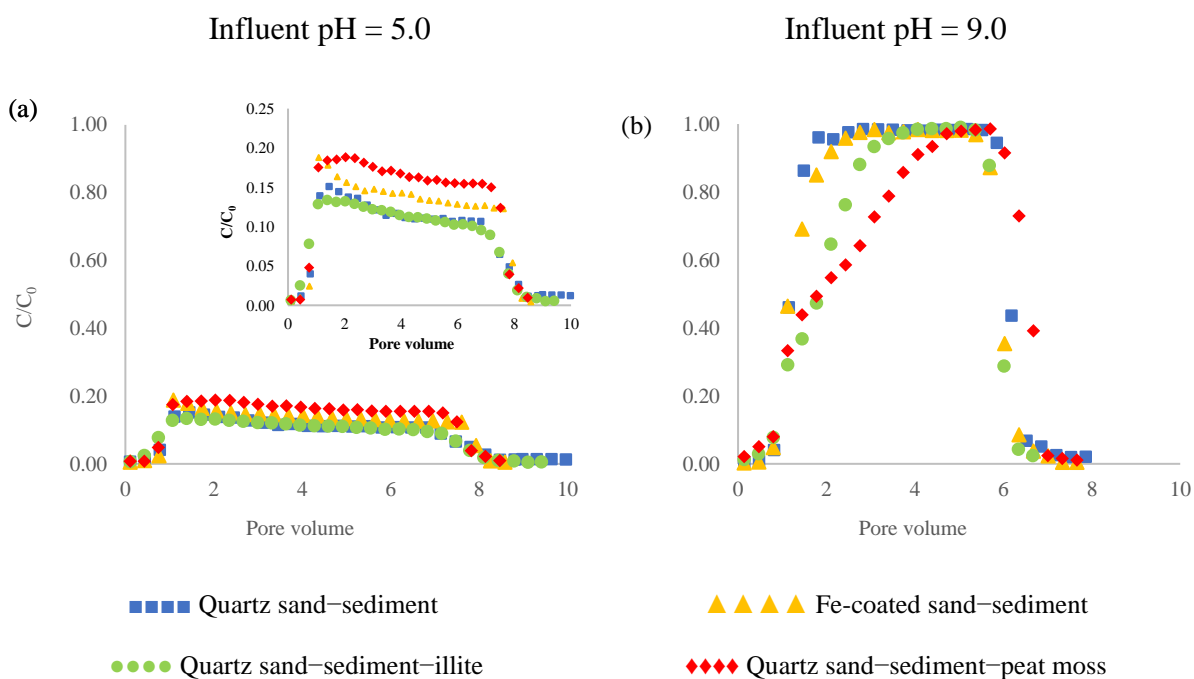


Fig. 8. nTiO₂ BTCs for experiments conducted in columns with various media at pH 5 (a) and 9 (b). Illite and peat moss in the column = 2.6 g and 0.26 g, respectively. Influent nTiO₂ concentration = 100 mg/L and background solution = 1 mM NaCl. C_0 and C represent influent and effluent particle concentration, respectively. The inset in Fig 8-a is a zoom-in version of the BTCs. The BTCs with error bars are provided in (Fig. S12, SI).

The influence of Fe oxyhydroxide, illite clay, and peat moss on transport was also pH dependent. At pH 5, Fe oxyhydroxide and peat moss increased transport relative to that of the quartz sand–sediment column, whereas illite clay did not seem to change transport (Fig. 8-a & Table S9, SI). At pH 9, Fe oxyhydroxide, illite, and peat moss all hindered transport, with the Fe oxyhydroxide having a minor effect and the illite and peat moss having substantial effects (Fig. 8-b & Table S3, SI). For the pH 5 experiments, the pH range is from 5 to ~6, while for the pH 9 experiments, the pH range is from 9 to ~6 (Fig. 9-a & 9-b). These different pH ranges caused the difference in the nTiO₂ zeta potential and eventually varying BTCs (Fig. 9-c & 9-d & Fig. 8).

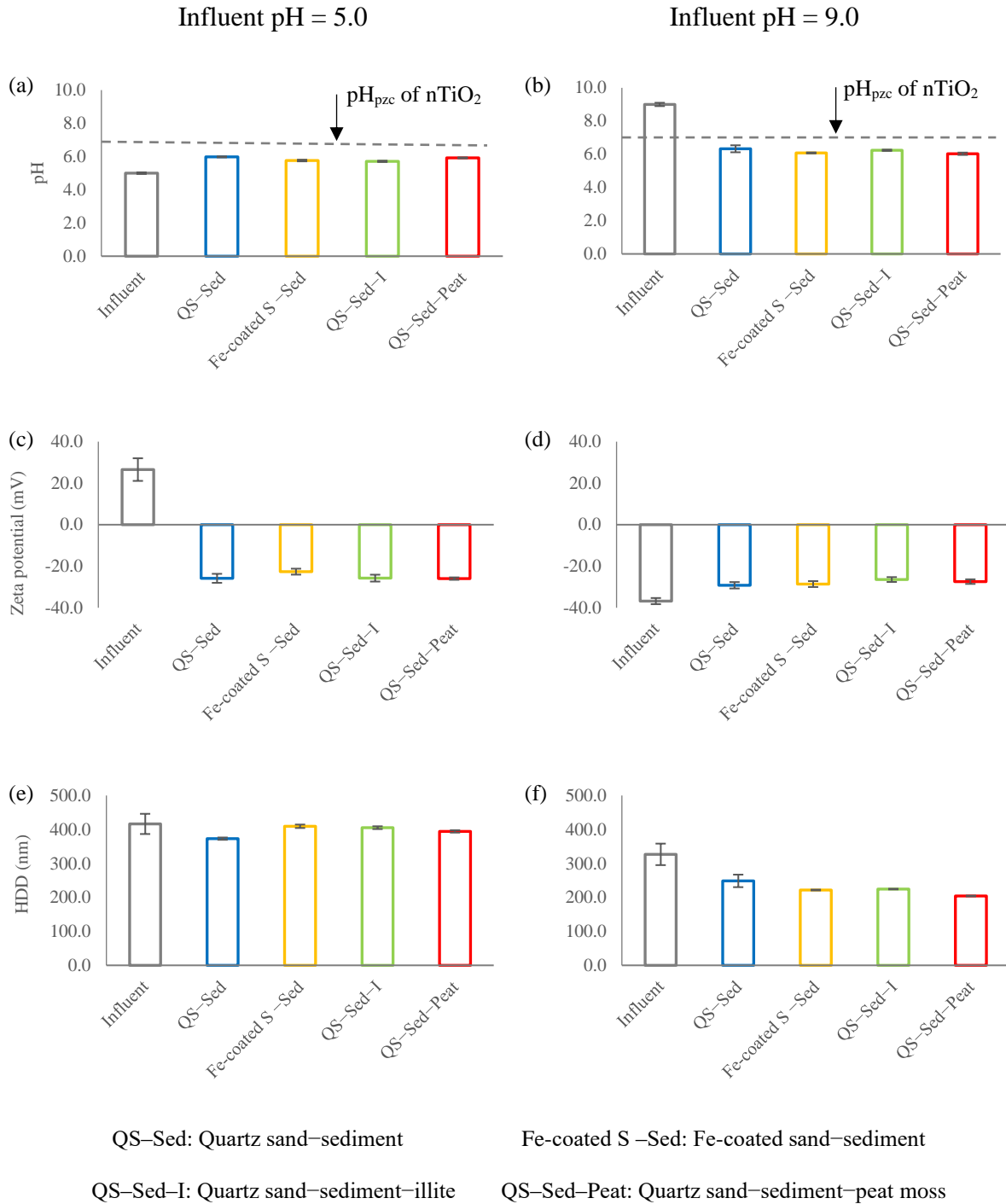


Fig. 9. The mean pH (a & b), zeta potential (c & d), and HDD (e & f) of various columns' effluent. The pH, zeta potential, and HDD of the influent are also plotted for comparison. Illite and peat moss in the column = 2.60 g and 0.26 g, respectively. Influent nTiO₂ concentration = 100 mg/L

and background solution = 1 mM NaCl. Data is expressed as mean \pm standard deviation of duplicate measurement.

At pH 5 and 9, the influent HDD of nTiO₂ was much larger than that of single nanoparticle (~20 nm) (Fig. 9-e & 9-f), attributable to aggregation. This implies that size exclusion and straining could potentially influence nTiO₂ transport. The HDD did not considerably vary at pH 5, comparing the influent and effluent HDD in each experiment and between the experiments. At pH 9, the effluent HDD decreased with respect to that of the influent, although the effluent HDD were similar across experiments. It is worth mentioning that the effluent HDD is consistently larger for the pH 5 experiments compared to those for the pH 9 experiments because the influent HDD for the pH 5 experiments is larger than that for the pH 9 experiments, due to a lower zeta potential magnitude at pH.

4.3.2.1. nTiO₂ transport and retention mechanisms at pH = 5

At pH 5, for different medium type, the shape of the BTC was all similar, i.e., each BTC started with an initial sharp increase (maximum $C/C_0 = 0.12\text{--}0.18$) until ~1 PV, followed by a gradual concentration decrease (Fig. 8-a). In the quartz sand–sediment experiment, the low mobility of nTiO₂ ($C/C_0 \leq 0.15$ and mass recovery ~11%) (Fig. 8-a & Table S3, SI) was attributable to the attractive electrostatic forces between positively charged nTiO₂ and negatively charged surfaces of quartz sand and the sediment (Fig. 10-a).

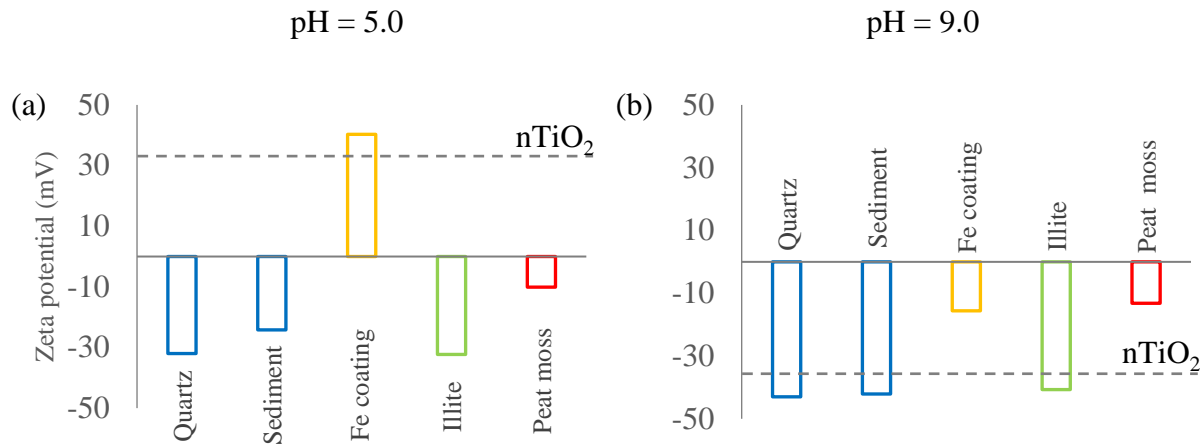


Fig. 10. Zeta potential of various types of collector surface (bars) and nTiO₂ (dashed lines) at pH 5.0 and 9.0. The zeta potential of quartz sand, illite, Fe oxyhydroxide coating, and peat moss were based on previous studies (Rastghalam et al., 2018; Wu and Cheng, 2016; and Zhou and Cheng, 2018). The zeta potential of sediment and nTiO₂ was measured in this study.

Effluent pH of the quartz sand–sediment column was 6.0 (Fig. 9-a), higher than that of the influent, indicating pH increased in the column, presumably due to pH buffering by the transport media. Although the column was flushed with the nTiO₂-free background solution with pH and background electrolyte matching those of the influent suspension for 16 hours before nTiO₂ injection, protonation on the surface of the medium did not seem to reach its capacity throughout the column since we still observed the difference in influent and effluent pH during the injection period (Fig. S13-a & S13-b, SI). Therefore, as the nTiO₂ moved along the column, its zeta potential was expected to become less positive. It is interesting to note, however, that the effluent zeta potential was negative (-26 mV) (Fig. 9-c), notwithstanding the effluent pH of 6.0, which was lower than the p*H*_{pzc} of nTiO₂ (~6.8) (Fig. 9-a). The negative zeta potential presumably was the result of DOC adsorption to nTiO₂. Partial dissolution of the natural organic matter in the sediment (SOC = 5.8 mg/g) could release dissolved organic carbon to the pore water. Our measurements

confirmed the presence of DOC in different columns' effluent (Fig. S14, SI). Positively charged nTiO₂ have a high affinity for negatively charged DOC (Wu and Cheng, 2016), and therefore DOC in the pore water could adsorb to the particles and change particle zeta potential. Similar results have been reported previously (Fisher-Power and Cheng, 2018; Zhou and Cheng, 2018), demonstrating the importance of SOM in mediating the surface charge and mobility of positively-charged ENPs in acidic water. It is worth noting that nano-size or small-size clay colloids, together with DOC, could also attach to nTiO₂ and decrease the overall zeta potential. However, as shown in Fig. 9-c, nTiO₂ zeta potential reversed at pH 5 after nTiO₂ passed through the column. Based on the authors' previous paper (Rastghalam et al., 2019), illite clay (even at high concentration of 10 mg/L) did not reverse the zeta potential of nTiO₂. Therefore, it is more likely that the decrease in zeta potential observed in this current study was caused by DOC (Fig. S14, SI). Due to the pH change along the flow path in the column and the effect of DOC on zeta potential, Fig. 10 cannot fully represent the nTiO₂-medium interactions. To better illustrate the mechanisms that governed nTiO₂ retention, the electrostatic interactions between nTiO₂ and each component were plotted (Fig. S15-a & S15-c). For the pH 5 experiments, pore water pH ranged from 5.0–6.0, and therefore both the sediment and quartz carried negative charges, whereas the nTiO₂ were expected to carry positive charge when the DOC effect was not considered (Fig. S15-a). Even though, the spatial distribution of zeta potential of the nTiO₂ along the flow path of the column is not known, based on the zeta potential measurement of the influent and the effluent (Fig. 9-c), we conclude that a small percentage of the originally positively charged nTiO₂ became negatively charged after passing through the column. Furthermore, our DLVO calculation confirmed substantial energy barriers between the effluent nTiO₂ and negatively charged collector surfaces (Fig. S16-b, SI), which is the very reason why these particles could pass through the column. At the same time, the

low nTiO₂ recovery from the effluent in the pH 5 experiments (Fig. 8-a) showed high deposition, attributable to the electrostatic attraction between the positively charged nTiO₂ and collector surfaces (Fig. S16-a, SI). Taken together, we concluded that a small percentage of the particles gained sufficient negative charges while the majority of the particles were retained in the columns by electrostatic attraction, even though it is not clear if the change in zeta potential took place near the inlet, outlet, or gradually along the flow path of the column. The effluent nTiO₂ concentration for the Fe oxyhydroxide-coated sand–sediment experiment was slightly higher ($C/C_0 \leq 0.18$ and mass recovery ~13 %) than that of the quartz sand–sediment column (Fig. 8-a & Table S3, SI), indicating that the Fe oxyhydroxide coating decreased particle retention. As shown in Fig. 10-a, the Fe oxyhydroxide coating was positively charged at pH 5, and therefore the patch-wise coating could repel the like-charged nTiO₂ and reduced particle retention, resulting in a minor delay in reaching the highest effluent nTiO₂ concentration compared to that of the quartz sand–sediment column. It is worth noting that the Fe oxyhydroxide was present in all the treatments due to the sediment used in the columns and its impact on nTiO₂ transport under a certain condition was similar to what has been previously described for the Fe oxyhydroxide coating at pH 5 and 9. However, since the amount of Fe oxyhydroxides from the sediment is identical for all the experiments, we considered it as a common factor having the same effect on nTiO₂ transport in all the treatments.

The BTC of the quartz sand–sediment–illite experiment was almost identical to the BTC of the quartz sand–sediment experiment (Fig. 8-a), indicating that illite clays did not notably influence nTiO₂ transport. Previous studies found that under unfavorable deposition conditions, fine-sized clay minerals in columns either decreased or increased the transport of negatively charged ENPs due to physical entrapment or stronger negative charges of the clay minerals (Bayat

et al., 2015; Jung et al., 2014). These effects were not observed in our experiment, since in our experiment particle deposition was under favorable condition, i.e., the quartz sand, sediment, and illite were all negatively charged throughout the column (Fig. S15-a), and the strong electrostatic attractive forces between the medium surface and positively-charged nTiO₂ dominated particle retention.

For the quartz sand–sediment–peat moss column, the quartz sand, sediment, and peat moss were all negatively charged at pH = 5.0 (Fig. 10-a), therefore the positively charged nTiO₂ was attracted to the medium upon entering the column (Fig. S15-a & Fig. S16), explaining the low mobility of nTiO₂ (Fig. 8-a & Table S3, SI). Among all the columns at pH 5, the quartz sand–sediment–peat moss column showed the highest effluent concentration and mass recovery ($C/C_0 \leq 0.18$ and mass recovery ~15%) (Fig. 8-a & Table S3, SI). The higher mobility in this column was most likely caused by the higher DOC concentration (Fig. S14, SI). Similar to the NOM in the sediment, the peat moss is organic-rich and releases DOC to pore water (Zhou and Cheng, 2018). Hence, the peat moss in the column could increase DOC concentration in the pore water. In turn, the higher DOC concentration led to higher DOC adsorption to the nTiO₂ (as well as the Fe oxyhydroxide in the sediment), which intensified the negative charges and the electrostatic/steric repulsions between nTiO₂ and the medium, causing higher mobility.

For all the pH 5 experiments, decrease in effluent nTiO₂ concentration during particle injection after ~1 PV was observed (Fig. 8-a). Similar results were previously reported and explained by ripening, i.e., incoming particles were attracted to the particles already deposited, resulting in higher particle retention and lower effluent concentration (Fisher-Power and Cheng, 2018). In our experiments, the nTiO₂ that were positively charged and previously retained on the medium could attract those incoming nTiO₂ particles that were negatively charged due to DOC adsorption.

According to the DLVO profiles (Fig. S16, SI), the influent nTiO₂ particle, which carried positive charge, can attach to the quartz, illite, and peat moss. Conversely, there were energy barriers between the negatively charged effluent nTiO₂ and the collectors, indicating that collectors' surface was not responsible for the increased particle retention. A fraction of the Fe oxyhydroxide coating which was not covered by the DOC may repel the positively charged nTiO₂ particle and adsorb those negatively charged nTiO₂ particles. However, the shape of BTCs suggests that the ripening (i.e., increased deposition over time) was the dominant mechanism.

4.3.2.2. nTiO₂ transport and retention mechanisms at pH = 9

With influent pH = 9, no retardation was observed for nTiO₂ breakthrough from the quartz sand–sediment column (Fig. 8-b). Effluent nTiO₂ concentration rapidly increased to a plateau of $C/C_0 = 0.99$ at ~1 PV and mass recovery from the effluent was 95% (Table S3, SI). At pH 9, the quartz sand, sediment, and nTiO₂ were all negatively charged near the influent side (Fig. 10-b), resulting in repulsive electrostatic forces between the nTiO₂ and medium surfaces (Fig. S15-b, upper diagram), consistent with the high mobility observed. However, on the effluent side, due to pH buffering by the medium materials, the pH decreased to 6.3, lower than the pH_{PZC} of nTiO₂ (Fig. 9-b). Therefore, nTiO₂ could carry positive charge near the effluent side and be retained by the negatively charged medium via electrostatic attraction (Fig. S15-b, lower diagram). This contradicts the high mobility observed. To reconcile the discrepancy, the effect of DOC needs to be considered. It was found that the effluent zeta potential was negative (Fig. 9-d) despite the lower pH (Fig. 9-b), which was attributable to DOC adsorption as previously discussed. Hence, even near the effluent side of the column where pH was lower than the pH_{PZC} of nTiO₂, the nTiO₂ were still negatively charged and repelled by the like-charged quartz sand and sediment components. It should also be noted that the effluent pH was below the pH_{PZC} of Fe oxyhydroxide (~8.4), which

could make the Fe oxyhydroxide (in the sediment) near the column effluent side positively charged and attract the negatively charged nTiO₂. However, the observed high mobility of nTiO₂ suggested that the Fe oxyhydroxide did not have a strong effect, presumably due to DOC adsorption to the Fe oxyhydroxide. As previously discussed, partial dissolution of the SOC in the sediment released DOC, which could adsorb to the Fe oxyhydroxides and make the mineral surface negatively charged (Fig. S15-d).

The BTC of the Fe oxyhydroxide-coated sand–sediment column was very similar to that of the quartz sand–sediment column (Fig. 8-b), except that nTiO₂ breakthrough was slightly delayed in the presence of the Fe oxyhydroxide coating, with C/C₀ reaching a plateau of 0.98 at ~3 PV and a mass recovery of 93% (Table S3, SI). The zeta potentials of quartz, sediment, and Fe oxyhydroxide were all negative at pH 9.0 (Fig. 10-b), representing the conditions near the influent side of the Fe oxyhydroxide-coated sand–sediment column, where negatively charged nTiO₂ was repelled by the medium. The pH decreased to ~6.1 (Fig. 9-b) as measured in the effluent, lower than the p*H*_{pzc} of Fe oxyhydroxide, suggesting Fe oxyhydroxide could carry positive charges. However, as discussed for the quartz sand–sediment column, DOC in the pore water could adsorb to the Fe oxyhydroxide and reverse its zeta potential. Due to the extra mass of Fe oxyhydroxide (0.01 g as Fe) in the Fe oxyhydroxide-coated sand–sediment column, the positive charges of the Fe oxyhydroxide were not fully neutralized/reversed, and therefore a small fraction of the Fe oxyhydroxide could carry positive charge and attract the negatively charged nTiO₂ (Fig. 9-d), resulting in minor delay in nTiO₂ transport.

With quartz sand–sediment–illite as the transport medium, nTiO₂ breakthrough was substantially delayed in comparison to that of the quartz sand–sediment column (Fig. 8-b). For the quartz sand–sediment–illite column, the full breakthrough was not reached until 4 PV and the

mass recovery was lower than that of the quartz sand–sediment column (82% vs. 95%) (Table S3, SI). Within the pH range of the quartz sand–sediment–illite column (6.2–9.0) (Fig. 9-b), illite clays were negatively charged (Fig. 10). Additionally, as discussed previously, the nTiO₂ were negatively charged throughout the column due to high pH and/or DOC adsorption. As such, the illite clays were expected to repel the like-charged nTiO₂, which did not explain the lower mobility in the presence of illite. The lower mobility was presumably caused by straining, which happens when flow paths are too narrow for particles to pass or when medium grains are irregular in shape or have unsmooth surface (i.e., surface structures) that can physically entrap particles (Auset and Keller, 2006; Bradford et al., 2005; Chowdhury et al., 2011). In our experiment, with the presence of illite clays in the column, several mechanisms could promote straining. First was the smaller grain size of the illite clay ($d_{50} = 150 \pm 26 \mu\text{m}$ for illite vs. $d_{50} = 212 \pm 36 \mu\text{m}$ for the sediment and $d = 600\text{--}700 \mu\text{m}$ for the quartz sand) (Fig. S10 & S11, SI), which caused smaller pore space and narrower flow paths. Previous studies confirmed that for porous media with polydispersed grains, the amount of strained particles was positively correlated to the amount of fine-sized grains (e.g., grains < 150 μm) in the medium (Fang et al., 2009; Shani et al., 2008). The difference in the particle-to-grain diameter ratio (d_p/d_c , where d_p and d_c are the diameters of the nTiO₂ and clay, respectively) of the influent and effluent also suggested straining. For the influent, $d_p/d_c = 2.2 \times 10^{-3}$, greater than the cutoff value of 2.0×10^{-3} , at which straining occurs (Auset and Keller, 2006; Chowdhury et al., 2011; Xu et al., 2006). While for the effluent, the particles were too small to be strained ($d_p/d_c = 1.3 \times 10^{-3}$ to 1.6×10^{-3}). Additionally, in our experiment, the wider range of grain size as a result of illite addition to the column also helped create narrower flow paths, since the smaller grains tend to occupy the pore space between larger grains (Fetter, 2001). Furthermore, the fibrous structure of the illite clay provided sites for nTiO₂ entrapment (Bayat et al., 2015). At

both pH 5 and 9, illite clay could increase straining. However, the straining effect was only obvious at pH 9, where the effluent nTiO₂ concentrations were high due to the unfavorable deposition condition and straining was the dominant mechanism that hindered nTiO₂ transport. At pH 5, the nTiO₂ deposition was under favorable condition as a result of strong electrostatic attraction, which made the effect of straining negligible.

The BTC of the column containing quartz sand–sediment–peat moss showed an even slower increase in nTiO₂ concentration ($C/C_0 = 0.99$ at ~6 PV) with a 73% mass recovery (Fig. 8-b & Table S3, SI). Near the influent side of the column where pH was close to the influent pH of 9.0, all the medium components were negatively charged, with the peat moss having a less negative zeta potential (-13.2 mV) compared to the quartz sand (-32 mV) and the sediment (-24 mV) (Fig. 10-b). Near the effluent side of the column, where pH was close to the effluent pH of 6.0, all these components were also expected to carry negative charges, considering their negative charges at pH 5 (Fig. 10-a). Additionally, the nTiO₂ carried negative charge throughout the column due to high pH and/or DOC adsorption. Therefore, according to the electrostatic repulsions between nTiO₂ and medium surfaces, fast release of nTiO₂ from the column was expected, which was inconsistent with the delayed breakthrough actually observed (Fig. 8-b). The delay in nTiO₂ breakthrough was attributed to the less negative charges of the peat moss (compared to the quartz sand and the sediment) (Fig. 10), coupled with the irregular shape and surface roughness of the peat moss. The DLVO calculations indicated that although at pH 9 nTiO₂ and peat moss were negatively charged, the energy barrier between nTiO₂ and peat moss was low (~6.0 k_BT) (Fig. S17-d, SI). In addition, the irregular shape and surface roughness of peat moss could further reduce the energy barrier so that nTiO₂ could overcome the energy barrier and deposit via primary minimum. (Shen et al., 2012; Wu and Cheng, 2016; Zhou and Cheng, 2018). Moreover, the

irregular shape of the peat moss provided sites for particle entrapment, and the addition of peat moss to the column caused larger disparity in grain size, which in turn facilitated straining (as discussed for the quartz sand–sediment–illite experiment). The effect of roughness was more pronounced at pH 9 compared to that at pH 5, since under unfavorable deposition conditions, other mechanisms, including electrostatic interactions had no/minimum effect on nTiO₂ transport.

4.4. Conclusions

In a geochemically heterogeneous medium, NOM, Fe oxyhydroxide coating, and illite clays may significantly influence the retention and transport of nTiO₂, and pH was found a key factor that governs the nature of such influence. NOM, Fe oxyhydroxide coating, and illite clays were found to play distinct roles under similar mineralogical, water chemistry, and hydrological conditions. While the Fe oxyhydroxide coating increased the transport of positively-charged nTiO₂ in the pH 5 experiment via electrostatic repulsion, the coating decreased transport in the pH 9 experiment, attributable to the electrostatic attraction caused by pH buffering and/or DOC adsorption. Illite clay did not affect nTiO₂ transport in the pH 5 experiment since electrostatic attraction dominated particle retention, whereas illite caused a notable delay in nTiO₂ transport in the pH 9 experiment due to straining and entrapment despite unfavorable deposition conditions. The effect of peat moss was also pH dependent. In the pH 5 experiment, peat moss enhanced nTiO₂ transport by releasing DOC, which reversed the zeta potential of the positively-charged nTiO₂ and facilitated particle transport through a mainly negatively-charged medium. While in the pH 9 experiment, peat moss hindered transport via multiple mechanisms. Less negative zeta potential of the peat moss in comparison to that of quartz and the sediment, as well as surface roughness of the peat moss, reduced energy barrier. Additionally, the larger disparity in grain size in the presence of peat moss and the irregular shape of the peat moss facilitated straining and entrapment.

All these factors helped increase particle retention. In summary, this study demonstrated that in a geochemically heterogeneous medium, NOM, Fe oxyhydroxides, and clay minerals could affect nTiO₂ retention and transport through the combined effect of various processes, which include electrostatic interaction, straining and entrapment, and changing of pH and DOC concentration in pore water. Overall, the low mobility of nTiO₂ in acidic soils/sediment observed in this study suggests a low risk of nTiO₂ transport into nearby sites and eventually the groundwater. The results demonstrated that at low pH electrostatic attraction had a substantial effect on nTiO₂ transport that dominated the effect of other mechanisms. Conversely, nTiO₂ mobility can be significant through alkaline soil/sediment and sensitive to the soil/sediment minerals and organic matter content. These findings are important to understand the behaviour of nTiO₂ in natural subsurface environments where various soil/sediment components co-exist. Further research on the effect of ionic strength, clay mineral type, and various dissolved anions and cations will be beneficial to the understanding of the fate and transport of nTiO₂ in the natural environment.

Acknowledgments

This work was supported by Natural Sciences and Engineering Research Council of Canada's Discovery Grant (No. 402815-2012) and Canada Foundation for Innovation's Leaders Opportunity Fund (No. 31836).

Appendix 3. Supplementary data

Supplementary material related to this chapter can be found, in the Appendices. All the original data are provided in electronic format.

Chapter 5. Summary

With the development and application of nanotechnology, there has been a rising demand to evaluate the potential risks derived from nanomaterials. Whether the nanoparticles will travel long distances or attach to the porous media determines their adverse effect on the environment. The effect of solution chemistry and porous media on nanoparticle mobility has been shown by numerous studies. However, more investigations are needed to comprehend and predict the behavior of nanoparticles in natural water systems, due to the complex water chemistry and properties of the media through which nanoparticles travel. The results of this research illustrated that the fate and transport of nTiO₂ in aquatic systems are under the influence of a combination of different factors and mechanisms arising from various water chemistry and porous media conditions.

In Chapter 2, it was demonstrated that the nTiO₂ aggregation and attachment to quartz sand was strongly influenced by the interactions among nTiO₂, phosphate and major dissolved cations (e.g., Na and Ca²⁺), depending on the pH and valency of the major cation involved. The nTiO₂ attachment to quartz sand in an NaCl solution was governed by electrostatic interactions. In a CaCl₂ solution, the nTiO₂ attachment to quartz sand was high due to the electrostatic attraction between nTiO₂ and quartz sand at pH 5 and ripening at pH 9. The phosphate adsorption to nTiO₂ was under the effect of electrostatic interactions in the NaCl solution, while precipitation, in addition to electrostatic interactions, contributed to phosphate adsorption to nTiO₂ in the presence of Ca²⁺. Moreover, this study showed that the attachment of illite colloid to quartz sand can be much less sensitive to water chemistry changes compared to that of nTiO₂.

From Chapter 3 it can be concluded that nTiO₂ aggregation and transport were affected by the co-presence of dissolved phosphate, suspended illite colloids, and Fe oxyhydroxide coating on

quartz sand. The nature of this influence was strongly pH dependent and governed by the interactions between nTiO₂, dissolved phosphate, suspended illite colloids, and Fe oxyhydroxide coating. Fe oxyhydroxide coating was found to increase nTiO₂ transport at pH 5 via electrostatic repulsion, whereas illite colloid was found to attract and entrap nTiO₂ and hence reduce its transport. Dissolved phosphate at pH 5 had high affinity for nTiO₂ and served as bridges between nTiO₂ particles, resulting in large aggregates, which were immobilized due to physical straining. At pH 9, neither illite colloid nor phosphate influenced nTiO₂ aggregation or transport in quartz sand since all the particle and media surfaces carried negative charges and repelled each other. However, at pH 9, Fe oxyhydroxide coating decreased $pH_{\text{porewater}}$ to the range between the pH_{pzc} of nTiO₂ and Fe oxyhydroxide and thus made the Fe oxyhydroxide and nTiO₂ oppositely charged, which inhibited nTiO₂ transport. The presence of phosphate and illite colloid enhanced nTiO₂ transport in Fe oxyhydroxide-coated sand, as they competed against nTiO₂ for deposition sites on the positively-charged Fe oxyhydroxide coating and reduced nTiO₂ retention.

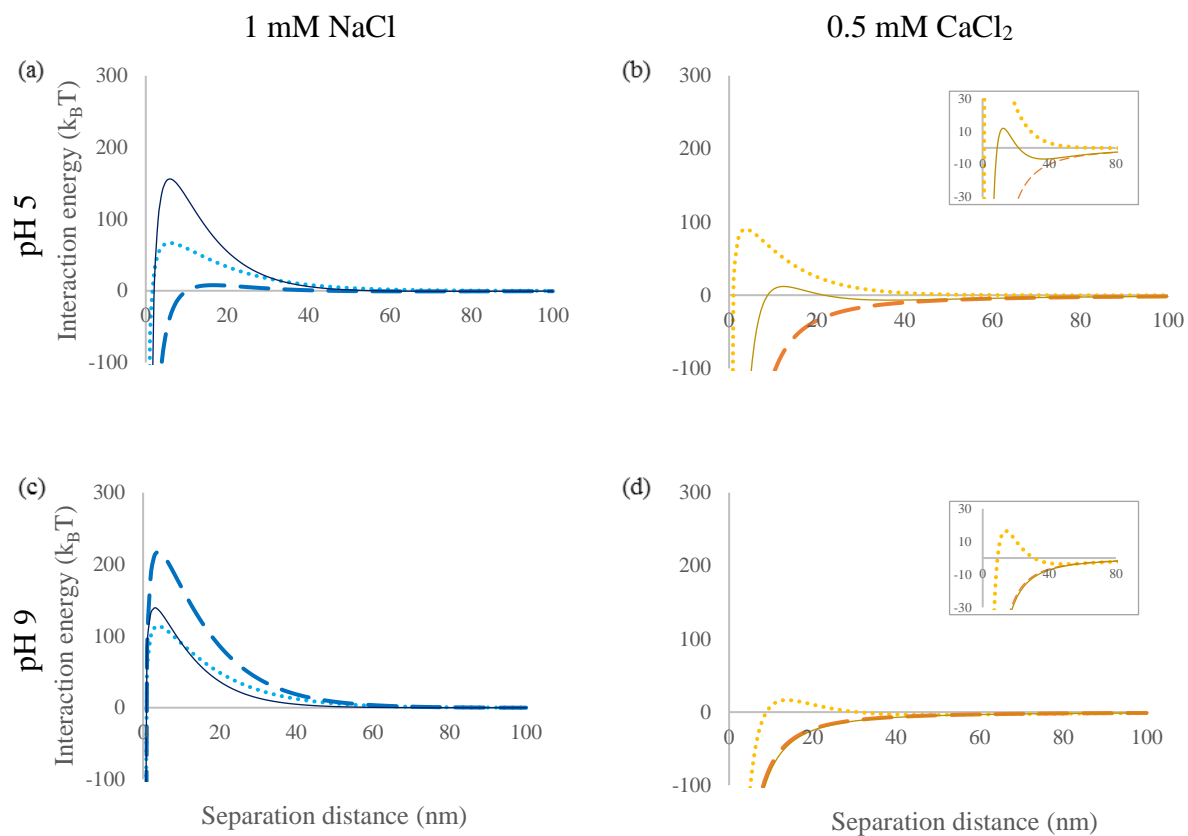
Chapter 4 showed that under similar mineralogical, water chemistry, and hydrological conditions, NOM, Fe oxyhydroxide coating, and illite clays could have crucial and distinct influence on nTiO₂ transport, and pH determined the nature of such influence. At pH 5, Fe oxyhydroxide coating increased nTiO₂ transport due to electrostatic repulsion, but slightly decreased the nTiO₂ mobility at pH 9, attributable to the electrostatic attraction between oppositely-charged nTiO₂ and the coating (caused by pH buffering and/or DOC adsorption). At pH 5, illite clay did not affect nTiO₂ transport due to the domination of electrostatic attraction, whereas at pH 9 illite increased the straining and entrapment, resulting in a notable reduction in nTiO₂ transport. Peat moss enhanced nTiO₂ transport at pH 5 by releasing DOC, whereas at pH 9, peat moss hindered nTiO₂ transport due to surface roughness and straining effect of the peat moss.

In summary, this study demonstrated that nanoparticle transport in a geochemically heterogeneous medium is governed by synergic effect of various factors and different processes which include electrostatic interaction, straining, blocking, ripening, entrapment, and changing of pH and DOC concentration in pore water. Our findings suggest that the combined effect of various water chemistry conditions (e.g., pH, dissolved cations, and anions), and mineralogical/organic composition of the transport medium are important considerations when evaluating nanoparticle transport in the natural environment. Findings from this thesis illuminated some of the geochemical reactions that need to be considered when evaluating the behaviours of engineered nanomaterials under complex physicochemical conditions.

Additional investigations on important factors and mechanisms affecting the fate and transport of nanoparticles are required due to the complexity of the processes involved. Examples of future research include: (1) investigating the effect of complex physicochemical conditions, including varying ionic strength, mixed types of cations/anions, different types of clay minerals/organic matter; (2) extension of the DLVO theory to better predict the interaction forces between particles-particle or particle-porous media (considering the heterogeneity of porous media) (2) development and application of more accurate analytical instruments and methods to detect and monitor ENPs; (3) conducting field studies and using intact columns to determine the fate and transport of ENPs in the vadose zone and groundwater; and (4) extension of mathematical models that can better predict the retention and transport of ENPs, especially in natural soil/sediment.

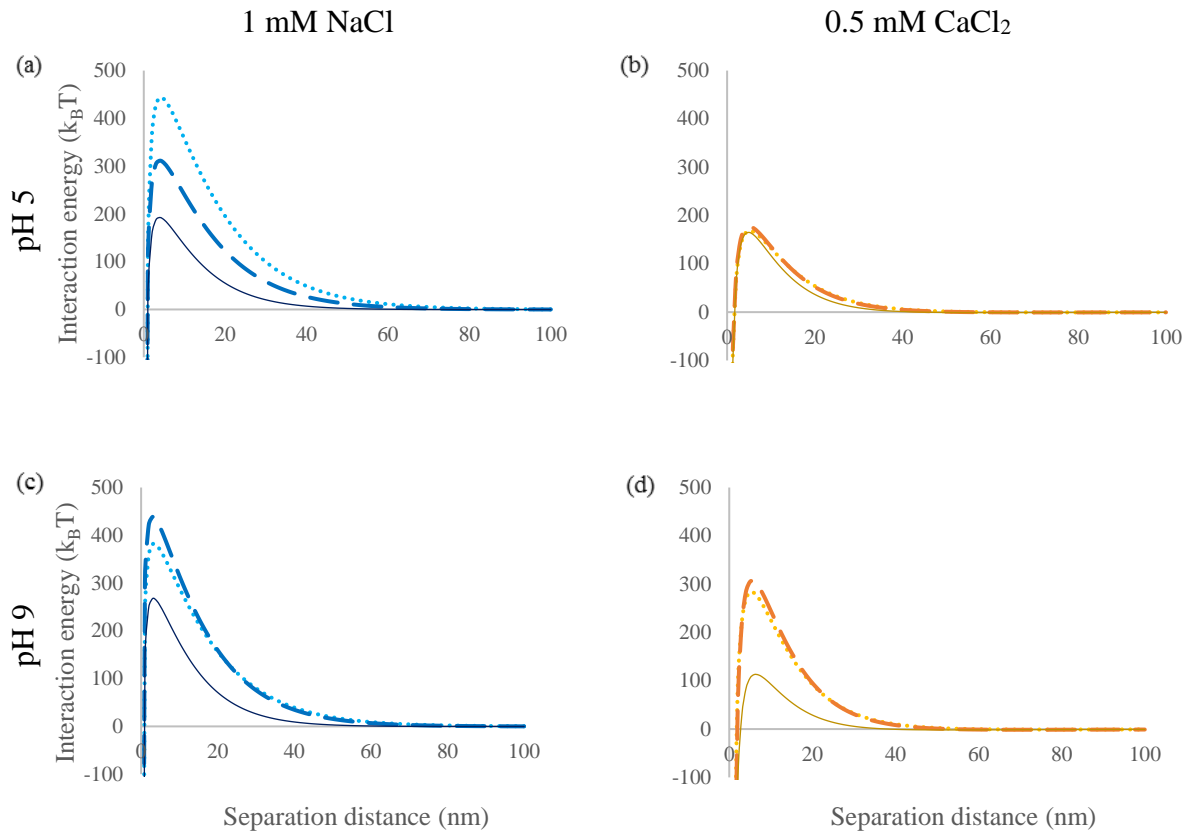
Appendices

Appendix 1. Supporting Information for Chapter 2



Dotted line: $P = 0$; long dash line: $P = 2$ mg/L; solid line: $P = 10$ mg/L. P is total phosphate concentration.

Fig. S1. Interaction energy vs. separation distance between nTiO₂ particles in 1 mM NaCl solution (a, c) and 0.5 mM CaCl₂ solution (b, d) at pH 5 (a, b) and pH 9 (c, d).



Dotted line: $P = 0$; long dash line: $P = 2$ mg/L; solid line: $P = 10$ mg/L. P is total phosphate concentration.

Fig. S2. Interaction energy vs. separation distance between illite particles in 1 mM NaCl solution (a, c) and 0.5 mM CaCl₂ solution (b, d) at pH 5 (a, b) and pH 9 (c, d).

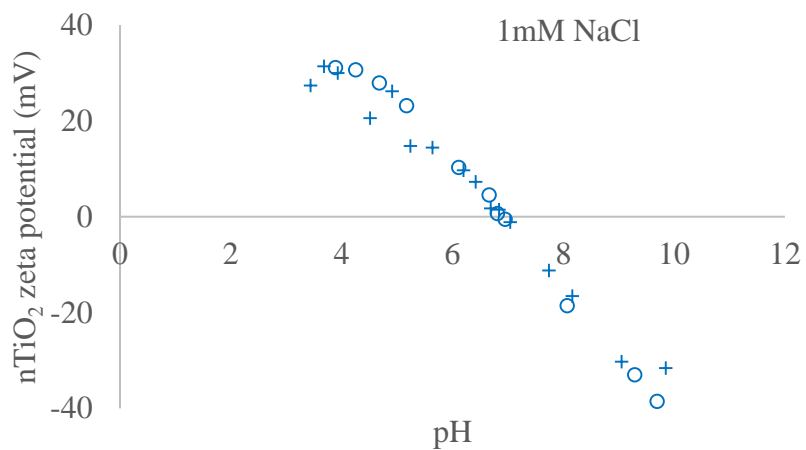
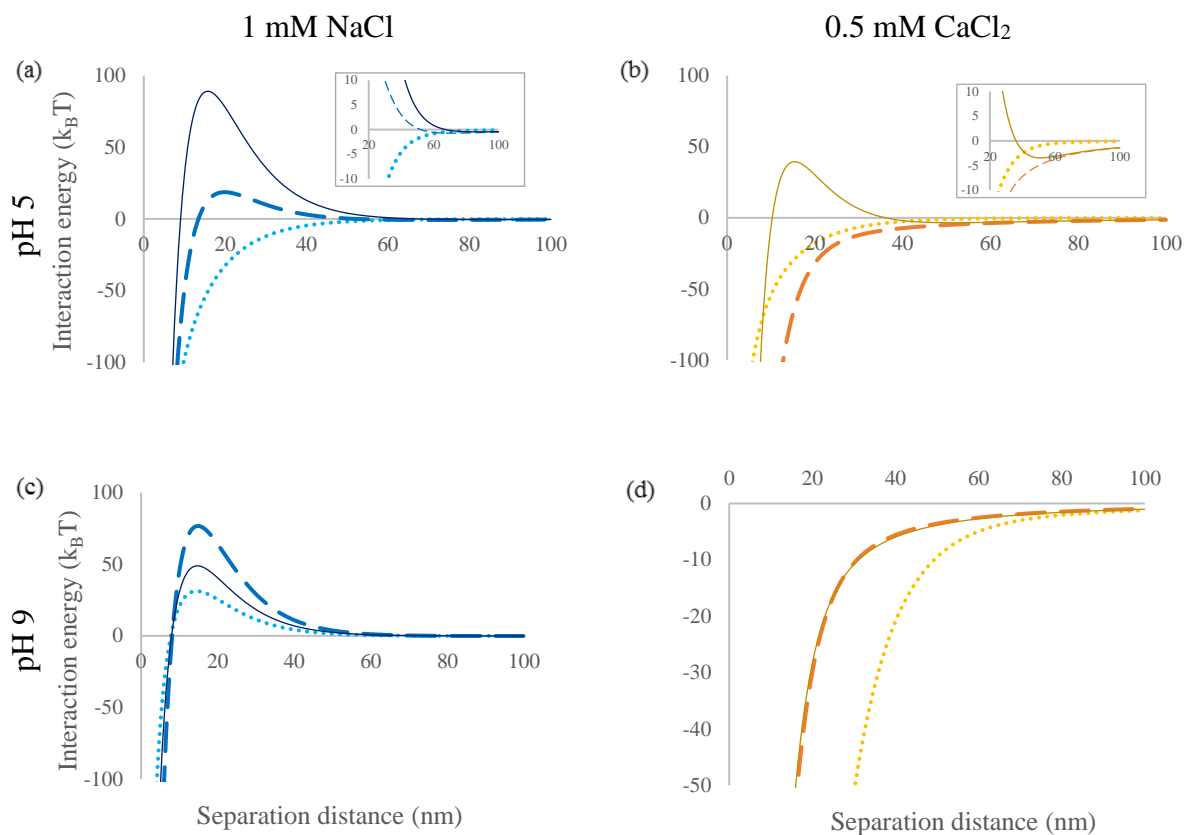
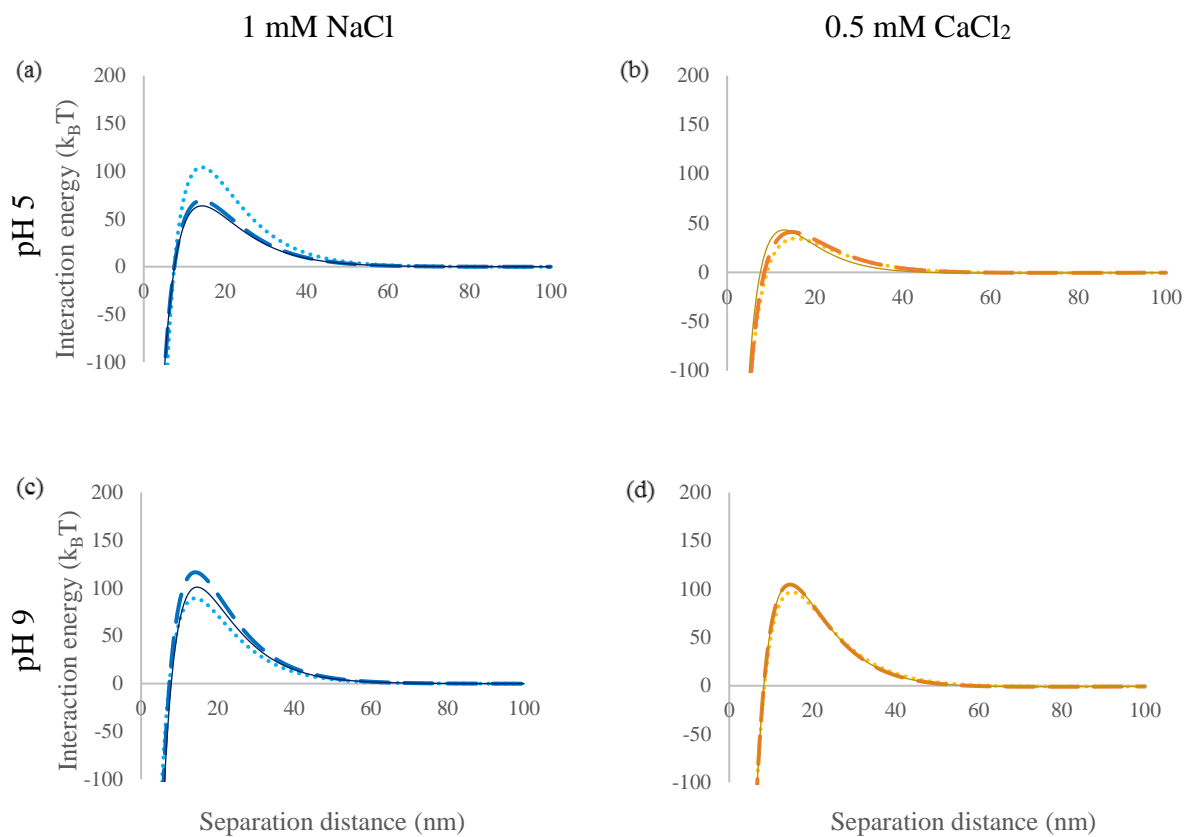


Fig. S3. Zeta potential of nTiO₂ as a function of pH in phosphate-free 1 mM NaCl solution. Point of zero charge (pHPZC) ~ 6.8. The circles and crosses indicate results from two replicate experiments.



Dotted line: $P = 0$; long dash line: $P = 2$ mg/L; solid line: $P = 10$ mg/L. P is total phosphate concentration.

Fig. S4. Interaction energy vs. separation distance between nTiO₂ and quartz sand in 1 mM NaCl solution (a, c) and 0.5 mM CaCl₂ solution (b, d) at pH 5 (a, b) and pH 9 (c, d).



Dotted line: $P = 0$; long dash line: $P = 2$ mg/L; solid line: $P = 10$ mg/L. P is total phosphate concentration.

Fig. S5. Interaction energy vs. separation distance between illite colloid and quartz sand in 1 mM NaCl solution (a, c) and 0.5 mM CaCl₂ solution (b, d) at pH 5 (a, b) and pH 9 (c, d).

Appendix 2. Supporting Information for Chapter 3

1. Additional materials and methods

1.1. DLVO calculations

Interactions between two similar particles (e.g., nTiO₂ to nTiO₂ or illite to illite) (Gregory, 1981; Hogg et al., 1966; Sun et al., 2015b):

$$\Phi_{LW} = -\frac{A r_p}{12D} \left[1 + \frac{14D}{\lambda}\right]^{-1} \quad (S1)$$

$$\Phi_{EDL} = 2\pi \varepsilon_0 \varepsilon_r r_p \psi_p^2 \ln [1 + \exp(-\kappa D)] \quad (S2)$$

Interactions between two dissimilar particles (e.g., nTiO₂ to illite) (Chen et al., 2011; Gregory, 1981; Hogg et al., 1966; Tang and Cheng, 2018):

$$\Phi_{LW} = -\frac{A r_{p1} r_{p2}}{6D (r_{p1} + r_{p2})} \left[1 - \frac{5.32 D}{\lambda} \ln \left(1 + \frac{\lambda}{5.32 D}\right)\right]^{-1} \quad (S3)$$

$$\Phi_{EDL} = \frac{\varepsilon_0 \varepsilon_r r_{p1} r_{p2}}{4(r_{p1} + r_{p2})} (\psi_{p1}^2 + \psi_{p2}^2) \left\{ \frac{2 \psi_{p1} \psi_{p2}}{\psi_{p1}^2 + \psi_{p2}^2} \ln \left[\frac{1 + \exp(-\kappa D)}{1 - \exp(-\kappa D)} \right] + \ln [1 - \exp(-2\kappa D)] \right\} \quad (S4)$$

Interactions between particle (e.g., nTiO₂ or illite particles) and collector surface (Gregory, 1981; Hogg et al., 1966; Sun et al., 2015b):

$$\Phi_{LW} = -\frac{A r_p}{6D} \left[1 + \frac{14D}{\lambda}\right]^{-1} \quad (S5)$$

$$\Phi_{EDL} = \pi \varepsilon_0 \varepsilon_r r_p \left\{ 2\psi_p \psi_s \ln \left[\frac{1 + \exp(-\kappa D)}{1 - \exp(-\kappa D)} \right] + (\psi_p^2 + \psi_s^2) \ln [1 - \exp(-2\kappa D)] \right\} \quad (S6)$$

where A is Hamaker constant, r_p (or r_{p1} and r_{p2}) refers to radius of the particle, D is separation distance, and λ is characteristic wavelength of interaction, usually taken to be 100 nm (Elimelech et al., 1995). ε_0 ($8.85 \times 10^{-12} \text{ C}^2 \text{ J}^{-1} \text{ m}^{-1}$) is permittivity of vacuum, ε_r (80) is relative dielectric constant of the medium, k_B is Boltzmann constant ($1.38 \times 10^{-23} \text{ m}^2 \text{ kg s}^{-2} \text{ K}^{-1}$), T is absolute temperature (K) of the system, ψ_p (or ψ_{p1} and ψ_{p2}) (V) and ψ_c are zeta potential of particle and collector surface, n_∞ (m^{-3}) is number concentrations of the bulk ions in bulk solution, and κ

(m^{-1}) is Debye–Hückel reciprocal length and can be calculated using Equation (S7) (Chen et al., 2011).

$$\kappa = \sqrt{\left(\frac{e^2 \sum n_{i0} z_i^2}{\epsilon_0 \epsilon_r k_B T}\right)} \quad (S7)$$

where e is electron charge (1.602×10^{-19} coulombs), n_{i0} is number concentration of ion i in bulk solution (m^{-3}), z_i is valence of ion i in bulk solution.

Hamaker constant (A) values for the interactions of two dissimilar materials (1 and 2) via a third media (3) was calculated by Equation (S8) (Hiemenz and Rajagopalan, 1997) or obtained from previous studies (Table S1).

$$A_{132} = (\sqrt{A_{11}} - \sqrt{A_{33}})(\sqrt{A_{22}} - \sqrt{A_{33}}) \quad (S8)$$

$nTiO_2$ and illite colloids were assumed to exist as individual particles in all mixed suspensions except for the $nTiO_2$ –illite experiment at pH 5. Under this circumstance, zeta potential and HDD measurements reflected the mean properties of 3 dissimilar particles ($nTiO_2$, illite colloid, and $nTiO_2$ –illite aggregate) and, therefore, the properties of the individual particles (i.e., $nTiO_2$ and illite colloid) and the aggregates ($nTiO_2$ –illite) could not be distinguished. Hence, DLVO calculation between $nTiO_2$ –illite particles and collector surfaces in this treatment was not performed.

Table S1. Hamaker constant applied in DLVO calculations.

Materials	Hamaker constant ($\times 10^{-20}$ J)	References
nTiO ₂ -H ₂ O-nTiO ₂	3.5	Gómez-Merino et al. (Gómez-Merino et al., 2007)
illite-H ₂ O-illite	2.2	Long et al. (Long et al., 2006)
nTiO ₂ -H ₂ O-illite	2.0	Calculated using Equation S8
nTiO ₂ -H ₂ O-SiO ₂	1.4	Butt et al. (Butt et al., 2005); Petosa et al. (Petosa et al., 2010)
illite-H ₂ O-SiO ₂	0.6	Calculated using Equation S8
nTiO ₂ -H ₂ O-FeOx	12.6	Wu and Cheng (Wu and Cheng, 2016)
illite-H ₂ O-FeOx	6.4	Calculated using Equation S8
nTiO ₂ -nTiO ₂	15.3	Bergström (Bergström, 1997)
illite-illite	8.6	Médout-Marère (Médout-Marère, 2000)
H ₂ O-H ₂ O	3.7	Israelachvili (Israelachvili, 2011)
SiO ₂ -SiO ₂	6.5	Hough and White (Hough and White, 1980)
FeOx-FeOx	68.0	Faure et al. (Faure et al., 2011)

1.2. Modeling nTiO₂ transport

(a) One-site model

A one-dimensional form of the ADE (Advection Dispersion Equation) with one kinetic attachment site was used to simulate the nTiO₂ BTCs:

$$\frac{\partial(\theta C)}{\partial t} = \frac{\partial}{\partial x} \left(\theta D \frac{\partial C}{\partial x} \right) - v \frac{\partial C}{\partial x} - \rho \frac{\partial S}{\partial t} \quad (\text{S9})$$

$$\rho \frac{\partial S}{\partial t} = \theta k_{att} \psi C - \rho k_{det} S \quad (\text{S10})$$

where C is nTiO₂ concentration in the aqueous phase [M L^{-3}], t is the time [T], S is the particle concentration on the solid phase [M M^{-1}], ρ is the bulk density [M L^{-3}], D is the dispersion coefficient [$\text{L}^2 \text{T}^{-1}$], x is the distance from the column inlet [L], v is the pore water velocity [L T^{-1}], θ is the porosity of the quartz sand. k_{att} and k_{det} are the particle attachment and detachment coefficients, respectively (k_{det} was set to zero based on the shape of BTCs). ψ is a dimensionless function to account for both time- and depth-dependent blocking. The expression for the blocking term (ψ) is given as follows:

$$\psi = 1 - \frac{S}{S_{max}} \quad (\text{S11})$$

S_{max} is the maximum solid phase concentration of nanoparticle [M M^{-1}].

(b) Two-site model depending on blocking

A two-site model of the ADE with two sorption sites was used to simulate the blocking BTCs, where $\rho \frac{\partial S}{\partial t}$ in Equation (S9) is given as follows:

$$\rho \frac{\partial S}{\partial t} = \rho \left(\frac{\partial S_e}{\partial t} + \frac{\partial S_k}{\partial t} \right) = \theta k_{1\,att} \psi_1 C - \rho k_{1\,det} S + \theta k_{2\,att} \psi_2 C - \rho k_{2\,det} S \quad (\text{S12})$$

Type-1 sorption sites are rapid adsorption site, type-2 sites are slow adsorption site. $k_{1\,att}$ and $k_{2\,att}$, and $k_{1\,det}$ and $k_{2\,det}$ are the particle attachment and detachment coefficients of two types

of sorption sites, respectively (kI_{det} and kI_{det} were set to zero based on the shape of BTCs). The expression for the blocking term (ψ) is given as follows:

$$\psi_1 = 1 - \frac{S}{S_{1\ max}} \quad (S13)$$

$$\psi_2 = 1 - \frac{S}{S_{2\ max}} \quad (S14)$$

(c) Two-site model depending on both blocking and straining

nTiO₂ transport process within the saturated sand column was described by an ADE model considering reversible and irreversible attachment process. $\rho \frac{\partial S}{\partial t}$ in Equation (S9) is given as follows:

$$\rho \frac{\partial S}{\partial t} = \rho \left(\frac{\partial S_r}{\partial t} + \frac{\partial S_{irr}}{\partial t} \right) = \theta k_{att} \psi_{att} C - \rho k_{det} S + \theta k_{str} \psi_{str} C \quad (S15)$$

S_r and S_{irr} are the “reversibly” and “irreversibly” attached particle concentration [M M⁻¹], respectively. k_{att} and k_{det} (k_{det} was set to zero based on the shape of BTCs) are the particle attachment and detachment coefficients at the reversible sites [T⁻¹], respectively.

$$\psi_{att} = 1 - \frac{S}{S_{max}} \quad (S16)$$

A depth-dependent power law function for ψ_{str} will therefore be utilized:

$$\psi_{str} = \left(\frac{d_c + x}{d_c} \right)^{-\beta} \quad (S17)$$

where d_c is the diameter of the sand grains [L], and β is an empirical factor (with an optimal value of 0.43

2. Additional results

Table S2. Physical and chemical conditions of column transport experiments using 100 mg/L

nTiO₂.

pH	Influent suspension	Illite (mg/L)	Phosphate (mg/L)	Collector	Average flow velocity (cm/h)	Column pore volume (cm ³)	Porosity	Bulk density (g/cm ³)	
5	nTiO ₂	0	0	Quartz sand	32.15±0.71	27.91±0.61	0.38±0.00	1.76±0.01	
				Fe-coated sand	30.80±0.15	28.58±0.14	0.38±0.00	1.74±0.00	
	nTiO ₂ -illite	10	0	Quartz sand	30.27±1.07	28.46±1.04	0.39±0.01	1.74±0.01	
				Fe-coated sand	30.78±0.13	28.79±0.12	0.39±0.00	1.75±0.01	
	nTiO ₂ -phosphate	0	10	Quartz sand	30.86±0.44	28.05±0.83	0.38±0.01	1.75±0.01	
				Fe-coated sand	30.70±0.84	28.23±0.10	0.38±0.01	1.74±0.00	
	nTiO ₂ -phosphate-illite	10	10	Quartz sand	31.21±0.10	28.43±0.18	0.38±0.00	1.74±0.00	
				Fe-coated sand	30.11±0.83	28.85±0.76	0.39±0.01	1.73±0.01	
	9	nTiO ₂	0	0	Quartz sand	30.85±0.29	28.27±0.53	0.38±0.00	1.78±0.02
					Fe-coated sand	30.89±0.23	28.75±0.21	0.39±0.00	1.75±0.01
		nTiO ₂ -illite	10	0	Quartz sand	30.42±0.18	28.79±0.34	0.39±0.00	1.78±0.02
					Fe-coated sand	30.46±0.94	29.65±0.90	0.39±0.00	1.72±0.02
nTiO ₂ -phosphate		0	10	Quartz sand	31.21±0.05	28.30±0.09	0.38±0.00	1.76±0.00	
				Fe-coated sand	30.63±0.39	29.10±0.36	0.39±0.00	1.74±0.01	
nTiO ₂ -phosphate-illite		10	10	Quartz sand	30.63±0.57	28.09±1.09	0.38±0.01	1.74±0.00	
				Fe-coated sand	30.48±0.07	29.03±0.07	0.39±0.00	1.74±0.02	

Data expressed as mean±standard deviation of replicate measurements.

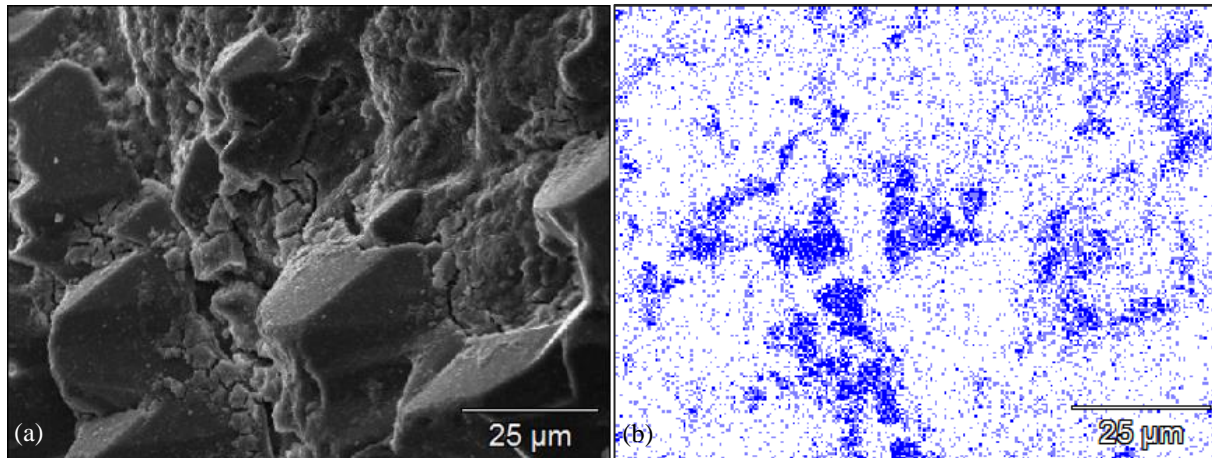


Fig. S6. SEM image (a) and energy dispersive X-ray (EDX) spectrum of element distribution (b) of representative Fe oxyhydroxide-coated sand surface. Blue color in (b) demonstrates patchy Fe oxyhydroxide coating.

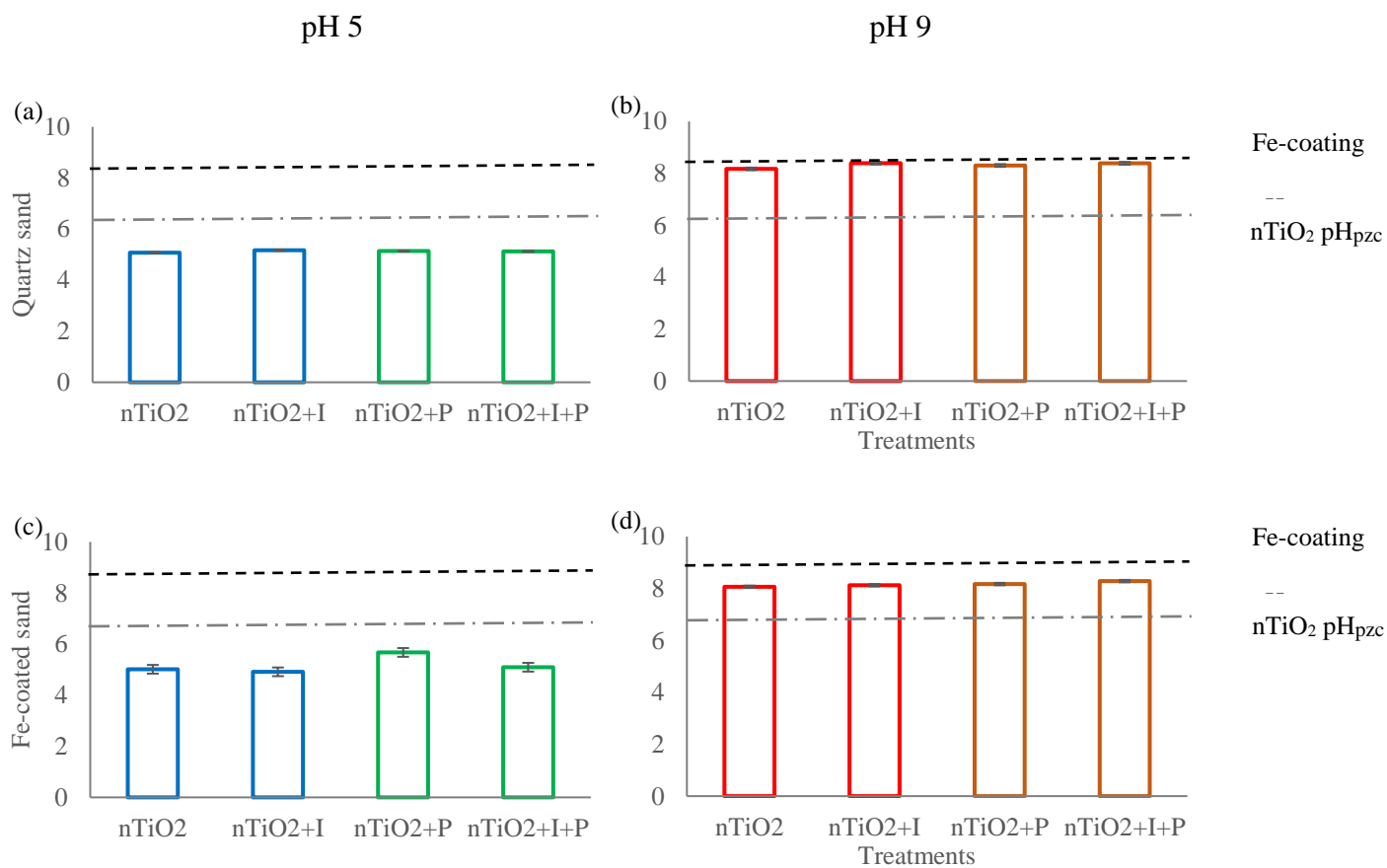


Fig. S7. Effluent pH for quartz sand column (a and b) and Fe-oxyhydroxide coated sand column (c and d). Background solution = 1 mM NaCl. I: illite colloid concentration = 10 mg/L. P: phosphate concentration = 10 mg/L. Data is expressed as mean \pm standard deviation of duplicate measurement.

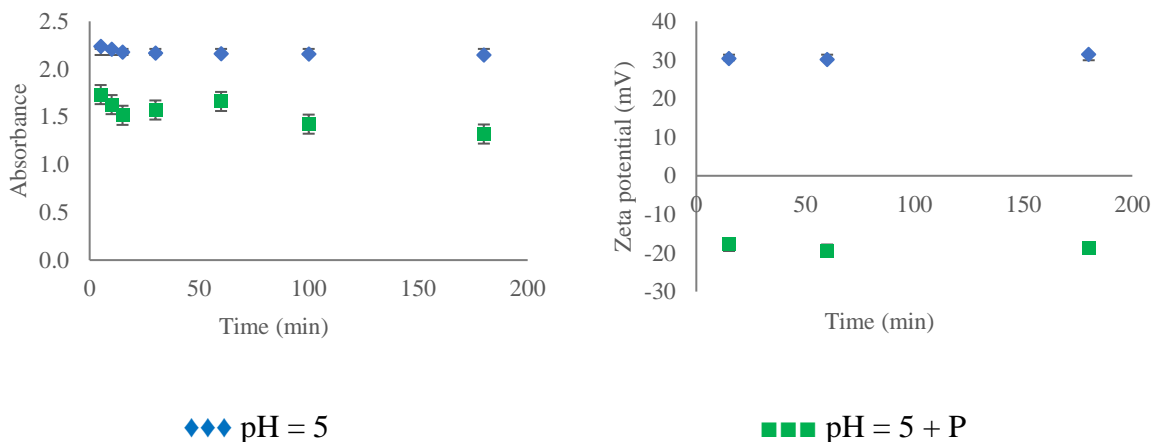


Fig. S8. Stability (a) and zeta potential (b) of nTiO₂ suspension over time before (blue diamonds) and after (green squares) adding 10 mg/L phosphate at pH 5 and 1 mM NaCl background.

To study the adsorption kinetics of phosphate on nTiO₂ particles at pH 5 in 1 mM NaCl background, nTiO₂ light absorbance was measured using a Thermo Scientific GENESYS 10S UV-vis spectrophotometer at a wavelength of 368 nm. The zeta potential and HDD were monitored at specified intervals (t = 0 to 180 minutes). nTiO₂-phosphate samples were prepared in duplicate and were shaken on an orbital shaker (Model 5000, VWR International) at ~300 rpm for 180 mins. The suspensions' pH was maintained at 5 ± 0.05 during shaking time.

Appendix 3. Supporting Information for Chapter 4

1. Additional materials and methods (DLVO calculations)

Interactions between nTiO₂ and collector surface (quartz sand, Fe oxyhydroxide coating, illite, and peat moss) was calculated using the following equations (Gregory, 1981; Hogg et al., 1966; Sun et al., 2015b):

$$\Phi_{LW} = -\frac{Ar_p}{6D} \left[1 + \frac{14D}{\lambda}\right]^{-1} \quad (S1)$$

$$\Phi_{EDL} = \pi \varepsilon_0 \varepsilon_r r_p \{2\psi_p \psi_s \ln \left[\frac{1 + \exp(-\kappa D)}{1 - \exp(-\kappa D)} \right] + (\psi_p^2 + \psi_s^2) \ln[1 - \exp(-2\kappa D)]\} \quad (S2)$$

where A is Hamaker constant, r_p refers to radius of the particle, D is separation distance, and λ is characteristic wavelength of interaction, usually taken to be 100 nm (Elimelech et al., 1995). ε_0 ($8.85 \times 10^{-12} \text{ C}^2 \text{ J}^{-1} \text{ m}^{-1}$) is permittivity of vacuum, ε_r (80) is relative dielectric constant of the medium, k_B is Boltzmann constant ($1.38 \times 10^{-23} \text{ m}^2 \text{ kg s}^{-2} \text{ K}^{-1}$), T is absolute temperature (K) of the system, ψ_p (V) and ψ_s are zeta potential of particle and collector surface, n_∞ (m^{-3}) is number concentrations of the bulk ions in bulk solution, and κ (m^{-1}) is Debye–Hückel reciprocal length and can be calculated using Equation (S3) (Chen et al., 2011).

$$\kappa = \sqrt{\left(\frac{e^2 \sum n_{i0} z_i^2}{\varepsilon_0 \varepsilon_r k_B T} \right)} \quad (S3)$$

where e is electron charge (1.602×10^{-19} coulombs), n_{i0} is number concentration of ion i in bulk solution (m^{-3}), z_i is valence of ion i in bulk solution.

Hamaker constant (A) values for the interactions of two dissimilar materials (1 and 2) via a third media (3) was obtained from previous studies as follows: nTiO₂-H₂O-SiO₂ = 1.4×10^{-20} J (Butt et al., 2005; Petosa et al., 2010), nTiO₂-H₂O-FeOx = 12.6×10^{-20} J (Wu and Cheng, 2016), nTiO₂-H₂O-illite = 2.0×10^{-20} J (Rastghalam et al., 2019), nTiO₂-H₂O-peat moss = 2.46×10^{-20} J (Zhou and Cheng, 2018).

2. Additional results

2.1. Supplementary table

Table 3. Physical properties of the column transport experiment. The Fe oxyhydroxide, illite, and peat moss mass reported is the dry mass in each column.

Influent pH	Medium type	Fe oxyhydroxide coating (g Fe)	Illite (g)	Peat moss (g)	Total mass of the medium ^a (g)	Average flow velocity (cm/h)	Column pore volume (cm ³)	Porosity	Bulk density (g/cm ³)	Particle mass recovery from effluent (%)
5	Quartz sand-sediment				130.88±1.36	31.56±0.07	27.99±0.06	0.38±0.008	1.75±0.003	11±1.5
	Fe-coated sand-sediment	0.01			128.99±0.42	32.31±0.34	27.34±0.29	0.37±0.003	1.76±0.001	13±0.8
	Quartz sand-sediment-illite		2.6		129.93±0.16	32.85±0.83	26.90±0.68	0.36±0.009	1.77±0.010	11±0.9
	Quartz sand-sediment-peat moss			0.26	129.46±0.26	32.31±0.50	27.34±0.43	0.37±0.005	1.75±0.010	15±0.5
9	Quartz sand-sediment				130.44±0.36	32.97±0.74	26.80±0.61	0.36±0.008	1.77±0.004	95±3.5
	Fe-coated sand-sediment	0.01			129.70±0.60	31.90±0.34	27.69±0.30	0.37±0.004	1.76±0.007	93±2.3
	Quartz sand-sediment-illite		2.6		129.76±0.57	32.01±0.94	27.61±0.81	0.37±0.010	1.76±0.007	82±2.4
	Quartz sand-sediment-peat moss			0.26	129.15±0.02	32.09±0.79	27.53±0.68	0.37±0.009	1.75±0.000	73±3.3

^a Sediment to sand mass ratio was 1:4.

2.2. Supplementary Figures

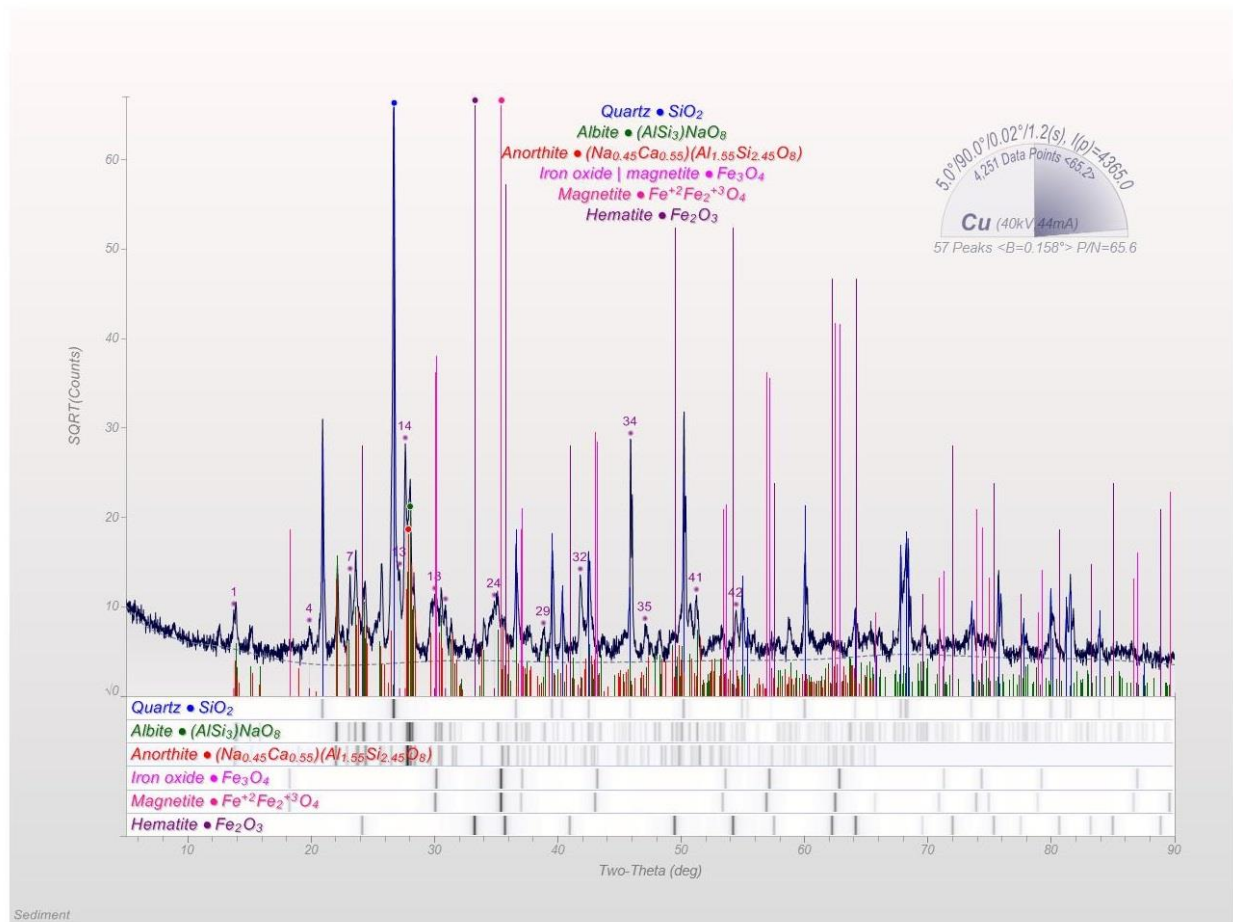


Fig. S9. X-ray diffraction (XRD) spectra of the sediment.

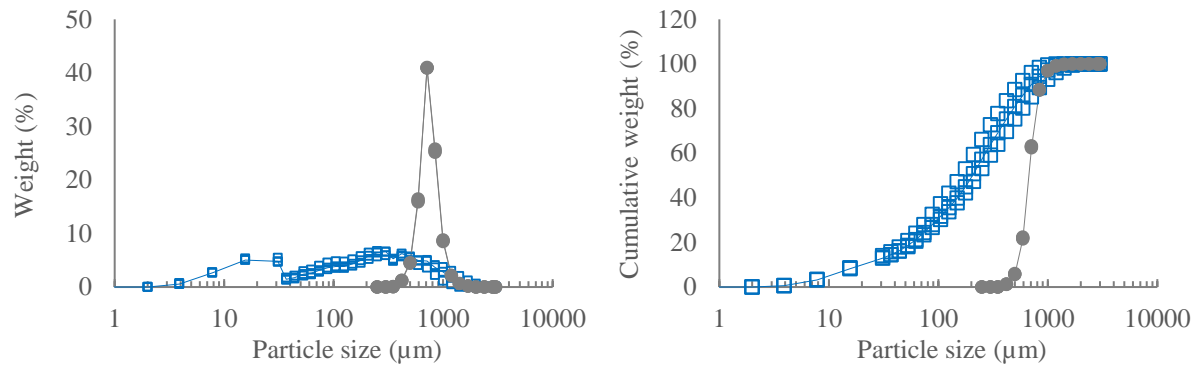


Fig. S10. Grain size distribution of sediment (blue squares) and quartz sand (gray circles) as determined by Horiba LA-950 Laser Particle Size Analyzer in triplicate.

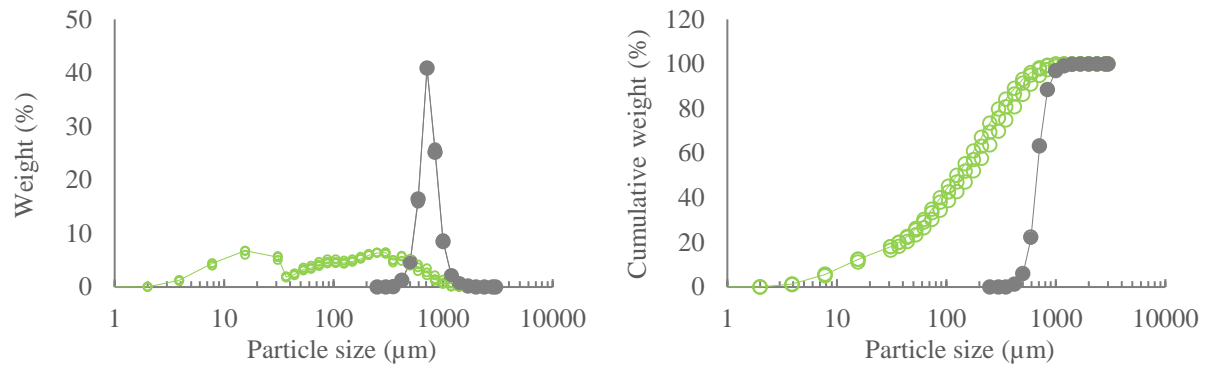


Fig. S11. Grain size distribution of illite (green circles) and quartz sand (gray circles) as determined by Horiba LA-950 Laser Particle Size Analyzer in triplicate.

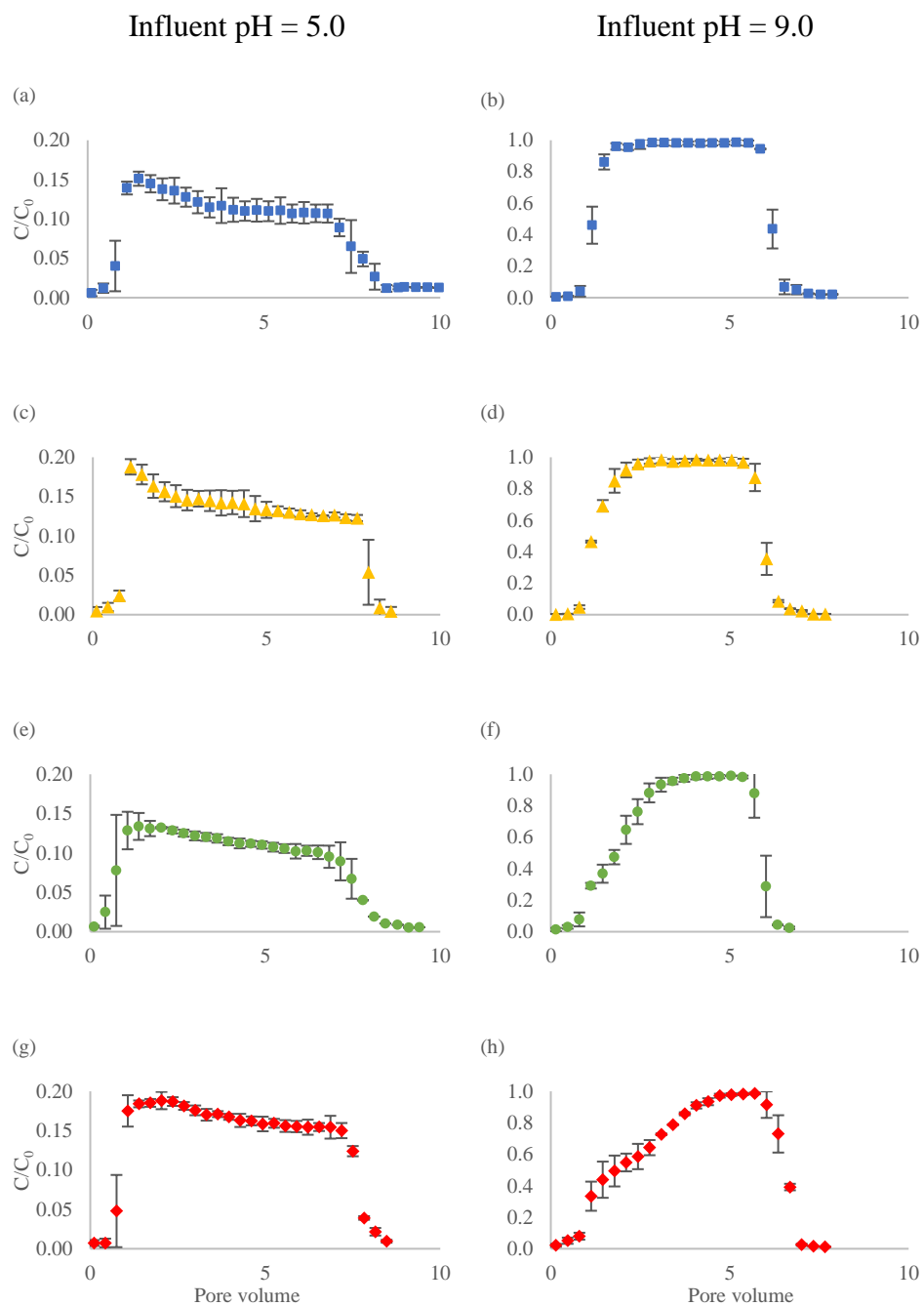


Fig. S12. Average of duplicate nTiO₂ breakthrough curve experiments with standard deviation as error bars. C₀ and C represent influent and effluent particle concentration, respectively.

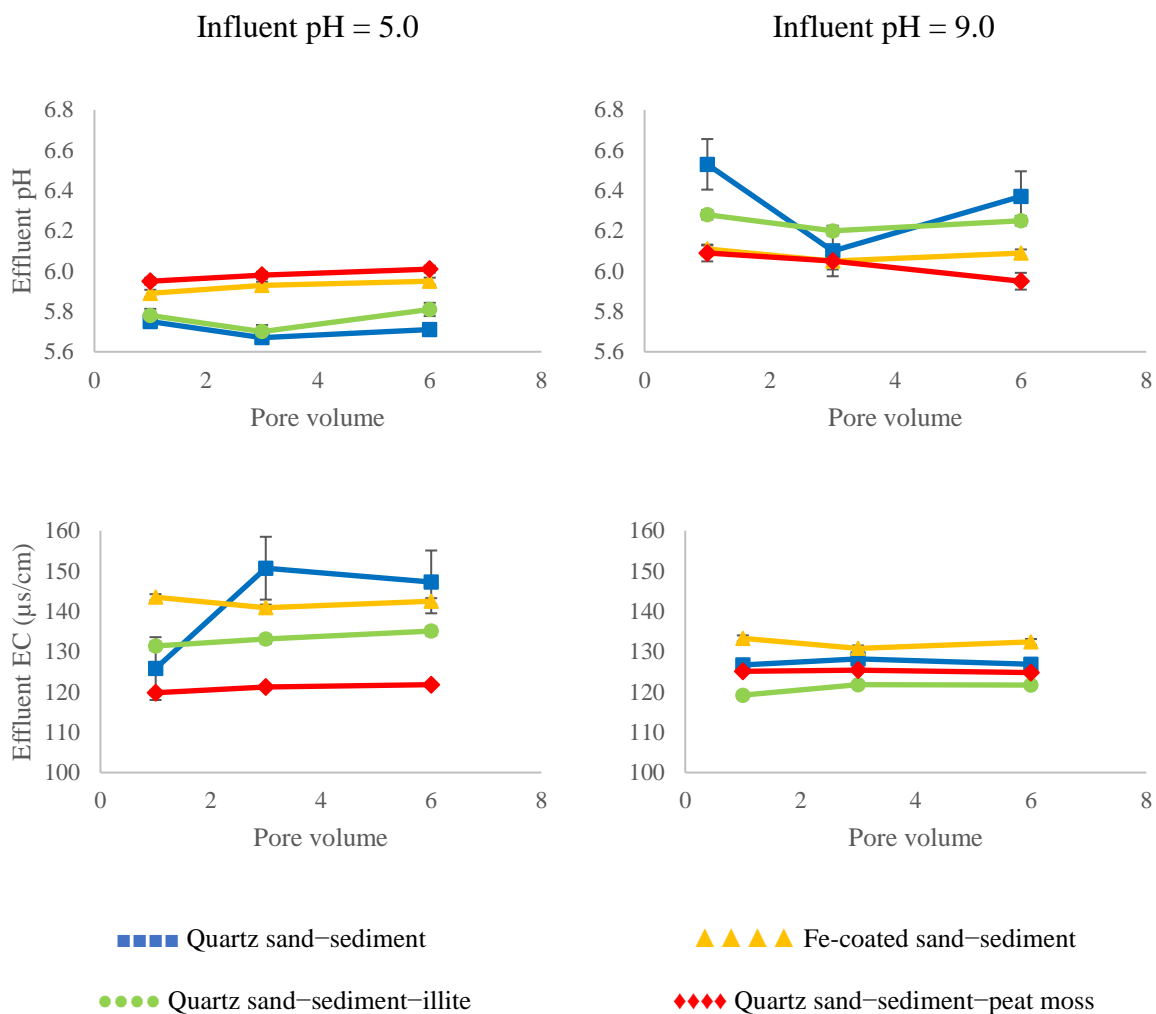


Fig. S13. Effluent pH and electrical conductivity (EC) vs. pore volume for columns with various medium. Illite and peat in the column = 2.60 g and 0.26 g, respectively. Influent $n\text{TiO}_2$ concentration = 100 mg/L and background solution = 1 mM NaCl. Data is expressed as mean \pm standard deviation of duplicate measurement.

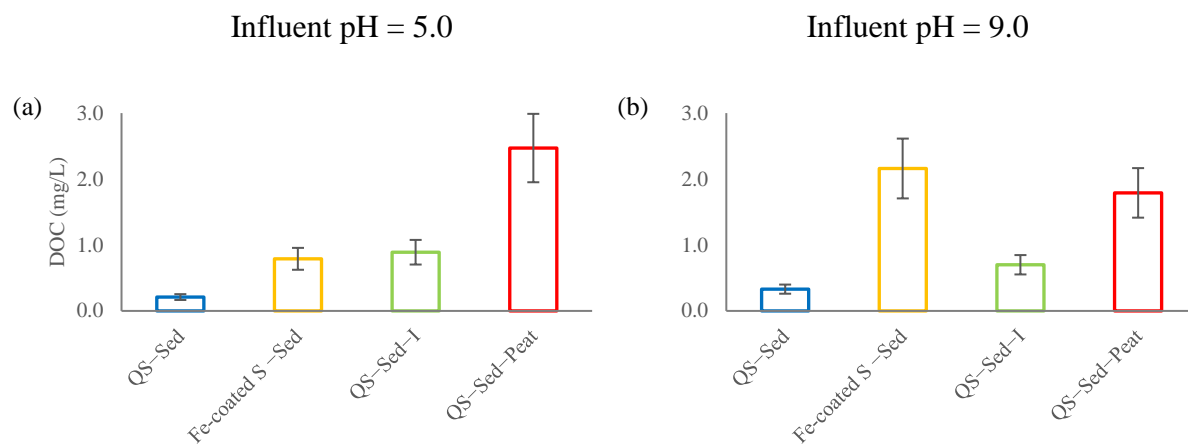
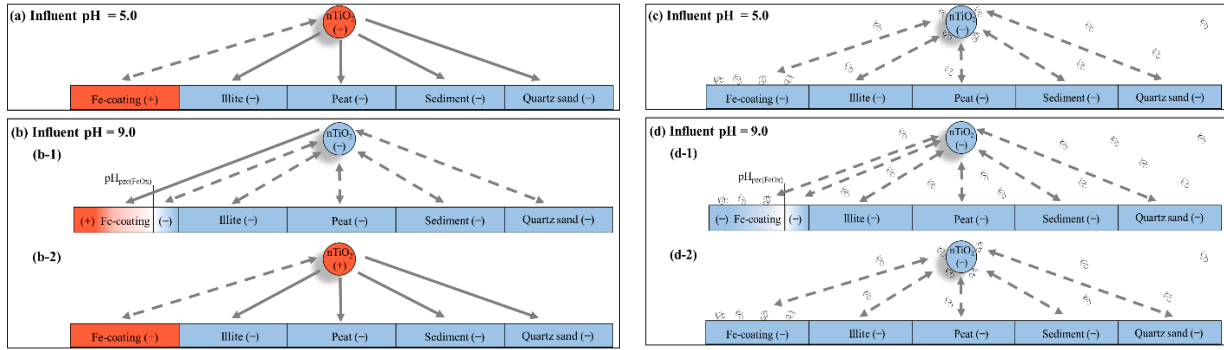


Fig. S14. Effluent DOC measurement for columns with various medium. Illite and peat in the column = 2.60 g and 0.26 g, respectively. Influent $n\text{TiO}_2$ concentration = 100 mg/L and background solution = 1 mM NaCl. Data is expressed as mean \pm estimated standard deviation. The uncertainty was estimated to be ~20% of the mean value.

DOC not considered

DOC considered



(a) $pH_{in} = 5.0 \leq pH_{porewater} \leq pH_{eff} \approx 6.0$

(c) $pH_{in} = 5.0 \leq pH_{porewater} \leq pH_{eff} \approx 6.0$

(b-1) $pH_{pzc(nTiO_2)} = 6.8 \leq pH_{porewater} \leq pH_{in} = 9.0$

(d-1) $pH_{pzc(nTiO_2)} = 6.8 \leq pH_{porewater} \leq pH_{in} = 9.0$

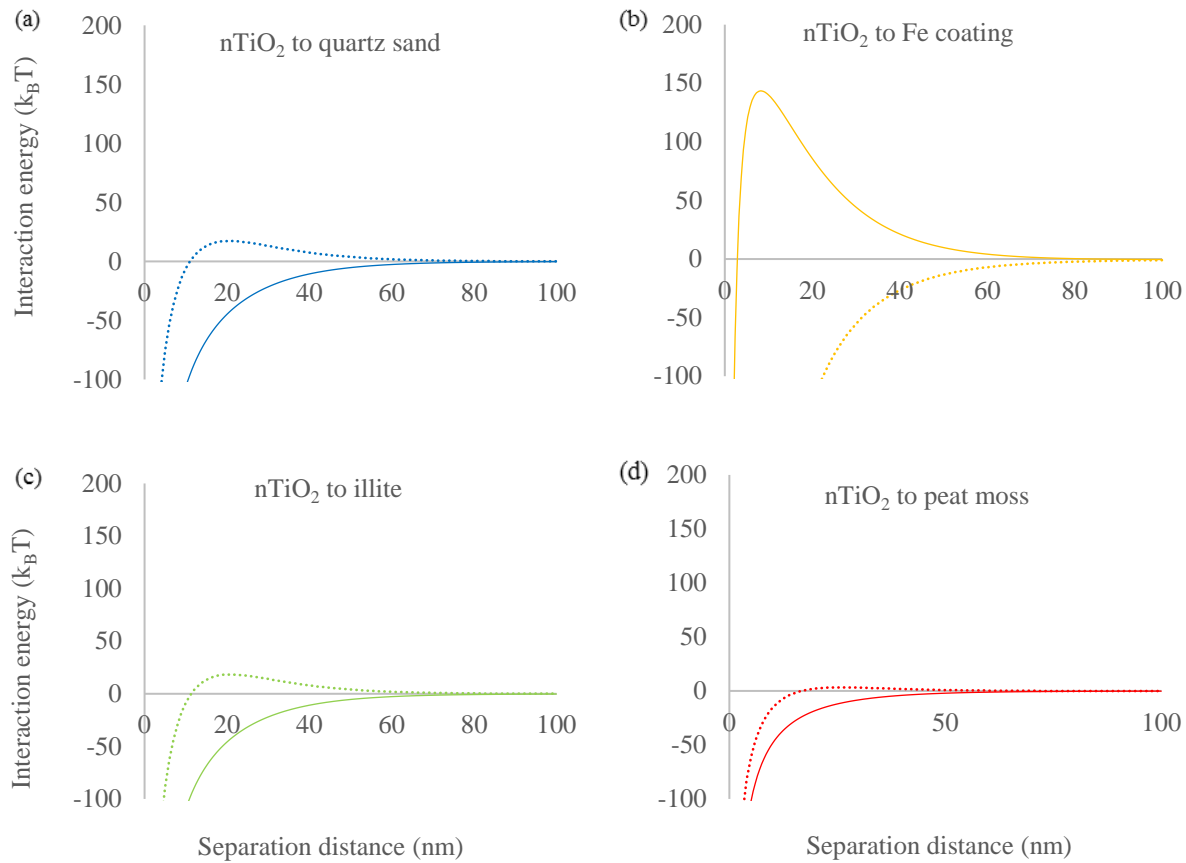
(b-2) $pH_{eff} \approx 6.1 \leq pH_{porewater} \leq pH_{pzc(nTiO_2)} = 6.8$

(d-2) $pH_{eff} \approx 6.1 \leq pH_{porewater} \leq pH_{pzc(nTiO_2)} = 6.8$

δ : DOC ■ : negatively charged surface ■ : positively charged surface

→ : attractive force ← - - - → : repulsive force

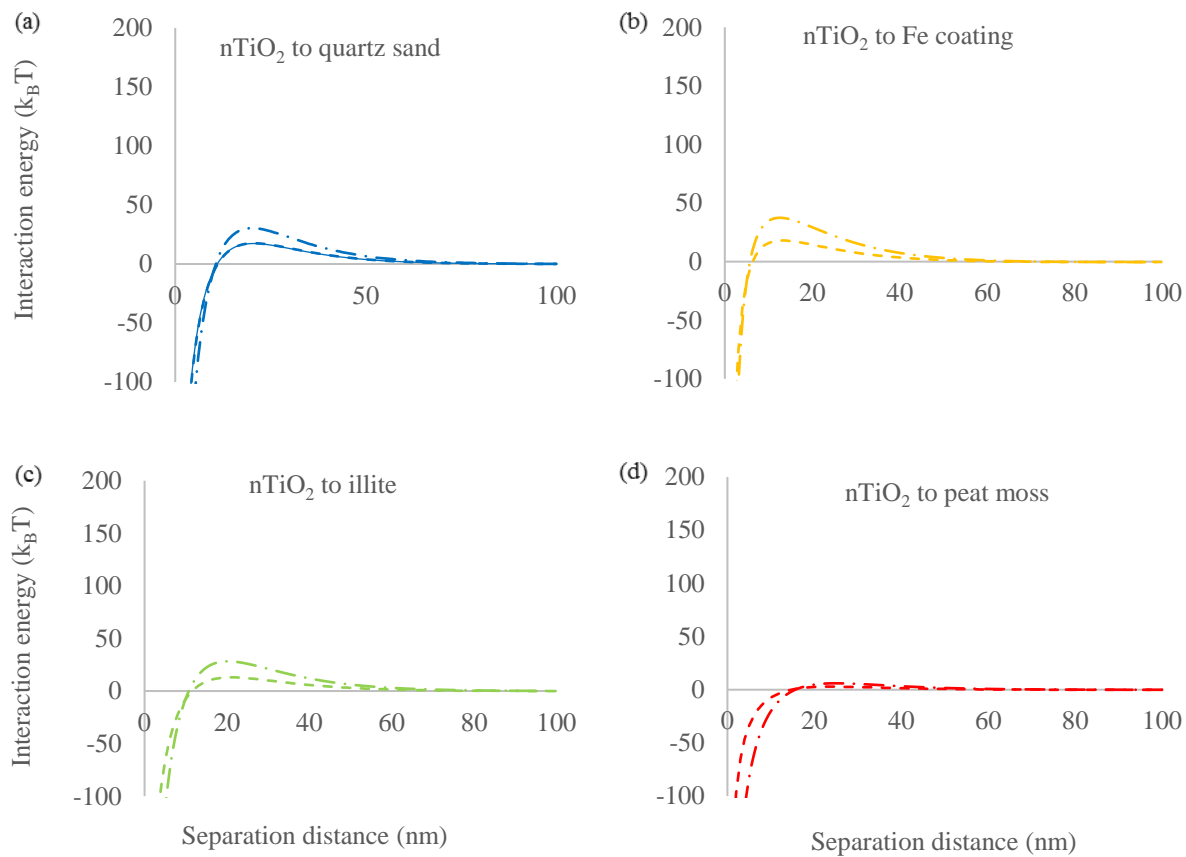
Fig. S15. Electrostatic interactions between nTiO₂ and various collectors using pH 5 (a & c) and pH 9 (b & d) influent suspensions. The point of zero charge (pH_{pzc}) of nTiO₂ and Fe coating are based on Rastghalam et al. (2018) and Wu and Cheng (2016) respectively. The zeta potential of peat moss is based on Zhou and Cheng (2018). The zeta potential of illite and quartz sand was measured in a previous study (Rastghalam et al., 2018). The zeta potential of nTiO₂ and the sediment was measured in this study.



Solid line: influent nTiO₂

Dotted line: effluent nTiO₂

Fig. S16. Particle-collector interaction energy vs. separation distance between nTiO₂ particles and (a) quartz sand, (b) Fe coating, (c) illite, and (d) peat moss in 1 mM NaCl solution at pH 5.



long dash-dotted line: influent nTiO₂

long dash line: effluent nTiO₂

Fig. S17. Particle-collector interaction energy vs. separation distance between nTiO₂ particles and (a) quartz sand, (b) Fe coating, (c) illite, and (d) peat moss in 1 mM NaCl solution at pH 9.

Appendix 4. All the original data for Chapter 2, 3, and 4 in electronic format

All the original data for Chapter 2, 3, and 4 are provided in electronic format.

References

- Akaighe, N., Depner, S.W., Banerjee, S., Sharma, V.K., Sohn, M., 2012. The effects of monovalent and divalent cations on the stability of silver nanoparticles formed from direct reduction of silver ions by Suwannee River humic acid/natural organic matter. *Sci. Total Environ.* 441, 277–289. <https://doi.org/10.1016/j.scitotenv.2012.09.055>
- Akanbi, M.O., Hernandez, L.M., Mobarok, M.H., Veinot, J.G.C., Tufenkji, N., 2018. QCM-D and NanoTweezer measurements to characterize the effect of soil cellulase on the deposition of PEG-coated TiO₂ nanoparticles in model subsurface environments. *Environ. Sci. Nano* 5, 2172–2183. <https://doi.org/10.1039/c8en00508g>
- Auset, M., Keller, A.A., 2006. Pore-scale visualization of colloid straining and filtration in saturated porous media using micromodels. *Water Resour. Res.* 42, 1–9. <https://doi.org/10.1029/2005WR004639>
- Baalousha, M., Nur, Y., Römer, I., Tejamaya, M., Lead, J.R., 2013. Effect of monovalent and divalent cations, anions and fulvic acid on aggregation of citrate-coated silver nanoparticles. *Sci. Total Environ.* 454–455, 119–131. <https://doi.org/10.1016/j.scitotenv.2013.02.093>
- Bang, S.H., Le, T.-H., Lee, S.K., Kim, P., Kim, J.S., Min, J., 2011. Toxicity Assessment of Titanium (IV) Oxide Nanoparticles Using *Daphnia magna* (Water Flea). *Environ. Health Toxicol.* 26, e2011002. <https://doi.org/10.5620/eh.2011.26.e2011002>
- Bayat, A.E., Junin, R., Mohsin, R., Hokmabadi, M., Shamshirband, S., 2015. Influence of clay particles on Al₂O₃ and TiO₂ nanoparticles transport and retention through limestone porous media : measurements and mechanisms. *J. Nanoparticle Res.* 17, 1–14. <https://doi.org/10.1007/s11051-015-3031-4>
- Ben-Moshe, T., Dror, I., Berkowitz, B., 2010. Transport of metal oxide nanoparticles in saturated

- porous media. *Chemosphere* 81, 387–393.
<https://doi.org/10.1016/j.chemosphere.2010.07.007>
- Bergström, L., 1997. Hamaker constants of inorganic materials. *Adv. Colloid Interface Sci.* 70, 125–169.
- Bolan, N.S., Barrow, N.J., 1984. Modelling the effect of adsorption of phosphate and other anions on the surface charge of variable charge oxides. *J. Soil Sci.* 35, 273–281.
- Borggaard, O.K., Gimsing, A.L., Strobel, B.W., 2005. Influence of humic substances on phosphate adsorption by aluminium and iron oxides. *Geoderma* 127, 270–279.
<https://doi.org/10.1016/j.geoderma.2004.12.011>
- Bradford, S.A., Bettahar, M., 2006. Concentration dependent transport of colloids in saturated porous media. *J. Contam. Hydrol.* 82, 99–117.
<https://doi.org/10.1016/j.jconhyd.2005.09.006>
- Bradford, S.A., Kim, H., Shen, C., Sasidharan, S., Shang, J., 2017. Contributions of Nanoscale Roughness to Anomalous Colloid Retention and Stability Behavior 33, 10094–10105.
<https://doi.org/10.1021/acs.langmuir.7b02445>
- Bradford, S.A., Simunek, J., Bettahar, M., Tadassa, Y.F., van Genuchten, M.T., Yates, S.R., 2005. Straining of colloids at textural interfaces. *Water Resour. Res.* 41, 1–18.
<https://doi.org/10.1029/2004wr003675>
- Bradford, S.A., Simunek, J., Bettahar, M., van Genuchten, M.T., Yates, S.R., 2003. Modeling Colloid Attachment, Straining, and Exclusion in Saturated Porous Media. *Environ. Sci. Technol.* 37, 2242–2250. <https://doi.org/10.1021/es025899u>
- Bradl, H.B., 2004. Adsorption of heavy metal ions on soils and soils constituents. *J. Colloid Interface Sci.* 277, 1–18. <https://doi.org/10.1016/j.jcis.2004.04.005>

- Butt, H.-J., Cappella, B., Kappl, M., 2005. Force measurements with the atomic force microscope: Technique, interpretation and applications. *Surf. Sci. Rep.* 59, 1–152.
- Cai, L., Tong, M., Ma, H., Kim, H., 2013. Cotransport of Titanium Dioxide and Fullerene Nanoparticles in Saturated Porous Media. *Environ. Sci. Technol.* 47, 5703–5710.
<https://doi.org/10.1021/es400256d>
- Cai, L., Tong, M., Wang, X., Kim, H., 2015. Effect of different-sized colloids on the transport and deposition of titanium dioxide nanoparticles in quartz sand. *Environ. Pollut.* 208, 637–644. <https://doi.org/10.1021/es5019652>
- Cai, L., Tong, M., Wang, X., Kim, H., 2014. Influence of clay particles on the transport and retention of titanium dioxide nanoparticles in quartz sand. *Environ. Sci. Technol.* 48, 7323–7332.
- Carstens, J.F., Bachmann, J., Neuweiler, I., 2018. Effects of organic matter coatings on the mobility of goethite colloids in model sand and undisturbed soil. *Eur. J. Soil Sci.* 69, 360–369.
- Cary, L., Pauwels, H., Ollivier, P., Picot, G., Leroy, P., Mougín, B., Braibant, G., Labille, J., 2015. Evidence for TiO₂ nanoparticle transfer in a hard-rock aquifer. *J. Contam. Hydrol.* 179, 148–159. <https://doi.org/10.1016/j.jconhyd.2015.06.007>
- Chen, G., Liu, X., Su, C., 2012. Distinct effects of humic acid on transport and retention of TiO₂ rutile nanoparticles in saturated sand columns. *Environ. Sci. Technol.* 46, 7142–7150.
<https://doi.org/10.1021/es204010g>
- Chen, G., Liu, X., Su, C., 2011. Transport and retention of TiO₂ rutile nanoparticles in saturated porous media under low-ionic-strength conditions: Measurements and mechanisms. *Langmuir* 27, 5393–5402. <https://doi.org/10.1021/la200251v>

- Chen, M., Xu, N., Cao, X., Zhou, K., Chen, Z., Wang, Y., Liu, C., 2015. Facilitated transport of anatase titanium dioxides nanoparticles in the presence of phosphate in saturated sands. *J. Colloid Interface Sci.* 451, 134–143. <https://doi.org/10.1016/j.jcis.2015.04.010>
- Chen, X., 2015. Modeling of experimental adsorption isotherm data. *Inf.* 6, 14–22. <https://doi.org/10.3390/info6010014>
- Chen, X., Mao, S.S., 2007. Titanium dioxide nanomaterials: synthesis, properties, modifications, and applications. *Chem. Rev.* 107, 2891–2959.
- Chen, X.G., Li, J.P., Li, Z.J., Chen, B. De, Han, Y.J., 2006. Vegetation change in Yanchi of Ningxia and its relationship with climate change in recent years. *Acta Ecol. Sin.* 26, 1516–1522. <https://doi.org/10.1021/es0518068>
- Cheng, T., Barnett, M.O., Roden, E.E., Zhuang, J., 2004. Effects of phosphate on uranium(VI) adsorption to goethite-coated sand. *Environ. Sci. Technol.* 38, 6059–6065. <https://doi.org/10.1021/es040388o>
- Chowdhury, I., Cwiertny, D.M., Walker, S.L., 2012. Combined factors influencing the aggregation and deposition of nano-TiO₂ in the presence of humic acid and bacteria. *Environ. Sci. Technol.* 46, 6968–6976. <https://doi.org/10.1021/es2034747>
- Chowdhury, I., Hong, Y., Honda, R.J., Walker, S.L., 2011. Mechanisms of TiO₂ nanoparticle transport in porous media: Role of solution chemistry, nanoparticle concentration, and flowrate. *J. Colloid Interface Sci.* 360, 548–555. <https://doi.org/10.1016/j.jcis.2011.04.111>
- Connor, P.A., McQuillan, A.J., 1999. Phosphate Adsorption onto TiO₂ from Aqueous Solutions: An in Situ Internal Reflection Infrared Spectroscopic Study. *Langmuir* 15, 2916–2921. <https://doi.org/10.1021/LA980894P>
- Cornelis, G., DooletteMadeleine Thomas, C., McLaughlin, M.J., Kirby, J.K., Beak, D.G.,

- Chittleborough, D., 2012. Retention and Dissolution of Engineered Silver Nanoparticles in Natural Soils. *Soil Sci. Soc. Am. J.* 76, 891–902. <https://doi.org/10.2136/sssaj2011.0360>
- Cornelis, G., Pang, L., Doolette, C., Kirby, J.K., Mclaughlin, M.J., 2013. Transport of silver nanoparticles in saturated columns of natural soils. *Sci. Total Environ.* 464, 120–130. <https://doi.org/10.1016/j.scitotenv.2013.05.089>
- Delay, M., Frimmel, F.H., 2012. Nanoparticles in aquatic systems. *Anal. Bioanal. Chem.* 402, 583–592. <https://doi.org/10.1007/s00216-011-5443-z>
- Derjaguin, B. V, Landau, L., 1941. Theory of the stability of strongly charged lyophobic sols and of the adhesion of strongly charged particles in solution of electrolytes. *Acta Physicochim USSR* 14, 633–662.
- Domingos, R.F., Tufenkji, N., Wilkinson, K.J., 2009. Aggregation of Titanium Dioxide Nanoparticles : Role of a Fulvic Acid Aggregation of Titanium Dioxide Nanoparticles : Role of a Fulvic Acid. *Environ. Sci. Technol.* 43, 1282–1286. <https://doi.org/10.1021/es8023594>
- Dror, I., Jacov, O.M., Cortis, A., Berkowitz, B., 2012. Catalytic transformation of persistent contaminants using a new composite material based on nanosized zero-valent iron. *ACS Appl. Mater. Interfaces* 4, 3416–3423.
- Du, W., Sun, Y., Ji, R., Zhu, J., Wu, J., Guo, H., 2011. TiO₂ and ZnO nanoparticles negatively affect wheat growth and soil enzyme activities in agricultural soil. *J. Environ. Monit.* 13, 822–828. <https://doi.org/10.1039/C0EM00611D>
- Dubinina, M.M., 1947. The equation of the characteristic curve of activated charcoal, in: *Dokl. Akad. Nauk. SSSR.* pp. 327–329.
- El Hadri, H., Louie, S.M., Hackley, V.A., 2018. Assessing the interactions of metal nanoparticles

- in soil and sediment matrices—a quantitative analytical multi-technique approach. *Environ. Sci. Nano* 5, 203–214. <https://doi.org/10.1039/c7en00868f>
- Elimelech, M., Gregory, J., Jia, X., 2013. *Particle Deposition and Aggregation: Measurement, Modelling and Simulation*. Butterworth-Heinemann, London.
- Elimelech, M., Gregory, J., Jia, X., Williams, R., 1995. Particle deposition and aggregation, measurement, modeling and simulation. *Colloids Surfaces A Physicochem. Eng. Asp.* 1, 93–94.
- Elimelech, M., Nagai, M., Ko, C.H., Ryan, J.N., 2000. Relative insignificance of mineral grain zeta potential to colloid transport in geochemically heterogeneous porous media. *Environ. Sci. Technol.* 34, 2143–2148. <https://doi.org/10.1021/es9910309>
- Fang, J., Shan, X., Wen, B., Lin, J., Owens, G., 2009. Stability of titania nanoparticles in soil suspensions and transport in saturated homogeneous soil columns. *Environ. Pollut.* 157, 1101–1109. <https://doi.org/10.1016/j.envpol.2008.11.006>
- Fang, J., Shan, X., Wen, B., Lin, J., Owens, G., Zhou, S., 2011. Transport of copper as affected by titania nanoparticles in soil columns. *Environ. Pollut.* 159, 1248–1256. <https://doi.org/10.1016/j.envpol.2011.01.039>
- Fang, J., Xu, M., Jia, Wang, D. jun, Wen, B., Han, J. yi, 2013. Modeling the transport of TiO₂nanoparticle aggregates in saturated and unsaturated granular media: Effects of ionic strength and pH. *Water Res.* 47, 1399–1408. <https://doi.org/10.1016/j.watres.2012.12.005>
- Farré, M., Gajda-Schranz, K., Kantiani, L., Barceló, D., 2009. Ecotoxicity and analysis of nanomaterials in the aquatic environment. *Anal. Bioanal. Chem.* 393, 81–95.
- Faure, B., Salazar-Alvarez, G., Bergström, L., 2011. Hamaker constants of iron oxide nanoparticles. *Langmuir* 27, 8659–8664.

- Fetter, C.W., 2001. Applied hydrogeology. Waveland Press.
- Fisher-Power, L.M., Cheng, T., 2018. Nanoscale titanium dioxide (nTiO₂) transport in natural sediments : Importance of soil organic matter and Fe / Al Oxyhydroxides. Environ. Sci. Technol. 52, 2668–2676. <https://doi.org/10.1021/acs.est.7b05062>
- Fisher-Power, L.M., Shi, Z., Cheng, T., 2019. Testing the “component additivity” approach for modelling Cu and Zn adsorption to a natural sediment. Chem. Geol. 512, 31–42. <https://doi.org/10.1016/j.chemgeo.2019.02.038>
- Foo, K.Y., Hameed, B.H., 2010. Insights into the modeling of adsorption isotherm systems. Chem. Eng. J. 156, 2–10.
- French, R. a., Jacobson, A.R., Kim, B., Isley, S.L., Penn, R.L.E.E., Baveye, P.C., 2009. Influence of ionic strength, pH, and cation valence on aggregation kinetics of titanium dioxide nanoparticles. Environ. Sci. Technol. 43, 1354–1359. <https://doi.org/10.1021/es802628n>
- Freundlich, H.M.F., 1906. Over the adsorption in solution. J. Phys. Chem 57, 1100–1107.
- Gao, B., Saiers, J.E., 2004. Deposition and mobilization of clay colloids in unsaturated porous media. Water Resour. Res. 40, 1–8. <https://doi.org/10.1029/2004WR003189>
- Gentile, G.J., Fidalgo de Cortalezzi, M.M., 2016. Enhanced retention of bacteria by TiO₂ nanoparticles in saturated porous media. J. Contam. Hydrol. 191, 66–75. <https://doi.org/10.1016/j.jconhyd.2016.05.004>
- Godinez, I.G., Darnault, C.J.G., Khodadoust, A.P., Bogdan, D., 2013. Deposition and release kinetics of nano-TiO₂ in saturated porous media: Effects of solution ionic strength and surfactants. Environ. Pollut. 174, 106–113. <https://doi.org/10.1016/j.envpol.2012.11.002>
- Goldberg, E., Scheringer, M., Bucheli, T.D., Hungerbühler, K., 2014. Critical assessment of models for transport of engineered nanoparticles in saturated porous media. Environ. Sci.

Technol. 48, 12732–12741.

Gómez-Merino, A.I., Rubio-Hernández, F. J., Velázquez-Navarro, J. F., Galindo-Rosales, F.J., Fortes-Quesada, P., 2007. The Hamaker constant of anatase aqueous suspensions. *J. Colloid Interface Sci.* 316, 451–456. <https://doi.org/10.1016/j.jcis.2007.08.001>

Gregory, J., 1981. Approximate expressions for retarded van der Waals interaction. *J. Colloid Interface Sci.* 83, 138–145.

Guo, P., Xu, N., Li, D., Huangfu, X., Li, Z., 2018. Aggregation and transport of rutile titanium dioxide nanoparticles with montmorillonite and diatomite in the presence of phosphate in porous sand. *Chemosphere* 204, 327–334.
<https://doi.org/10.1016/j.chemosphere.2018.04.041>

Gustafsson J, 2010. Visual Minteq Ver 3.0. Retrieved from. <http://vminteq.lwr.kth.se/download/>.

Guzman, K.A.D., Finnegan, M.P., Banfield, J.F., 2006. Influence of surface potential on aggregation and transport of titania nanoparticles. *Environ. Sci. Technol.* 40, 7688–7693.
<https://doi.org/10.1021/es060847g>

Han, P., Shen, X., Yang, H., Kim, H., Tong, M., 2013. *Colloids and Surfaces B : Biointerfaces* Influence of nutrient conditions on the transport of bacteria in saturated porous media. *Colloids Surfaces B Biointerfaces* 102, 752–758.
<https://doi.org/10.1016/j.colsurfb.2012.08.053>

Han, P., Wang, X., Cai, L., Tong, M., Kim, H., 2014. Transport and retention behaviors of titanium dioxide nanoparticles in iron oxide-coated quartz sand: Effects of pH, ionic strength, and humic acid. *Colloids Surfaces A Physicochem. Eng. Asp.* 454, 119–127.
<https://doi.org/10.1016/j.colsurfa.2014.04.020>

- Han, P., Zhou, D., Tong, M., Kim, H., 2016. Effect of bacteria on the transport and deposition of multi-walled carbon nanotubes in saturated porous media *. *Environ. Pollut.* 213, 895–903. <https://doi.org/10.1016/j.envpol.2016.03.058>
- Hassellöv, M., Readman, J.W., Ranville, J.F., Tiede, K., 2008. Nanoparticle analysis and characterization methodologies in environmental risk assessment of engineered nanoparticles. *Ecotoxicology* 17, 344–361.
- He, H., Cheng, Y., Yang, C., Zeng, G., Zhu, C., Yan, Z., 2017. Influences of anion concentration and valence on dispersion and aggregation of titanium dioxide nanoparticles in aqueous solutions. *J. Environ. Sci. (China)* 54, 135–141. <https://doi.org/10.1016/j.jes.2016.06.009>
- Hiemenz, P.C., Rajagopalan, R., 1997. *Principles of Colloid and Surface Chemistry*, revised and expanded, 3rd ed. CRC press, New York.
- Hogg, R., Healy, T.W., Fuerstenau, D.W., 1966. Mutual coagulation of colloidal dispersions. *Trans. Faraday Soc.* 62, 1638–1651.
- Hough, D.B., White, L.R., 1980. The calculation of Hamaker constants from Lifshitz theory with applications to wetting phenomena. *Adv. Colloid Interface Sci.* 14, 3–41.
- Hu, J., Shipley, H.J., 2012. Evaluation of desorption of Pb (II), Cu (II) and Zn (II) from titanium dioxide nanoparticles. *Sci. Total Environ.* 431, 209–220.
- Huang, P.M., 1995. *Environmental Impacts of Soil Component Interactions: Metals, Other Inorganics, and Microbial Activities*. CRC Press.
- Hussain, S.A., Demirci, Ş., Özbayoğlu, G., 1996. Zeta potential measurements on three clays from Turkey and effects of clays on coal flotation. *J. Colloid Interface Sci.* 184, 535–541. <https://doi.org/10.1006/jcis.1996.0649>
- Hwang, G., Gomez-flores, A., Bradford, S.A., Choi, S., Jo, E., Bae, S., Tong, M., Kim, H., 2018.

- Analysis of stability behavior of carbon black nanoparticles in ecotoxicological media :
Hydrophobic and steric effects. *Colloids Surfaces A* 554, 306–316.
<https://doi.org/10.1016/j.colsurfa.2018.06.049>
- Israelachvili, J.N., 2011. *Intermolecular and surface forces*. Academic press.
- Jada, A., Ait Akbour, R., Douch, J., 2006. Surface charge and adsorption from water onto quartz sand of humic acid. *Chemosphere* 64, 1287–1295.
<https://doi.org/10.1016/j.chemosphere.2005.12.063>
- Jang, H.M., Fuerstenau, D.W., 1986. The specific adsorption of alkaline-earth cations at the rutile/water interface. *Colloids and surfaces* 21, 235–257.
- Jiang, C.L., Séquaris, J.M., Vereecken, H., Klumpp, E., 2012. Effects of inorganic and organic anions on the stability of illite and quartz soil colloids in Na-, Ca- and mixed Na-Ca systems. *Colloids Surfaces A Physicochem. Eng. Asp.* 415, 134–141.
<https://doi.org/10.1016/j.colsurfa.2012.10.007>
- Jung, B., O’Carroll, D., Sleep, B., 2014. The influence of humic acid and clay content on the transport of polymer-coated iron nanoparticles through sand. *Sci. Total Environ.* 496, 155–164. <https://doi.org/10.1016/j.scitotenv.2014.06.075>
- Kang, S.A., Li, W., Lee, H.E., Phillips, B.L., Jae, Y., 2011. Phosphate uptake by TiO₂ : Batch studies and NMR spectroscopic evidence for multisite adsorption. *J. Colloid Interface Sci.* 364, 455–461. <https://doi.org/10.1016/j.jcis.2011.07.088>
- Kaya, A., Yukselen, Y., 2005. Zeta potential of clay minerals and quartz contaminated by heavy metals. *Can. Geotech. J.* 42, 1280–1289. <https://doi.org/10.1139/t05-048>
- Kim, C., Lee, J., Lee, S., 2015. TiO₂ nanoparticle sorption to sand in the presence of natural organic matter. *Environ. Earth Sci.* 73, 5585–5591. <https://doi.org/10.1007/s12665-014->

- Kirby, B.J., Hasselbrink, E.F., 2004. Zeta potential of microfluidic substrates: 1. Theory, experimental techniques, and effects on separations. *Electrophoresis* 25, 187–202. <https://doi.org/10.1002/elps.200305754>
- Klaine, S.J., Alvarez, P.J.J., Batley, G.E., Fernandes, T.F., Handy, R.D., Lyon, D.Y., Mahendra, S., 2012. McLaughlin MJ, Lead JR. 2008. Nanomaterials in the environment: Behavior, fate, bioavailability, and effects. *Environ Toxicol Chem* 27: 1825–1851. DOI: 10.1897/08-090.1 In the article “Nanomaterials in the environment: Behavior, fate, bioavailability, and. *Environ. Toxicol. Chem.* 31, 2893.
- Konecny, R., 2001. Reactivity of hydroxyl radicals on hydroxylated quartz surface - 1: Cluster model calculations. *J. Phys. Chem. B* 105, 6221–6226. <https://doi.org/10.1021/jp010752v>
- Kosmulski, M., 2002. The significance of the difference in the point of zero charge between rutile and anatase. *Adv. Colloid Interface Sci.* 99, 255–264.
- Langmuir, I., 1916. The constitution and fundamental properties of solids and liquids. Part I. Solids. *J. Am. Chem. Soc.* 38, 2221–2295.
- Larue, C., Baratange, C., Vantelon, D., Khodja, H., Surblé, S., Elger, A., Carrière, M., 2018. Influence of soil type on TiO₂ nanoparticle fate in an agro-ecosystem. *Sci. Total Environ.* 630, 609–617. <https://doi.org/10.1016/j.scitotenv.2018.02.264>
- Laxman, V., Larios, A.D., Cledón, M., Kaur, S., Verma, M., Surampalli, R.Y., 2016. Behavior and characterization of titanium dioxide and silver nanoparticles in soils. *Sci. Total Environ.* 563–564, 933–943. <https://doi.org/10.1016/j.scitotenv.2015.11.090>
- Li, D., Chang, H.S., Seaman, J.C., Kaplan, D.I., 2013. Effects of matrix heterogeneity and aqueous humic acid on transport and deposition of mineral colloids in sandy sediments. *J.*

- Environ. Chem. Eng. 1, 875–883. <https://doi.org/10.1016/j.jece.2013.07.032>
- Lin, D., Tian, X., Wu, F., Xing, B., 2010. Fate and Transport of Engineered Nanomaterials in the Environment. *J. Environ. Qual.* 39, 1896–1908. <https://doi.org/10.2134/jeq2009.0423>
- Lin, S., Cheng, Y., Bobcombe, Y., L. Jones, K., Liu, J., Wiesner, M.R., 2011. Deposition of Silver Nanoparticles in Geochemically Heterogeneous Porous Media: Predicting Affinity from Surface Composition Analysis. *Environ. Sci. Technol.* 45, 5209–5215. <https://doi.org/10.1021/es2002327>
- Liu, L., Gao, B., Wu, L., Morales, V.L., Yang, L., Zhou, Z., Wang, H., 2013. Deposition and transport of graphene oxide in saturated and unsaturated porous media. *Chem. Eng. J.* 229, 444–449.
- Liu, L., Neretniek, I., 2010. Interaction between colloidal particles. Sweden.
- Long, J., Xu, Z., Masliyah, J.H., 2006. Role of illite-illite interactions in oil sands processing. *Colloids Surfaces A Physicochem. Eng. Asp.* 281, 202–214. <https://doi.org/10.1016/j.colsurfa.2006.02.059>
- Loosli, F., Le Coustumer, P., Stoll, S., 2015. Effect of electrolyte valency, alginate concentration and pH on engineered TiO₂ nanoparticle stability in aqueous solution. *Sci. Total Environ.* 535, 28–34. <https://doi.org/10.1016/j.scitotenv.2015.02.037>
- Loosli, F., Le Coustumer, P., Stoll, S., 2013. TiO₂ nanoparticles aggregation and disaggregation in presence of alginate and Suwannee River humic acids. pH and concentration effects on nanoparticle stability. *Water Res.* 47, 6052–6063. <https://doi.org/10.1016/j.watres.2013.07.021>
- Lv, J., Zhang, S., Luo, L., Han, W., Zhang, J., Yang, K., Christie, P., 2012. Dissolution and microstructural transformation of ZnO nanoparticles under the influence of phosphate.

- Environ. Sci. Technol. 46, 7215–7221. <https://doi.org/10.1021/es301027a>
- Lv, X., Gao, B., Sun, Y., Dong, S., Wu, J., Jiang, B., Shi, X., 2016. Effects of grain size and structural heterogeneity on the transport and retention of nano-TiO₂ in saturated porous media. *Sci. Total Environ.* 563–564, 987–995.
<https://doi.org/10.1016/j.scitotenv.2015.12.128>
- Mackevica, A., Foss Hansen, S., 2016. Release of nanomaterials from solid nanocomposites and consumer exposure assessment – a forward-looking review. *Nanotoxicology* 10, 641–653.
<https://doi.org/10.3109/17435390.2015.1132346>
- Malvern Panalytical Ltd., 2018. Dynamic light scattering: An introduction in 30 minutes. Technical note (MRK656-01).
- McCarthy, J.F., McKay, L.D., 2004. Colloid transport in the subsurface. *Vadose Zo. J.* 3, 326–337.
- McKeague, J.A., Day, J.H., 1966. Dithionite- and Oxalate-extractable Fe and Al as aids in differentiating various classes of soils. *Can. J. Soil Sci.* 46, 13–22.
<https://doi.org/10.4141/cjss66-003>
- Médout-Marère, V., 2000. A simple experimental way of measuring the Hamaker constant of divided solids by immersion calorimetry in apolar liquids. *J. Colloid Interface Sci.* 228, 434–437. <https://doi.org/10.1006/jcis.2000.6984>
- Mehra, O.P., Jackson, M.L., 1960. Iron Oxide Removal From Soils and Clays By a Dithionite–Citrate System Buffered With Sodium Bicarbonate. *Clays Clay Miner.* 7, 317–327.
<https://doi.org/10.1016/b978-0-08-009235-5.50026-7>
- Mizutani, K., Fisher-Power, L.M., Shi, Z., Cheng, T., 2017. Cu and Zn adsorption to a terrestrial sediment: Influence of solid-to-solution ratio. *Chemosphere* 175, 341–349.

<https://doi.org/10.1016/j.chemosphere.2017.02.069>

Novich, B.E., Ring, T.A., 1984. Colloid stability of clays using photon correlation spectroscopy.

Clays Clay Miner. 32, 400.

Nowack, B., Bucheli, T.D., 2007. Occurrence, behavior and effects of nanoparticles in the

environment. *Environ. Pollut.* 150, 5–22. <https://doi.org/10.1016/j.envpol.2007.06.006>

Pachapur, V.L., Dalila Larios, A., Cledón, M., Brar, S.K., Verma, M., Surampalli, R.Y., 2016.

Behavior and characterization of titanium dioxide and silver nanoparticles in soils. *Sci.*

Total Environ. 563–564, 933–943. <https://doi.org/10.1016/j.scitotenv.2015.11.090>

Park, C.M., Chu, K.H., Heo, J., Her, N., Jang, M., Son, A., Yoon, Y., 2016. Environmental

behavior of engineered nanomaterials in porous media: A review. *J. Hazard. Mater.* 309,

133–150. <https://doi.org/10.1016/j.jhazmat.2016.02.006>

Parks, G.A., 1965. The isoelectric points of solid oxides, solid hydroxides, and aqueous hydroxo

complex systems. *Chem. Rev.* 65, 177–198.

Petosa, A.R., Jaisi, D.P., Quevedo, I.R., Elimelech, M., Tufenkji, N., 2010. Aggregation and

deposition of engineered nanomaterials in aquatic environments: role of physicochemical

interactions. *Environ. Sci. Technol.* 44, 6532–6549.

Philippe, A., Schaumann, G.E., 2014. Interactions of dissolved organic matter with natural and

engineered inorganic colloids: A review. *Environ. Sci. Technol.* 48, 8946–8962.

<https://doi.org/10.1021/es502342r>

Prasad, G.K., Agarwal, G.S., Singh, B., Rai, G.P., Vijayaraghavan, R., 2009. Photocatalytic

inactivation of *Bacillus anthracis* by titania nanomaterials. *J. Hazard. Mater.* 165, 506–510.

Rastghalam, Z.S., Cheng, T., Freake, B., 2018. Fine particle attachment to quartz sand in the

presence of multiple interacting dissolved components. *Sci. Total Environ.* 645, 499–508.

<https://doi.org/10.1016/j.scitotenv.2018.07.131>

Rastghalam, Z.S., Yan, C., Shang, J., Cheng, T., 2019. Nanoscale titanium dioxide (nTiO₂) aggregation and transport in the co-presence of dissolved phosphate, illite colloid, and Fe oxyhydroxide coating. *Colloids Surfaces A Physicochem. Eng. Asp.* 578, 123560.

<https://doi.org/10.1016/j.colsurfa.2019.06.025>

Rehn, B., Seiler, F., Rehn, S., Bruch, J., Maier, M., 2003. Investigations on the inflammatory and genotoxic lung effects of two types of titanium dioxide: Untreated and surface treated.

Toxicol. Appl. Pharmacol. 189, 84–95. [https://doi.org/10.1016/S0041-008X\(03\)00092-9](https://doi.org/10.1016/S0041-008X(03)00092-9)

Ren, M., Horn, H., Frimmel, F.H., 2017. Aggregation behavior of TiO₂ nanoparticles in municipal effluent: Influence of ionic strength and organic compounds. *Water Res.* 123, 678–686. <https://doi.org/10.1016/j.watres.2017.07.021>

Rietra, R.P.J.J., Hiemstra, T., van Riemsdijk, W.H., 2001. Interaction between calcium and phosphate adsorption on goethite. *Environ. Sci. Technol.* 35, 3369–3374.

Robichaud, C.O., Uyar, A.E., Darby, M.R., Zucker, L.G., Wiesner, M.R., 2009. Estimates of upper bounds and trends in nano-TiO₂ production as a basis for exposure assessment.

Environ. Sci. Technol. 43, 4227–4233.

Ronson, T.K., McQuillan, A.J., 2002. Infrared spectroscopic study of calcium and phosphate ion coadsorption and of brushite crystallization on TiO₂. *Langmuir* 18, 5019–5022.

<https://doi.org/10.1021/la011676q>

Ryan, J.N., Elimelech, M., Ard, R.A., Harvey, R.W., Johnson, P.R., 1999. Bacteriophage PRD1 and silica colloid transport and recovery in an iron oxide-coated sand aquifer. *Environ. Sci. Technol.* 33, 63–73.

Ryan, J.N., Gschwend, P.M., 1992. Effect of iron diagenesis on the transport of colloidal clay in

- an unconfined sand aquifer. *Geochim. Cosmochim. Acta* 56, 1507–1521.
- Sasidharan, S., Bradford, S.A., Šimůnek, J., Torkzaban, S., Vanderzalm, J., 2017. Transport and fate of viruses in sediment and stormwater from a Managed Aquifer Recharge site. *J. Hydrol.* 555, 724–735. <https://doi.org/10.1016/j.jhydrol.2017.10.062>
- Sasidharan, S., Torkzaban, S., Bradford, S.A., Kookana, R., Page, D., Cook, P.G., 2016. Transport and retention of bacteria and viruses in biochar-amended sand. *Sci. Total Environ.* 548–549, 100–109. <https://doi.org/10.1016/j.scitotenv.2015.12.126>
- Schramm, L.L., 2006. *Emulsions, foams, and suspensions: fundamentals and applications*. John Wiley & Sons.
- Shani, C., Weisbrod, N., Yakirevich, A., 2008. Colloid transport through saturated sand columns: Influence of physical and chemical surface properties on deposition. *Colloids Surfaces A Physicochem. Eng. Asp.* 316, 142–150. <https://doi.org/10.1016/j.colsurfa.2007.08.047>
- Sharma, V.K., 2017. Aggregation and toxicity of titanium dioxide nanoparticles in aquatic environment — A Review. *J. Environ. Sci. Heal. Part A* 4529. <https://doi.org/10.1080/10934520903263231>
- Sharma, V.K., 2009. Aggregation and toxicity of titanium dioxide nanoparticles in aquatic environment-a review. *J. Environ. Sci. Heal. - Part A Toxic/Hazardous Subst. Environ. Eng.* 44, 1485–1495. <https://doi.org/10.1080/10934520903263231>
- Shen, C., Lazouskaya, V., Zhang, H., Wang, F., Li, B., Jin, Y., Huang, Y., 2012. Theoretical and experimental investigation of detachment of colloids from rough collector surfaces. *Colloids Surfaces A Physicochem. Eng. Asp.* 410, 98–110. <https://doi.org/10.1016/j.colsurfa.2012.06.025>
- Shi, Z., Allen, H.E., Di Toro, D.M., Lee, S.Z., Flores Meza, D.M., Loftis, S., 2007. Predicting

- cadmium adsorption on soils using WHAM VI. *Chemosphere* 69, 605–612.
<https://doi.org/10.1016/j.chemosphere.2007.03.001>
- Singh, A.L., Tripathi, A.K., Singh, V.K., 2012. Nitrate and phosphate contamination in ground water of Varanasi, Uttar Pradesh, India. *J. Ind. Res. Technol.* 2, 26–32.
- Solovitch, N., Labille, J., Rose, J., Chaurand, P., Borschneck, D., Wiesner, M.R., Bottero, J.-Y., 2010. Concurrent Aggregation and Deposition of TiO₂ Nanoparticles in a Sandy Porous Media. *Environ. Sci. Technol.* 44, 4897–4902.
- Sposito, G., 2008. *The chemistry of soils*. Oxford university press.
- Sun, P., Shijirbaatar, A., Fang, J., Owens, G., Lin, D., Zhang, K., 2015a. Science of the Total Environment Distinguishable Transport Behavior of Zinc Oxide Nanoparticles in Silica Sand and Soil Columns. *Sci. Total Environ.* 505, 189–198.
<https://doi.org/10.1016/j.scitotenv.2014.09.095>
- Sun, P., Zhang, K., Fang, J., Lin, D., Wang, M., Han, J., 2015b. Transport of TiO₂ nanoparticles in soil in the presence of surfactants. *Sci. Total Environ.* 527–528, 420–428.
<https://doi.org/10.1016/j.scitotenv.2015.05.031>
- Sygouni, V., Chrysikopoulos, C. V, 2015. Characterization of TiO₂ nanoparticle suspensions in aqueous solutions and TiO₂ nanoparticle retention in water-saturated columns packed with glass beads. *Chem. Eng. J.* 262, 823–830. <https://doi.org/10.1016/j.cej.2014.10.044>
- Syngouna, V.I., Chrysikopoulos, C. V, 2013. Cotransport of clay colloids and viruses in water saturated porous media. *Colloids Surfaces A Physicochem. Eng. Asp.* 416, 56–65.
- Syngouna, V.I., Chrysikopoulos, C. V, Kokkinos, P., Tselepi, M.A., Vantarakis, A., 2017. Cotransport of human adenoviruses with clay colloids and TiO₂ nanoparticles in saturated porous media : Effect of flow velocity. *Sci. Total Environ.* 598, 160–167.

<https://doi.org/10.1016/j.scitotenv.2017.04.082>

- Tang, Z., Cheng, T., 2018. Stability and aggregation of nanoscale titanium dioxide particle (nTiO₂): Effect of cation valence , humic acid , and clay colloids. *Chemosphere* 192, 51–58. <https://doi.org/10.1016/j.chemosphere.2017.10.105>
- Tang, Z., Cheng, T., Fisher-Power, L.M., 2018. Influence of aggregation on nanoscale titanium dioxide (nTiO₂) deposition to quartz sand. *Chemosphere* 209, 517–524. <https://doi.org/10.1016/j.chemosphere.2018.06.112>
- Tempkin, M.I., Pyzhev, V., 1940. Kinetics of ammonia synthesis on promoted iron catalyst. *Acta Phys. Chim. USSR* 12, 327.
- Tian, Y., Gao, B., Wang, Y., Morales, V.L., Carpena, R.M., Huang, Q., Yang, L., 2012. Deposition and transport of functionalized carbon nanotubes in water-saturated sand columns. *J. Hazard. Mater.* 213–214, 265–272. <https://doi.org/10.1016/j.jhazmat.2012.01.088>
- Tiede, K., Boxall, A.B.A., Tear, S.P., Lewis, J., David, H., Hassellöv, M., 2008. Detection and characterization of engineered nanoparticles in food and the environment. *Food Addit. Contam.* 25, 795–821.
- Toloni, I., Lehmann, F., Ackerer, P., 2014. Modeling the effects of water velocity on TiO₂nanoparticles transport in saturated porous media. *J. Contam. Hydrol.* 171, 42–48. <https://doi.org/10.1016/j.jconhyd.2014.10.004>
- Torkzaban, S., Wan, J., Tokunaga, T.K., Bradford, S.A., 2012. Impacts of bridging complexation on the transport of surface-modified nanoparticles in saturated sand. *J. Contam. Hydrol.* 136–137, 86–95. <https://doi.org/10.1016/j.jconhyd.2012.05.004>
- Treumann, S., Torkzaban, S., Bradford, S.A., Visalakshan, R.M., Page, D., 2014. An explanation

- for differences in the process of colloid adsorption in batch and column studies. *J. Contam. Hydrol.* 164, 219–229. <https://doi.org/10.1016/j.jconhyd.2014.06.007>
- USEPA, 1996. Method 3050B - Acid digestion of sediments, sludges, and soils. 1996 2, 12. <https://doi.org/10.1117/12.528651>
- Van Olphen, H., 1963. An introduction to clay colloid chemistry, for clay technologists, geologists, and soil scientists. New York.
- Verwey, E.J.W., Overbeek, J.T.G., 1948. *Theory of Stability of Lyophobic Colloids* Elsevier Publishing" Co.
- Virkutyte, J., Al-Abed, S.R., Choi, H., Bennett-Stamper, C., 2014. Distinct structural behavior and transport of TiO₂nano- and nanostructured particles in sand. *Colloids Surfaces A Physicochem. Eng. Asp.* 443, 188–194. <https://doi.org/10.1016/j.colsurfa.2013.11.004>
- Walshe, G.E., Pang, L., Flury, M., Close, M.E., Flintoft, M., 2010. Effects of pH, ionic strength, dissolved organic matter, and flow rate on the co-transport of MS2 bacteriophages with kaolinite in gravel aquifer media. *Water Res.* 44, 1255–1269.
- Wang, D., Bradford, S.A., Harvey, R.W., Gao, B., Cang, L., Zhou, D., 2012. Humic acid facilitates the transport of ARS-labeled hydroxyapatite nanoparticles in iron oxyhydroxide-coated sand. *Environ. Sci. Technol.* 46, 2738–2745. <https://doi.org/10.1021/es203784u>
- Wang, D., Su, C., Zhang, W., Hao, X., Cang, L., Wang, Y., Zhou, D., 2014. Laboratory assessment of the mobility of water-dispersed engineered nanoparticles in a red soil (Ultisol). *J. Hydrol.* 519, 1677–1687. <https://doi.org/10.1016/j.jhydrol.2014.09.053>
- Wang, D., Zhang, W., Zhou, D., 2013. Antagonistic effects of humic acid and iron oxyhydroxide grain-coating on biochar nanoparticle transport in saturated sand. *Environ. Sci. Technol.* 47, 5154–5161. <https://doi.org/10.1021/es305337r>

- Wang, P., 2017. Aggregation of TiO₂ Nanoparticles in Aqueous Media: Effects of pH, Ferric Ion and Humic Acid. *Int. J. Environ. Sci. Nat. Resour.* 1, 1–6.
<https://doi.org/10.19080/ijesnr.2017.01.555575>
- Wang, Q., Cheng, T., Wu, Y., 2015. Distinct roles of illite colloid and humic acid in mediating arsenate transport in water-saturated sand columns. *Water, Air, Soil Pollut.* 226, 129.
- Westerhoff, P., Nowack, B., 2013. Searching for global descriptors of engineered nanomaterial fate and transport in the environment. *Acc. Chem. Res.* 46, 844–853.
<https://doi.org/10.1021/ar300030n>
- Wiesner, M.R., Lowry, G. V., Alvarez, P., Dionysiou, D., Biswas, P., 2006. Assessing the risks of manufactured nanomaterials. *Environ. Sci. Technol.* 40, 4336–4345.
<https://doi.org/10.1021/es062726m>
- Wilkinson, K.J., Joz-Roland, A., Buffle, J., 1997. Different roles of pedogenic fulvic acids and aquagenic biopolymers on colloid aggregation and stability in freshwaters. *Limnol. Oceanogr.* 42, 1714–1724. <https://doi.org/10.4319/lo.1997.42.8.1714>
- Wilson, M.J., Wilson, L., Patey, I., 2014. The influence of individual clay minerals on formation damage of reservoir sandstones: a critical review with some new insights. *Clay Miner.* 49, 147–164.
- Windler, L., Lorenz, C., von Goetz, N., Hungerbühler, K., Amberg, M., Heuberger, M., Nowack, B., 2012. Release of Titanium Dioxide from Textiles during Washing. *Environ. Sci. Technol.* 46, 8181–8188. <https://doi.org/10.1021/es301633b>
- Wu, D., Tong, M., Kim, H., 2016. Influence of Perfluorooctanoic Acid on the Transport and Deposition Behaviors of Bacteria in Quartz Sand. *Environ. Sci. Technol.*
<https://doi.org/10.1021/acs.est.5b05496>

- Wu, Y., Cheng, T., 2016. Stability of nTiO₂ particles and their attachment to sand : Effects of humic acid at different pH. *Sci. Total Environ.* 541, 579–589.
<https://doi.org/http://dx.doi.org/10.1016/j.scitotenv.2015.09.116> 0048-9697
- Xie, F., Wu, F., Liu, G., Mu, Y., Feng, C., Wang, H., Giesy, J.P., 2013. Removal of phosphate from eutrophic lakes through adsorption by in situ formation of magnesium hydroxide from diatomite. *Environ. Sci. Technol.* 48, 582–590.
- Xu, F., 2018. Review of analytical studies on TiO₂ nanoparticles and particle aggregation , coagulation , flocculation , sedimentation , stabilization. *Chemosphere* 212, 662–677.
<https://doi.org/10.1016/j.chemosphere.2018.08.108>
- Xu, S., Gao, B., Saiers, J.E., 2006. Straining of colloidal particles in saturated porous media. *Water Resour. Res.* 42, 1–10. <https://doi.org/10.1029/2006WR004948>
- Yan, C., Cheng, T., Shang, J., 2019. Effect of bovine serum albumin on stability and transport of kaolinite colloid. *Water Res.* 155, 204–213.
- Zhang, H., Nordin, N.A., Olson, M.S., 2013. Evaluating the effects of variable water chemistry on bacterial transport during infiltration. *J. Contam. Hydrol.* 150, 54–64.
<https://doi.org/10.1016/j.jconhyd.2013.04.003>
- Zhang, Y., Chen, Y., Westerhoff, P., Crittenden, J., 2009. Impact of natural organic matter and divalent cations on the stability of aqueous nanoparticles. *Water Res.* 43, 4249–4257.
<https://doi.org/10.1016/j.watres.2009.06.005>
- Zhou, D., Abdel-fattah, A.I., Keller, A.A., 2012. Clay Particles Destabilize Engineered Nanoparticles in Aqueous Environments. *Environ. Sci. Technol.* 7520–7526.
- Zhou, Y., Cheng, T., 2018. Influence of natural organic matter in porous media on fine particle transport. *Sci. Total Environ.* 627, 176–188. <https://doi.org/10.1016/j.scitotenv.2018.01.210>

